SOLID STATE PHASE TRANSFORMATIONS IN URANIUM-ZIRCONIUM ALLOYS

A Dissertation

by

SANDEEP IRUKUVARGHULA

Submitted to the Office of Graduate Studies of
Texas A&M University
in partial fulfillment of the requirements for the degree of

DOCTOR OF PHILOSOPHY

Chair of Committee,	Sean M. McDeavitt
Committee Members,	Lin Shao
	Pavel V. Tsvetkov
	Raymundo Arróyave
Head of Department,	Yassin A. Hassan

August 2013

Major Subject: Nuclear Engineering

ABSTRACT

Uranium-10wt% zirconium (U-10Zr) alloy nuclear fuels have been used for decades and new variations are under consideration ranging from U-5Zr to U-50Zr. As a precursor to understanding the fission gas behavior in U-Zr alloys using ion implantation, a basic study on the U-Zr metallurgy was completed using EPMA, DSC, XRD, Optical microscopy, and TEM with a focus on solid state phase transformations in alloys containing 2, 5, 10, 20, 30, and 50wt% zirconium. Alloys were cast by crucible melting using high temperature furnace under argon atmosphere in yttrium oxide crucibles and various thermal profiles were used to study phase transformations in these alloys.

Using TEM, XRD, and DSC data, it was ascertained that athermal-ω, along with martensitic $\alpha^{'}$, formed in all alloys quenched from γ phase. XRD could detect the presence of athermal-ω only in U-20, 30 and 50wt%Zr alloys. BSE images for as-cast alloys of 2, 5, 10, 20, and 30wt%Zr had lamellar microstructure with lamellae rich in zirconium. All alloy samples clearly showed a heating transformation pertaining to $\delta \rightarrow \gamma$ in DSC data while XRD could only confirm the presence of δ phase in U-20, 30, and 50wt%Zr alloys. An explanation is offered for the absence of δ phase peaks in uranium-rich alloys based on it's formation mechanism.

Alloy samples of U-2, 5, and 10wt%Zr were step-cooled from γ phase by annealing in the $(\alpha + \delta)$ phase field before cooling to room temperature revealed broad peaks for δ phase indicating incomplete collapse of $\{111\}_{\gamma}$ planes. Both as cast and γ-quenched alloys were annealed at 600^{o}C, in the $(\alpha + \delta)$ phase field for 1, 3, 7, and 30 days. Microstructures of the samples in both cases contained uranium-rich matrix and zirconium-rich precipitates and WDS analyses were consistent with their being α-U and δ phase respectively. However, XRD data for annealed alloys never showed peaks for δ phase even though it's area fraction was within the detection limits. Moreover, the peaks which were present in U-20wt%Zr vanished after annealing for

7 days. Based on the data obtained, it is suggested that it is more appropriate to consider the presence of metastable diffusional-ω instead of a stable δ in the as-cast alloys and that it is not stable at 600^{o}C.

ACKNOWLEDGMENTS

I must thank Dr. Munshi (Indian Institute of Technology kanpur) and Dr. Nelson (Texas A&M University) for giving me the opportunity to to join Ph.D program in Nulcear Engineering at Texas A&M University. I am also thankful to Dr. McDeavitt for accepting me as his student and introducing me to the fascinating field of uranium metallurgy. His attention to detail and articulation on subtle aspects of the subject had a profound influence on me during the course of this research. I also thank Dr. Shao, Dr. Tsvetkov, and Dr. Arróyave for accepting to be in my committee and for also giving their valuable comments during personal interactions.

My colleagues at Fuel Cycle and Materials Laboratory (FCML) have been extremely helpful in tackling problems with various instruments in the lab. I thank Jeff Clemens for helping me with quartz tube sealing, Aaron and Julie for introducing me to the art of sample preparation for SEM, Jeff Hausamann for teaching me how to use DSC, and Daniel Eichel for his help in fixing the furnace used for casting alloys. Sangjoon who was in the same project as I was in, has been a valuable critic throughout and his constructuve criticisms have helped a lot. Thanks are due to Dr. Guillemette of the Geology department for his unparalleled expertize on EPMA, Microscopy and Imaging Center, for allowing me to use the optical microscope, and Dr. Karaman for allowing me to access XRD instrument in his lab. His students Kadri, Nevin and, Ji Ma, and Dr. Anup Bandyopadhyay helped me collect the data. Dr. Nattamai of chemistry department is also thanked for allowing me to access TOPAS software for analyzing the diffraction data. Library personnel at TAMU were extremely diligent in procuring documents related to this research, some of which were seemingly impossible to obtain.

Thanks are due to Dr. Hartmann for hosting me at UNLV for TEM and XRD analysis on U-Zr samples. I am also extremely thankful to Dr. Egeland for teaching me how to use tecnai and also in optimizing the TEM sample preparation method for

my alloys. I had numerous discussions with him which triggered the whole idea of ω transformation occurring in U-Zr system and it's relation to δ phase. Dr. Hartmann also conducted Reitveld analysis on XRD data of a couple of samples for which I thank him. Thanks are also due to Dr. Joseph McKeown (LLNL), for the discussions on δ phase formation mechanism.

I also thank my friends Bhanesh, Alok, Sarat, Ravish, Gupta, Gentry, and Hyocheol for numerous get-togethers and endless discussions on wide ranging tpoics. My friends at SPICMACAY are also thanked, for I had a great time being involved in organizing some concerts at TAMU. I also thank Swaroop for encouraging me to pursue Ph.D and has been a strong moral support all along.

I sincerely thank my parents and my sister for showing confidence in me and supporting the idea of pursuing doctoral studies. This would not have happened without them. My wife Divya has been extremely patient and supportive. Her unmatched moral support whenever I had a failed experiment or an idea is indescribable.

Finally I thank everyone who directly or indirectly helped me during the course of my doctoral research.

Sandeep Irukuvarghula
College Station, 2013

NOMENCLATURE

α-U	Orthorhombic crystal structure of uranium with 4 atoms per unit cell
$\alpha_a^{'}$	Orthorhombic crystal structure with contraction of b parameter and having acicular morphology
$\alpha_b^{'}$	Orthorhombic crystal structure with contraction of b parameter and having banded morphology
$\alpha_b^{''}$	Monoclinic crystal structure having banded morphology
β	Tetragonal crystal structure of uranium with 30 atoms per unit cell
b.c.c	Body centered cubic crystal structure
γ	b.c.c crystal structure of uranium
γ^o	Tetragonal distortion of γ
γ^s	Even less deviation from equilibrium γ phase
$\hat{\gamma}$	Angle between a and b parameters of α-U
h.c.p	Hexagonal close packed crystal structure
ω	Metastable phase in zirconium alloys with hexagonal crystal structure
ω_d	Diffusional-omega formed in as-cast alloys which are slowly cooled form γ phase
ω_{ath}	Athermal-omega formed when quenched from γ phase
δ	C32-AlB_2 type structure and is a partially ordered ω
MA	Minor actinides
EBR I	Experimental Breeder Reactor I
EBR II	Experimental Breeder Reactor II
FCMI	Fuel Cladding Mechanical Interaction
FCCI	Fuel Cladding Chemical Interaction

FP	Fission Products
PIE	Post Irradiation Examination
EPMA	Electron Probe Micro Analysis
DSC	Differential Scanning Calorimetry
XRD	X-Ray Diffraction
TEM	Transmission Electron Microscopy
SAD	Selected Area Diffraction
DU	Depleted Uranium
WDS	Wavelength Dispersive Spectroscopy
DIC	Differential Interference Contrast
BSE	Back Scattered Electron image
SS	Stainless Steel
MIC	Microscopy and Imaging Center
OR	Orientation Relationship
EDS	Energy Dispersive Spectroscopy
UNLV	University of Nevada, Las Vegas
SEM	Scanning Electron Microscope

TABLE OF CONTENTS

Page

ABSTRACT ii

ACKNOWLEDGMENTS iv

NOMENCLATURE vi

TABLE OF CONTENTS viii

LIST OF TABLES x

LIST OF FIGURES xii

1 INTRODUCTION 1

1.1 Motivation 2
1.2 Objective and Scope of the Work 5

2 PHASE TRANSFORMATIONS IN BINARY URANIUM ALLOYS 6

2.1 Transformations Between Equilibrium Phases 6
2.2 Metastable Phases in Uranium Alloys and Associated Phase Transformations 6
2.2.1 $\gamma \rightarrow \alpha^{'}$ Transformation 8
2.2.2 $\beta \rightarrow \alpha^{'}$ Transformation 13
2.2.3 ω Phase in Zr and it's Alloys 14
2.2.4 B.C.C-$\gamma \rightarrow \omega$ Transformation and the Relationship Between ω and δ 15
2.3 The U-Zr System 18

3 EXPERIMENTAL METHODS AND ANALYSES 22

3.1 Alloy Preparation 22
3.1.1 Heat Treatments of Specimens 25
3.2 Specimen Sample Preparation 27
3.2.1 Electron Probe Micro Analysis 27
3.2.2 Optical Microscopy 29
3.2.3 X-ray Diffraction 29
3.2.4 Differential Scanning Calorimetry 30
3.2.5 Transmission Electron Microscopy 30

Page

4 RESULTS . . . 32

4.1 Metallurgy of U-2wt%Zr Alloy . . . 32
4.1.1 As-cast and γ-Quenched Samples . . . 32
4.1.2 Samples Step-Cooled from the γ Phase . . . 36
4.1.3 Samples Annealed at 600^{o}C . . . 39
4.2 Metallurgy of U-5wt%Zr . . . 45
4.2.1 As-cast and γ-Quenched Samples . . . 45
4.2.2 Samples Step-Cooled from the γ Phase . . . 49
4.2.3 Samples Annealed at 600^{o}C . . . 51
4.3 Metallurgy of U-10wt%Zr . . . 57
4.3.1 As-cast and γ-Quenched Samples . . . 57
4.3.2 Samples Step-Cooled from the γ Phase . . . 62
4.3.3 Samples Annealed at 600^{o}C . . . 66
4.4 Metallurgy of U-20wt%Zr . . . 72
4.4.1 As-cast and γ-Quenched Samples . . . 72
4.4.2 Samples Step-Cooled from the γ Phase . . . 76
4.4.3 Samples Annealed at 600^{o}C . . . 77
4.5 Metallurgy of U-30wt%Zr . . . 83
4.5.1 As-cast and γ-Quenched Samples . . . 83
4.5.2 Samples Step-Cooled from the γ Phase . . . 86
4.5.3 Samples Annealed at 600^{o}C . . . 88
4.6 Metallurgy of U-50wt%Zr . . . 90
4.6.1 As-cast and γ-Quenched Samples . . . 90
4.6.2 Samples Annealed at 600^{o}C . . . 92

5 DISCUSSION . . . 95

5.1 Quenched and As-cast Alloys . . . 95
5.1.1 Phase Transformation Sequence in γ-Quenched Alloys . . . 108
5.2 Step-Cooled Alloys . . . 112
5.2.1 Alloys Quenched from $(\alpha + \gamma)$ Phase Field . . . 112
5.2.2 Alloys Step-Cooled to $(\alpha + \delta)$ and Annealed . . . 113
5.3 Annealed Alloys . . . 114

6 SUMMARY AND CONCLUSIONS . . . 121

REFERENCES . . . 123

LIST OF TABLES

TABLE Page

2.1 Sequences of structural transitions in transition metals as a function of their d-band occupancy 15

2.2 Transformation temperatures and the reaction types in U-Zr system . . . 21

3.1 Weights of DU and Zr used in casting the alloys 23

3.2 WDS analysis indicating macro-segregation of Zr in U-10wt%Zr alloy . . 24

3.3 Metallographic preparation steps for U-Zr alloys 28

4.1 WDS analysis of step-cooled U-2Zr alloy 37

4.2 WDS analysis of annealed U-2Zr alloy samples 43

4.3 WDS analysis of step-cooled U-5Zr alloy 51

4.4 WDS analysis of annealed U-5Zr alloy samples 53

4.5 WDS analysis of step-cooled U-10Zr alloy 62

4.6 WDS analysis of annealed U-10Zr alloy samples 68

4.7 WDS analysis of annealed U-20Zr alloy samples 79

4.8 WDS analysis of annealed U-30Zr alloy samples 89

5.1 Ambient temperature phases in the alloys determined using XRD, TEM, EPMA, and DSC 96

5.2 $\delta(\omega_d) \rightarrow \gamma$ and $\omega \rightarrow \gamma$ transformation temperatures from DSC curves during heating for as-cast and the alloys quenched from γ phase 105

5.3 Transformation temperatures from DSC curves during heating for the alloys quenched from γ phase 109

5.4 Possible transformation schemes upon quenching from γ phase 110

5.5 Amount of γ phase present in as-cast U-5Zr and U-10Zr alloys as a function of annealing time 116

LIST OF FIGURES

FIGURE Page

1.1 Transverse metallographic section of U-10wt%Zr alloy at 5 at% burnup with superimposed microprobe scans 3

2.1 Schematic of crystal structures: Relationship between b.c.c γ (4 unit cells) and γ^o (left) and orthorhombic α phase (right) 8

2.2 Representation of diffraction patterns of α and α-like phases, and γ and γ^o 9

2.3 Projection of atoms in b.c.c structure on (110) b.c.c plane. 10

2.4 Schematic of $\gamma \rightarrow \alpha^{'}$ transformation along with shuffles 10

2.5 Lattice correspondences projected on $(110)_\gamma$, of Speer-Edmonds (left) and May (right) with the shuffles shown by arrows 12

2.6 Formation of ω from b.c.c-γ by the collapse of $\{111\}$ planes 16

2.7 Collapse of (111) planes in b.c.c (colored) to form (0001) planes of ω. Unit cells of b.c.c-γ are shown in full lines while those of ω are shown by broken lines 17

2.8 Projection of atomic positions on $(111)_\gamma$ and $(0001)_\delta$ 18

2.9 Assessed phase diagram of U-Zr system by Sheldon 19

3.1 Melt casting of U-Zr alloys 23

3.2 Microstructural features of as-cast U-10wt%Zr alloy 24

3.3 U-Zr alloy sample heat treatments 26

4.1 Back scattered and optical images of as cast U-2Zr alloy 33

4.2 XRD pattern of as-cast U-2Zr alloy 33

4.3 Back scattered and optical images of γ-quenched U-2Zr alloy 34

FIGURE Page

4.4 XRD pattern of γ-quenched U-2Zr alloy 34

4.5 DSC curves of γ-quenched and as-cast U-2Zr alloy showing various transformations (indicated by arrows) 35

4.6 Back scattered images of step-cooled U-2Zr alloys 36

4.7 XRD pattern of U-2Zr alloy step-cooled from $\gamma \xrightarrow[650C]{(\alpha+\gamma)}$ 2 days $\xrightarrow[600C]{(\alpha+\delta)}$ 3 days 38

4.8 XRD pattern of U-2Zr alloy step-cooled from $\gamma \xrightarrow[650C]{(\alpha+\gamma)}$ 2 days and quenched 38

4.9 Back scattered images of as-cast U-2Zr alloys annealed at 600^oC 40

4.10 XRD pattern of as-cast U-2Zr alloy annealed for 7 days 41

4.11 XRD pattern of as-cast U-2Zr alloy annealed for 30 days 41

4.12 BSE images of U-2Zr alloy quenched from γ phase and annealed for various times at 600^oC 42

4.13 XRD pattern of U-2Zr alloy quenched from γ phase and annealed for 7 days 44

4.14 XRD pattern of U-2Zr alloy quenched from γ phase and annealed for 30 days 44

4.15 Back scattered and optical images of as-cast U-5Zr alloy 45

4.16 XRD pattern of as-cast U-5Zr alloy 46

4.17 Back scattered and optical images of γ-quenched U-5Zr alloy 47

4.18 TEM images of γ-quenched U-5Zr alloy 47

4.19 XRD pattern of γ-quenched U-5Zr alloy 48

4.20 DSC curves of quenched and as-cast U-5Zr alloy showing various transformations (indicated by arrows) 49

FIGURE Page

4.21 Back scattered images of step-cooled U-5Zr alloys 50

4.22 XRD pattern of U-5Zr alloy step-cooled from $\gamma \xrightarrow[650C]{(\alpha+\gamma)}$ 2 days $\xrightarrow[600C]{(\alpha+\delta)}$ 3 days 50

4.23 XRD pattern of U-5Zr alloy step-cooled from $\gamma \xrightarrow[650C]{(\alpha+\gamma)}$ 2 days and quenched 51

4.24 Back scattered images of as-cast U-5Zr alloy annealed for various times at 600^{o}C 52

4.25 XRD pattern of as-cast U-5Zr alloy annealed for 7 days 54

4.26 XRD pattern of as-cast U-5Zr alloy annealed for 30 days 54

4.27 BSE images of U-5Zr alloy quenched from γ phase and annealed for various times at 600^{o}C 55

4.28 XRD pattern of U-5Zr alloy quenched from γ phase and annealed for 7 days 56

4.29 XRD pattern of U-5Zr alloy quenched from γ phase and annealed for 30 days 56

4.30 Back scattered and optical images of as-cast U-10Zr alloy 57

4.31 Optical image of as-cast U-10Zr at higher magnification showing lamellae within each grain 58

4.32 XRD pattern of as-cast U-10Zr alloy 59

4.33 BSE and optical images of γ-quenched U-10Zr alloy 60

4.34 TEM images of γ-quenched U-10Zr alloy 60

4.35 XRD pattern of γ-quenched U-10Zr alloy 61

4.36 DSC curves of U-10Zr alloy showing various transformations (indicated by arrows) 61

4.37 Back scattered and Bright field TEM images of step-cooled U-10Zr alloys 63

FIGURE Page

4.38 Bright field TEM image of U-10Zr alloy step-cooled from $\gamma \xrightarrow[650C]{(\alpha+\gamma)}$ 2 days and quenched showing lattice fringes 64

4.39 XRD pattern of U-10Zr alloy step-cooled from $\gamma \xrightarrow[650C]{(\alpha+\gamma)}$ 2 days $\xrightarrow[600C]{(\alpha+\delta)}$ 3 days 65

4.40 XRD pattern of U-10Zr alloy step cooled from $\gamma \xrightarrow[650C]{(\alpha+\gamma)}$ 2 days and quenched 66

4.41 Back scattered images of as-cast U-10Zr alloy annealed for various times at 600^{o}C 67

4.42 XRD pattern of as-cast U-10Zr alloy annealed for 7 days 68

4.43 XRD pattern of as-cast U-10Zr alloy annealed for 30 days 69

4.44 Back scattered images of U-10Zr alloy quenched from γ phase and annealed for various times at 600^{o}C 70

4.45 XRD pattern of U-10Zr alloy quenched from γ phase and annealed for 7 days 71

4.46 XRD pattern of U-10Zr alloy quenched from γ phase and annealed for 30 days 71

4.47 Back scattered and optical images of as-cast U-20Zr alloy 72

4.48 TEM images of as-cast U-20Zr alloy 73

4.49 XRD pattern of as-cast U-20Zr alloy 73

4.50 Optical (DIC) image of γ-quenched U-20Zr alloy 74

4.51 XRD pattern of γ-quenched U-20Zr alloy 75

4.52 DSC curves of U-20Zr alloy showing various transformations (indicated by arrows) 75

4.53 BSE images of step-cooled U-20Zr alloys 76

FIGURE Page

4.54 XRD pattern of U-20Zr alloy step-cooled from $\gamma \xrightarrow[650C]{(\alpha+\gamma)}$ 2 days and quenched 77

4.55 BSE images of as-cast U-20Zr alloy annealed for various times at 600^{o}C . 78

4.56 XRD pattern of as-cast U-20Zr alloy annealed for 7 days 80

4.57 XRD pattern of as-cast U-20Zr alloy annealed for 30 days 80

4.58 BSE images of U-20Zr alloy quenched from γ phase and annealed for various times at 600^{o}C 81

4.59 XRD pattern of U-20Zr alloy quenched from γ phase and annealed for 7 days 82

4.60 XRD pattern of U-20Zr alloy quenched from γ phase and annealed for 30 days 82

4.61 Back scattered and TEM images of as-cast U-30Zr alloy 84

4.62 XRD pattern of as-cast U-30Zr alloy 84

4.63 XRD pattern of γ-quenched U-30Zr alloy 85

4.64 DSC curves of quenched and as-cast U-30Zr alloy showing various transformations (indicated by arrows) 85

4.65 BSE images of step-cooled U-30Zr alloys 87

4.66 XRD pattern of U-30Zr alloy step-cooled from $\gamma \xrightarrow[650C]{(\alpha+\gamma)}$ 2 days and quenched 87

4.67 BSE images of as-cast U-30Zr alloys annealed for different times at 600^oC 88

4.68 BSE images of U-30Zr alloys quenched from γ phase and annealed for different times at 600^oC 90

4.69 XRD pattern of as-cast U-50Zr alloy 91

4.70 XRD pattern of γ-quenched U-50Zr alloy 91

FIGURE Page

4.71 DSC curves of U-50Zr alloy showing a single transformation 92

4.72 XRD pattern of as-cast U-50Zr alloy annealed for 7 days 93

4.73 XRD pattern of as-cast U-50Zr alloy annealed for 30 days 93

4.74 BSE images of U-50Zr alloys annealed for 30 days at 600^{o}C 94

5.1 XRD patterns of γ-quenched alloys (partial 2θ range) 107

5.2 XRD pattern of as-cast U-5Zr alloy annealed for 7 days 117

5.3 XRD pattern of as-cast U-5Zr alloy annealed for 30 days 117

5.4 XRD pattern of as-cast U-10Zr alloy annealed for 7 days 118

5.5 XRD pattern of as-cast U-10Zr alloy annealed for 30 days 118

1. INTRODUCTION

One of the most important characteristics of a nuclear fuel (uranium/plutonium compounds or uranium alloys) is its ability to achieve very high burn-up (tens of at%) without a cladding breach. Metallic fuels not only present such a capability, but also offer some unique advantages and hence have continued to receive much attention. Excellent breeding potential, high fissile and fertile atom density and hence high burn-up capability, good thermal conductivity, and ease of reprocessing are some of the attributes of metallic fuels [1].

Pure uranium, has three allotropes [2,3], α (Orthorhombic upto 668^{o}C), β (Tetragonal upto 776^{o}C), and γ (b.c.c upto 1135^{o}C), and it has very high fissile atom density but suffers from anisotropic growth and swelling of α phase, a result of anisotropic properties of orthorhombic crystal structure [4, 5]. Alloying uranium with elements like Zr, Mo, Ti, Nb etc not only overcomes this problem, but offers other advantages [1]. First, fast breeder reactor fuel inherently contains significant amount of plutonium besides uranium. U-Pu alloys have very low solidus temperature and it can be increased by alloying with the above mentioned elements, thus allowing safer margins for operation. Next, these elements lower the temperature of the b.c.c γ phase boundary which allows more fuel to operate in this isotropic phase. Further, alloy nuclear fuels offer straightforward reprocessing option which would allow the minor actinides (MA) to remain in the fuel cycle by their fabrication back into the fuel pin (example: U-MA-Zr).

Zirconium typically is the preferred fuel alloying additive as it increases the compatibility between fuel and cladding by reducing inter-diffusion between the components of each. The development of various metallic fuel types used in EBR I and EBR II, and their irradiation performance until and through 1970's has been reviewed by Walters et al [6]. Swelling, fission gas release, fuel cladding mechanical interaction

(FCMI), and fuel cladding chemical interaction (FCCI) issues in U-Zr and U-Pu-Zr fuels have been reviewed by Hofman et al [1, 7].

1.1 Motivation

Alloy nuclear fuels with very high burn-ups are desired as it translates to fuel having more residence time in the reactor which not only is economical but also reduces the amount of waste generated from spent nuclear fuel. However, the major limitation to reach high burn-ups comes from swelling of the fuel which leads to fuel-clad mechanical interactions (FCMI) and fuel-clad chemical interactions (FCCI), both of which may contribute to fuel performance limitations and cladding breach. Swelling is primarily caused by the continuous replacement of fissioned uranium/plutonium atoms by two or more atoms (fission products, FP) of greater average size and their interaction with point defects and sinks. In the case of solid FP's, they precipitate into pores and migrate towards periphery of the fuel. However, it is the gaseous fission products (Xenon and Krypton) that interact with point defects, forming gas bubbles which have dominating effect in swelling.

Reducing the smear density[1] helped circumvent this problem during EBR II operation and swelling is no longer a real constraint to reach high burn-ups [1]. However, reducing smeared density would reduce fuel loading in the reactor and this affects economical operation. Moreover, modeling fuel element behavior i.e. fission gas release, changes in fuel chemistry, and thermal conductivity as a function of burn-up would help design optimum fuel element and consequently, ensure safe and economical operation of a reactor.

While the problem of swelling in relation to achieving high burn-ups has been addressed quite successfully, modeling fuel element behavior in terms of various phys-

[1]Smear density denotes "a planar density calculated by dividing the mass of fuel (including any nongaseous fission products) in a unit length of pin by theoretical mass of a unit length of voidless fuel of the same composition, with diameter equal to the inside diameter of the cladding [7]."

ical processes occurring inside the fuel still remains a grand challenge. Current fuel performance codes [8–13] have fission gas release models containing empirical/semi-empirical relations which have limited range of validity. Motivation for this research comes from the post irradiation examination (PIE) data of U-Zr fuel from EBR II operation [14] and from the multi-atom gas bubble nucleation mechanism [15] (proposed to be operative in γ phase) and cavity nucleation model [16] (to be operative in α dominant phase) for fission gas release in metallic alloy nuclear fuels.

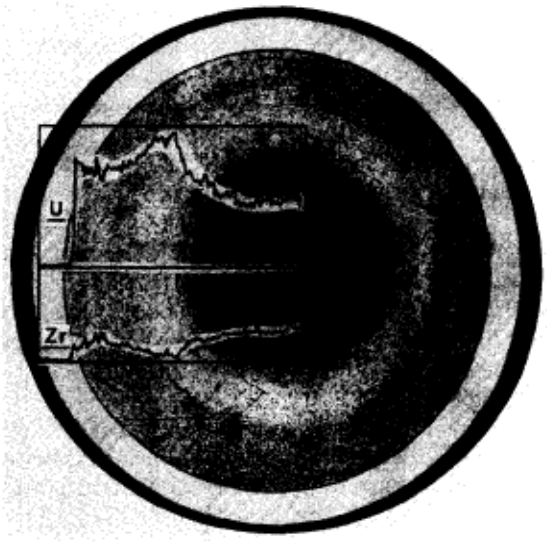

Fig. 1.1.: Transverse metallographic section of U-10wt%Zr alloy at 5 at% burnup with superimposed microprobe scans

Irradiation behavior of U-10wt%Zr alloys was assessed during the EBR-II operation [14]. Fuel constituent redistribution was observed as a result of temperature gradients across the fuel which resulted in the formation of distinct phase fields within the fuel, shown in Figure 1.1[2]. Depending on the burn-up, the peripheral zone consisted of $(\alpha + \delta)$ phase field, the central zone had γ phase while $(\alpha + \gamma)$ and

[2]Reprinted from Progress in Nuclear Energy, 31, G.L. Hofman, L.C. Walters, T.H. Bauer, Metallic Fast Reactor Fuels, 83–110, 1997, with permission from Elsevier.

$(\beta+\gamma)$ phase fields were present in the intermediate zones [7,17]. Zr migration from periphery to the center caused a Zr enriched central zone and a Zr depleted intermediate zone causing various U-Zr alloy compositions to form. It was observed that the $(\alpha+\delta)$ zone, which is dominated by α phase, is characterized by interconnected porosity formed due to the formation of gas bubbles at α/δ interface. Grain boundary tears formed due to anisotropic swelling of α phase were also seen. Swelling in γ phase was due to the formation of large fission gas bubbles in the matrix. Unlike the $(\alpha+\delta)$ zone which has bubbles preferentially formed at the α/δ interface, bubbles of larger size were seen in the γ phase matrix. Swelling in $(\alpha+\gamma)$ zone had a similar characteristic as in $(\alpha+\delta)$ zone but the γ lamellae were coarse in the α phase. *It is evident that the gas bubble nucleation conditions are different based on the metallurgical state of the alloy.*

The multi atom nucleation model considers phase transition theory for nucleation of gas bubbles [15]. Xe and Kr being noble gas atoms, have extremely low solubility in the fuel matrix and, once generated, become super-saturated in the matrix. At large super-saturations, the system transforms into a new phase as a whole instead of atom by atom transformation in order to lower its free energy and the new phase (inert gas bubble) will have a certain radius defined according to the degree of super-saturation. Once bubbles are formed, nucleation ceases as there wouldn't be enough atoms for super-saturation to occur. As fission events occur and gas atoms are generated, the process of nucleation begins once the saturation limit is reached. Because of irradiation induced re-solution, some of the bubbles are destroyed and the gas atoms re-appear in the matrix. Once the saturation limit is again reached, new bubbles nucleate. Bubbles diffuse via lattice and grain boundary diffusion mechanisms and coalesce with other bubbles. Bubbles thus grow, get interconnected, and once the interconnection reaches the surface of the fuel, the gas is released to the plenum. In order to test the model, data on fission gas bubble size distribution as a function of the amount of gas present in the fuel and diffusion coefficients of gas bubbles are

needed. In order to generate this data, a comprehensive and correct understanding of the fuel material science is required.

Ion implantations offer the capability to control the amount of gas present in a simulated fuel material and have been used to measure gas bubble size distributions using TEM [18–24]. Most of these studies were carried for UO_2 while the data on metallic fuels is very limited [25–27]. Since the bubble morphology depends on the metallurgical state of the alloy, ion implantations carried in specific phase fields give more insight towards gas bubble nucleation mechanisms. This forms the central idea of this research which aims to provide a thorough metallurgical characterization of U-Zr alloys for future ion beam studies.

1.2 Objective and Scope of the Work

The objective of this research is to study the solid state phase transformations in U-Zr system and characterize the alloys so that they form the baseline for further experiments using ion implantations. Alloys of varying Zr compositions were cast and were subjected to various heat treatments. They were then characterized using optical microscopy, Electron probe microanalysis (EPMA), Differential scanning calorimentry (DSC), Transmission electron microscopy (TEM), and X-ray diffraction (XRD). The dissertation is organized as follows. Phase transformations in uranium alloys and the associated metastable phases formed will be discussed in Chapter 2. This will serve as a background to better understand the results in present investigation. Experimental techniques, sample preparation methods, and thermal profiles studied will be outlined in Chapter 3 followed by results in Chapter 4. Results will be discussed in Chapter 5 and will be summarized and concluded in chapter 6.

2. PHASE TRANSFORMATIONS IN BINARY URANIUM ALLOYS

In this chapter, phase transformations between equilibrium and non-equilibrium phases in binary uranium alloys will be discussed in Sections 2.1 and 2.2 followed by ω phase in Zr alloys and the athermal γ to ω transformation which is unique to U-Zr alloys. Since present research is on solid state phase transformations in U-Zr alloys, literature on U-Zr system will be reviewed in Section 2.3.

2.1 Transformations Between Equilibrium Phases

The crystal structures of equilibrium phases of uranium have been determined as orthorhombic for α-U [28], tetragonal for β-U [29–38], and b.c.c for γ-U [39, 40]. Solid solubilities of various elements (Mo, Zr, Ti, Nb, Re, Ru) in α-U and β-U are extremely low (of the order of few at%) while it is much greater for γ-U (complete solid solubility for some elements like Zr and Ti). Transitions between these phases have been reviewed by Goldberg and Massalski [41] and by Yakel [42] and $\alpha \rightleftharpoons \beta$ and $\beta \rightleftharpoons \gamma$ transitions in uranium alloys involve diffusion controlled nucleation and growth processes.

2.2 Metastable Phases in Uranium Alloys and Associated Phase Transformations

Uranium alloys, when cooled from the BCC-γ phase, depending on the cooling rate and composition, transform into a variety of metastable phases [42, 43]. The metastable phases are typically distortions of the equilibrium structures, either in modified lattice parameters or angles, and they especially form as intermediate states under rapid cooling conditions. The reason for their formation is a consequence of rapid kinetics of formation of α phase in dilute alloys and will be elaborated later. When quenched from γ phase, the general sequence of metastable phases observed[1]

[1]Formation of the metastable ω phase in U-Zr alloys will be discussed in a separate Section

as a function of increasing solute content is: $\alpha_a^{'}$, $\alpha_b^{'}$, $\alpha_b^{''}$, γ^o, and γ^s. These metastable phases[2], are related to the equilibrium α and γ structures in that $\alpha_a^{'}$ has acicular appearance and $\alpha_b^{'}$ has banded appearance with same crystal structure as α but with a relative contraction in b parameter, $\alpha_b^{''}$ is monoclinic distortion of the α phase having banded morphology, γ^o is a tetragonal distortion of γ and γ^s is even less deviation from equilibrium γ phase.

Crystal structures of α-U, γ, and γ^o are shown in Figure 2.1, adapted from [45]. α-U can be thought of as base-centered orthorhombic structure with each lattice site containing two atoms thus making 4 atoms per unit cell. The two-atom motif at each lattice site is contained in the (100) plane, rotated about a axis. The (010) planes comprise of these atoms which form corrugated sheets [42]. In the case of $\alpha^{''}$, the monoclinic distortion is manifested as a change in $\hat{\gamma}$ which is the angle between a and b axes and the deviation is between 1-3^o. The structure of γ^o has been described by Yakel [46] and can be thought as forming as a result of a displacement wave which moves the body centered atoms (open circles in the Figure 2.1 (left)) in opposite directions (indicated by arrows).

A schematic of XRD patterns for α-like and γ-like phases is shown in Figure 2.2, adapted from [44]. It can be seen that in the case of $\alpha^{'}$, there is a displacement of $(021)_\alpha$ line towards $(002)_\alpha$ line and for $\alpha^{''}$, $(021)_\alpha$ and $(002)_\alpha$ lines overlap and there is a systematic splitting of $(110)_\alpha$, $(111)_\alpha$, $(112)_\alpha$, $(131)_\alpha$ lines. In the case of γ^o, there is a splitting of $(110)_\gamma$, $(200)_\gamma$, and $(211)_\gamma$ lines.

[2]Following the nomenclature by Lehmann and Hills [44]

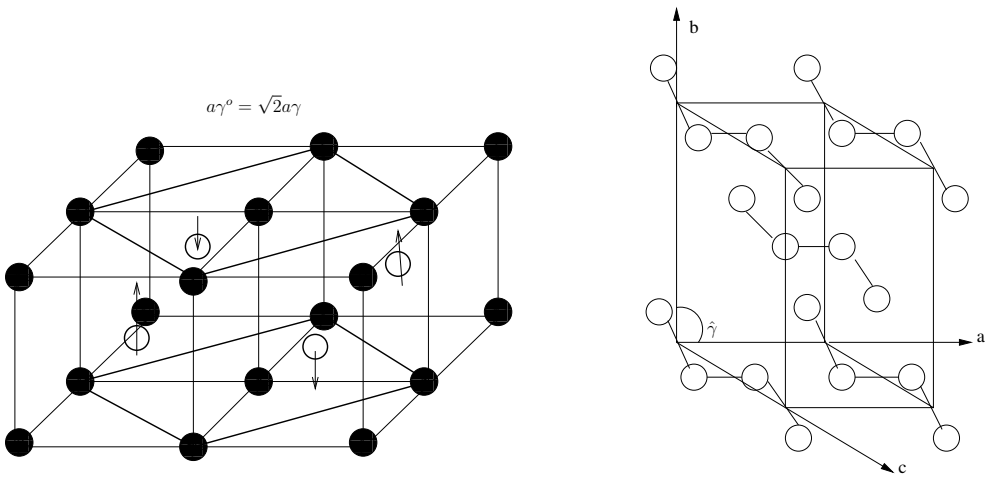

Fig. 2.1.: Schematic of crystal structures: Relationship between b.c.c γ (4 unit cells) and γ^o (left) and orthorhombic α phase (right)

2.2.1 $\gamma \rightarrow \alpha^{'}$ Transformation

The γ to $\alpha^{'}$ martensitic transformation[3] was first described by Hatt [48] in a model closely related to the Burgers mechanism [49] proposed for b.c.c to h.c.p transformation in Zr. In Hatt's model, the $\alpha^{'}$ structure is generated from γ by a shear on $\{112\}$ cubic planes in a $\langle 111 \rangle$cubic direction as the primary distortion with some shuffling of atoms needed (two atoms per lattice site as shown in Figure 2.1) for the orthorhombic structure to form. This mechanism is shown in Figure 2.3 (adapted from [50]) where the initial monoclinic structure denoted with $\hat{\gamma}$ angle which is 100.02 deg, is transformed by shearing of atoms to position C so that $\hat{\gamma}$ reaches 90^o. The orientation relationship between γ and $\alpha^{'}$ has been described as:

$$[100]_\alpha || [11\bar{1}]_\gamma ; [010]_\alpha || [\bar{2}1\bar{1}]_\gamma ; [001]_\alpha || [011]_\gamma$$

[3]Only transformations where β phase is completely skipped by alloy additions are considered in this document. The $\gamma \rightarrow \beta \rightarrow \alpha$ occurs in very dilute uranium alloys even at high quench rates which is a consequence of the kinetics of $\gamma \rightarrow \beta \rightarrow \alpha$ transformation in pure U [47].

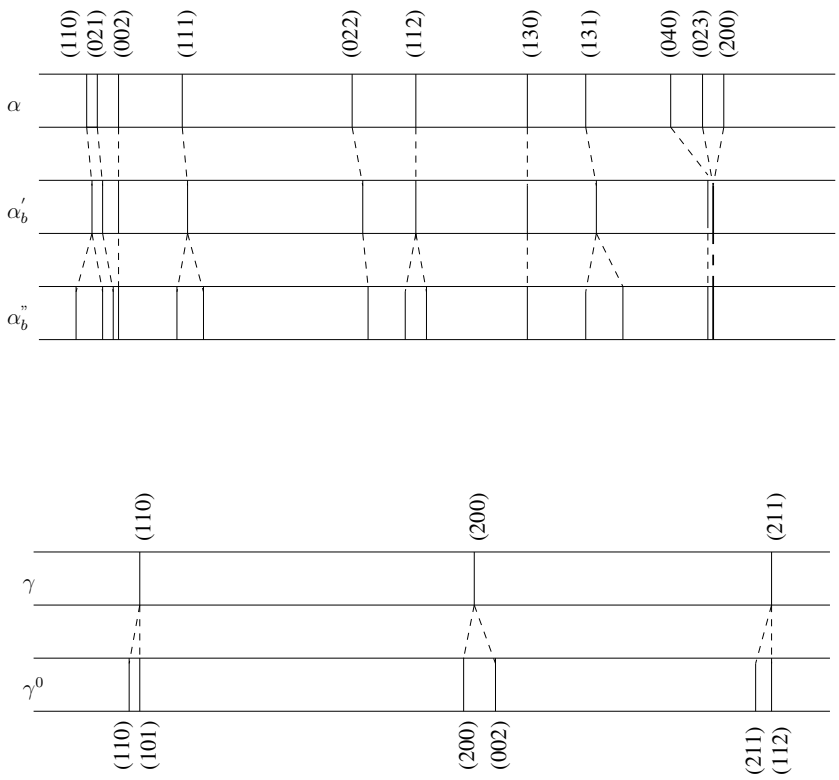

Fig. 2.2.: Representation of diffraction patterns of α and α-like phases, and γ and γ^o

A schematic adapted from [45] depecting the shuffles is shown in Figure 2.4. This figure is projected on $(110)_\gamma$ plane where $(11\bar{2})_\gamma$ is perpendicular to the plane of paper. A shear along $[111]_\gamma$ direction distorts the initial $\hat{\gamma}$ angle from 100.02 deg to 90 deg. Further shuffling of atoms completes the transformation as shown in the figure where $\alpha^{'}$ is projected on $(001)_\alpha$ plane. Within the context of this model, formation of metastable phases (i.e, $\alpha^{''}$ and γ^o) was explained by a model proposed by Tangri and Tangri and Williams [50, 51] in which by progressively restricting the magnitude of the shear (which translates to restricting the decrease in the $\hat{\gamma}$ angle shown in Figures 2.3 and 2.4), a continuous sequence of phases can be developed as:

$$\gamma \rightarrow \gamma^o \rightarrow \alpha^{''} \rightarrow \alpha^{'}$$

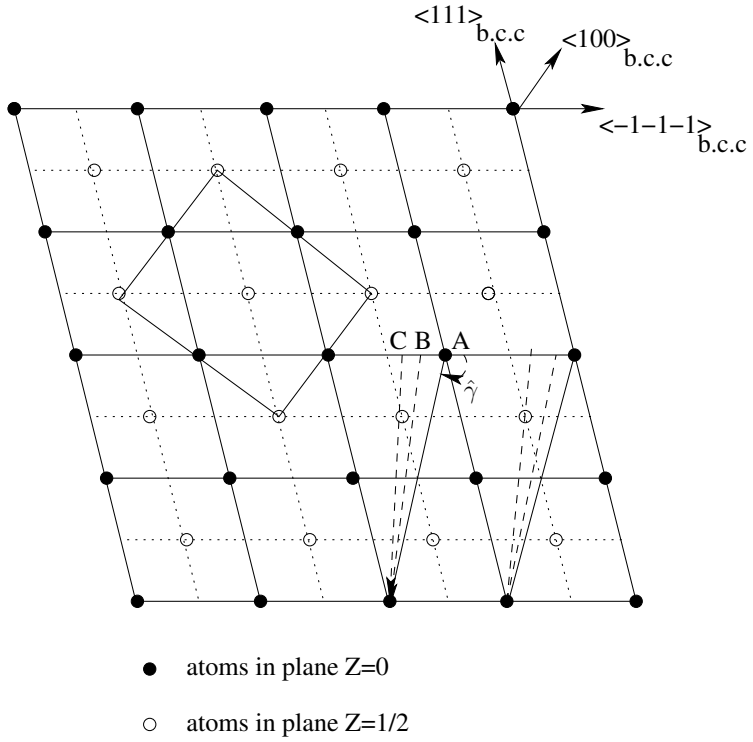

Fig. 2.3.: Projection of atoms in b.c.c structure on (110) b.c.c plane.

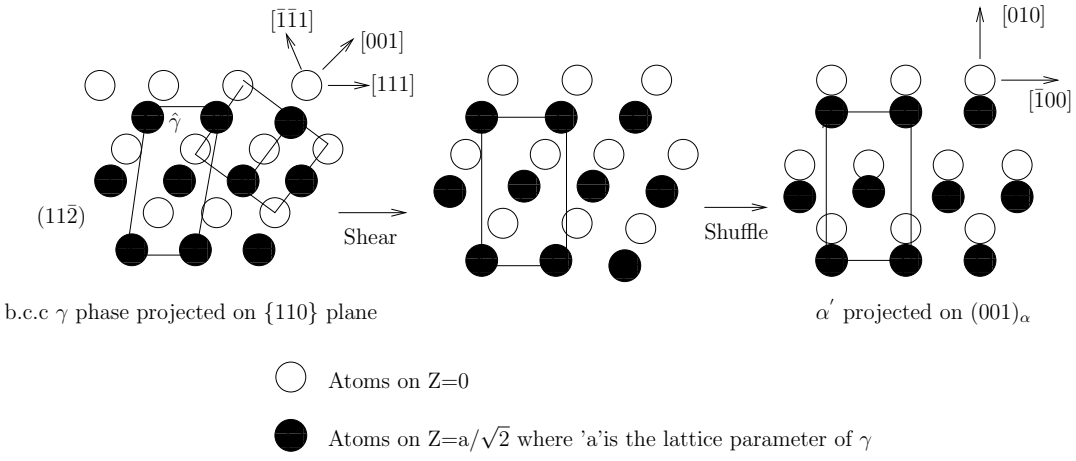

Fig. 2.4.: Schematic of $\gamma \rightarrow \alpha'$ transformation along with shuffles

These metastable phases have been observed in U-Nb [45, 52–59], U-Mo [50, 60–65], U-Ti [65, 66], U-Ru [67, 68], and U-Re [69] systems. In these systems, it was observed that formation of the metastable phases depends on both composition and the cooling rate from γ phase. However, not all phases are observed in every system. According to Tangri's model [51], the effect of increasing the solute content is to stiffen the uranium lattice making it more resistent to shear while the effect of increasing cooling rate is to favor the shear process. So, for a given solute content, slow cooling could produce a less distorted (with respect to γ) metastable phase, say γ^o because of a resistance to shear while fast quenching would produce a more distorted metastable phase, say $\alpha^{''}$, and at still higher quenching rates, $\alpha^{'}$ will form. So, at high quench rates if $\alpha^{'}$ is formed at room temperature, there should be a smooth change in $\hat{\gamma}$ angle and also a change from one structure to another progressively without coexistence of the metastable phases [58]. However, an abrupt change in $\hat{\gamma}$ has been observed in U-Re and U-Nb alloys [55, 58, 69] on the onset of $\alpha^{''}$ at a particular composition. In addition, the coexistence of γ^o and $\alpha^{''}$ was observed in U-Nb and U-Ti alloys [58, 66], and γ^o and $\alpha^{'}$ in U-Ru alloys [67]. Using quenching dilatometry, it has been shown that γ transforms to $\alpha^{''}$ via γ^0 and and both transformations, i.e, $\gamma \rightarrow \gamma^o$ and $\gamma^o \rightarrow \alpha^{''}$ are displacive (martensitic) in nature [53, 54].

Attempts have been made to solve the $\gamma \rightarrow \alpha^{'}/\alpha^{''}$ shear transformation using phenomenological theory of martensitic transformations[4] [70–76]. In order to apply this theory, a lattice correspondence[5] needs to be formulated between the parent phase and the transformed daughter phase. This usually is obtained by inspection for simple crystal structures [70, 71, 75, 76] but is more challenging for transformations between systems involving lower crystal symmetry (ex: orthorhombic crystal structure in the case of uranium alloys). Lattice correspondences for $\gamma \rightarrow \alpha^{'}$ were proposed by Christian [77] who used the correspondence for Au-Cd cubic $\rightarrow$ or-

[4]For an excellent review on crystallography of martensitic transformations, refer to [70].

[5]Lattice correspondence for a transformation specifies which vectors in the parent phase are transformed to which vectors in product phase.

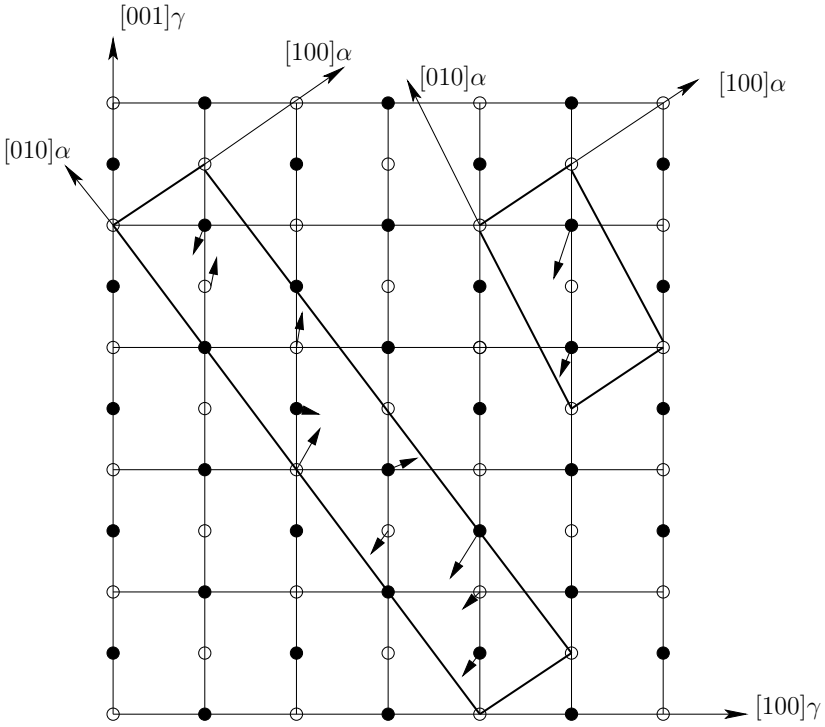

Fig. 2.5.: Lattice correspondences projected on $(110)_\gamma$, of Speer-Edmonds (left) and May (right) with the shuffles shown by arrows

thorhombic correspondence, by May [78], and by Speer and Edmonds [65, 79] who derived the correspondence matrix from the work of Hatt and Giraud et al [48, 80].

Based on the correspondences by Christian [77] and May [78], a comprehensive theoretical work has been performed by Crocker and Ross [81, 82] who showed that May's correspondence involved smaller principal strains[6] and shuffles[7] than those for Christian's correspondence. However, they have shown that May's correspondence produced imaginary solutions on applying crystallographic theories [83–85]. The cor-

[6]Principal strains can be calculated using lattice correspondence and the lattice parameters of the two phases associated in the transformation [77].

[7]For multiple lattice structures as in uranium which contain more than one atom per lattice site, the shear only takes certain number of atoms from the parent to product and transformation is completed with some shuffling of atoms. Since these are diffusionless transformations, smaller principal strains and simple shuffles are preferred. Larger strains and complicated shuffles mean that the transformation loses the diffusionless character [72].

respondence by Speer and Edmonds [65, 79] had lower principal strains than May's but lacked a straightforward correspondence and involved too many shuffles. The correspondences proposed by May and by Speer and Edmonds are shown in Figure 2.5, adapted from [79]. It is seen that the unit cell in Speer-Edmonds correspondence is quite large with 3 $\alpha^{'}$ unit cells with complicated shuffles while May's correspondence is straightforward. It has been shown that in the case of deformation twinning in α-U, twins involving smaller shuffles are favored over the ones with complicated shuffles even if the strains are larger [83]. One could say that application of phenomenological martensitic theory for $\gamma \rightarrow \alpha^{'}/\alpha^{''}$ transformation had limited success and it was remarked that this theory may not be applicable to all transformations having martensitic characteristics [81].

2.2.2 $\beta \rightarrow \alpha^{'}$ Transformation

Since none of the experiments in present research involved quenching the alloys from $(\beta + \gamma)$ phase field, $\beta \rightarrow \alpha^{'}$ transformation will be addressed only to the extent where it seems complete within the context of transformations in U alloys. Relatively few publications exist in which this transformation was studied [86–89]. Butcher et al [86] have reported orientation relationship for the $\beta \rightarrow \alpha^{'}$ transformation and the habit plane from the results on U-1.4at%Cr alloy while Lomer [87] theoretically determined lattice correspondences for the transformations. Considering the complexity of working out a correspondence which would need simple atom movements for transforming the unit cell of β-U which has 30 atoms per unit cell [29, 32] to α-U which has 4 atoms per unit cell, he came up with a correspondence[8] which had small strains. Dayan et al [88, 89], by considering U-1.5at%Ga alloy observed a new habit plane different from the one proposed by Butcher et al [86] and tried to explain the observation theoretically by using double shear mechanism.

[8]He examined 1600 possibilities

2.2.3 ω Phase in Zr and it's Alloys

The occurrence and formation mechanism of ω phase is discussed as it occurs as a metastable phase in Zr-alloys and also because of it's relationship[9] with δ phase which is a stable phase in the U-Zr system. In addition, the ω phase plays a prominent role in the data generated by this study and appears to form profusely as a metastable structure in γ-quenched U-Zr alloys. The crystal structure trend (i.e, h.c.p $\rightarrow$ b.c.c $\rightarrow$ h.c.p $\rightarrow$ f.c.c) has been explained based on the variation of number of valence d-band electrons with atomic number and by application of pressure by Pettifor and Moriarty [90, 91]. This is shown in Table 2.1 where the crystal structure trend as a function of d-band occupancy can be clearly seen [92]. The increase in d-band occupancy with increasing pressure is a consequence of $sp \rightarrow d$ transfer of valence electrons as explained by Moriarty [91]. This in turn has been used to explain the transformation sequence h.c.p $\rightarrow \omega \rightarrow$ b.c.c for Ti, Zr, and Hf both on application of pressure and alloying by Vohra [93].

Omega phase, which is metastable, occurs in all Ti and Zr alloy systems in which the high temperature b.c.c phase can be stabilized at room temperature by rapid quenching [94]. This form of ω is called athermal omega and has been found to be insuppressible even at ultra-high quench rates of 11,000^{o}C/s [95]. Other forms of the omega phase are also observed to form, including isothermal omega obtained by annealing the metastable b.c.c phase and irradiation-induced omega [94, 96, 97]. The crystal structure of ω has been first described by Silcock [98] and Bagaryatskyi [99] independently to be C32-hexagonal with atomic positions being at (0, 0, 0), ($\frac{2}{3}$, $\frac{1}{3}$,$\frac{1}{2}$), and ($\frac{1}{3}$, $\frac{2}{3}$, $\frac{1}{2}$). The formation of ω from the parent b.c.c phase is accomplished by extremely small atomic movements (explained in next Section) [98] and a characteristic feature of ω phase is it's brittleness [100] which has implications on mechanical properties of Ti and Zr alloys.

[9] δ phase is partially ordered ω phase with Zr atoms occupying special lattice positions. This is discussed in greater detail in next Section.

Table 2.1: Sequences of structural transitions in transition metals as a function of their d-band occupancy

3	4	5	6	7
Sc$[3d^1 4s^2]$	Ti$[3d^2 4s^2]$	V$[3d^3 4s^2]$	Cr$[3d^5 4s^2]$	Mn$[4s^2 3d^5]$
Y$[4d^1 5s^2]$	Zr$[5s^2 4d^2]$	Nb$[4d^4 5s^1]$	Mo$[5s^1 4d^6]$	Tc$[4d^5 5s^2]$
$[La]$	Hf$[4f^{14} 5d^2 6s^2]$	Ta$[4f^{14} 5d^3 6s^2]$	W$[4f^{14} 5d^4 6s^2]$	Re$[4f^{14} 5d^5 6s^2]$
h.c.p	h.c.p	b.c.c	b.c.c	h.c.p

2.2.4 B.C.C-$\gamma \rightarrow \omega$ Transformation and the Relationship Between ω and δ

The transformation from high temperature b.c.c to C32 hexagonal crystal structure (i.e, $\gamma \rightarrow \omega$) was described by Silcock [98, 101]. The change in the structure is brought by the collapse of two intermediate $(111)_\gamma$ planes which have to move a distance of $\frac{1}{12}[111]a_\gamma$ in opposite directions with the third plane unaltered to form an intermediate $(0001)_\omega$ plane. This is shown in Figure 2.6, adapted from [102]. The schematic on the left shown in this figure is a projection of atoms on $(111)_\gamma$ plane and the middle schematic is an edge-on view of these planes. The rightmost schematic is again $(111)_\gamma$ projection showing the honeycomb structure of the ω phase. From this figure, it can be seen that in the initial stacking sequence $ABCABC$ of the $\{111\}_\gamma$ planes, the intermediate $\{111\}_\gamma$ planes B and C collapse to form a (0001) plane $B^{'}$ in ω phase with $AB^{'}AB^{'}$ stacking sequence.

De Fontaine [103] in a theoretical study, has shown that the most probable type of instability occuring in a b.c.c lattice is the one which would cause the $\gamma \rightarrow \omega$ transformation. Hatt and Roberts, in their study on ω phase formation in Zr alloys [104, 105], have observed formation of a sequence of phases as a function of the solute content (solutes studied were Cr, V, Nb, and U) when the alloys were quenched from high temperature b.c.c phase. At low solute concentrations (Zr rich end of the

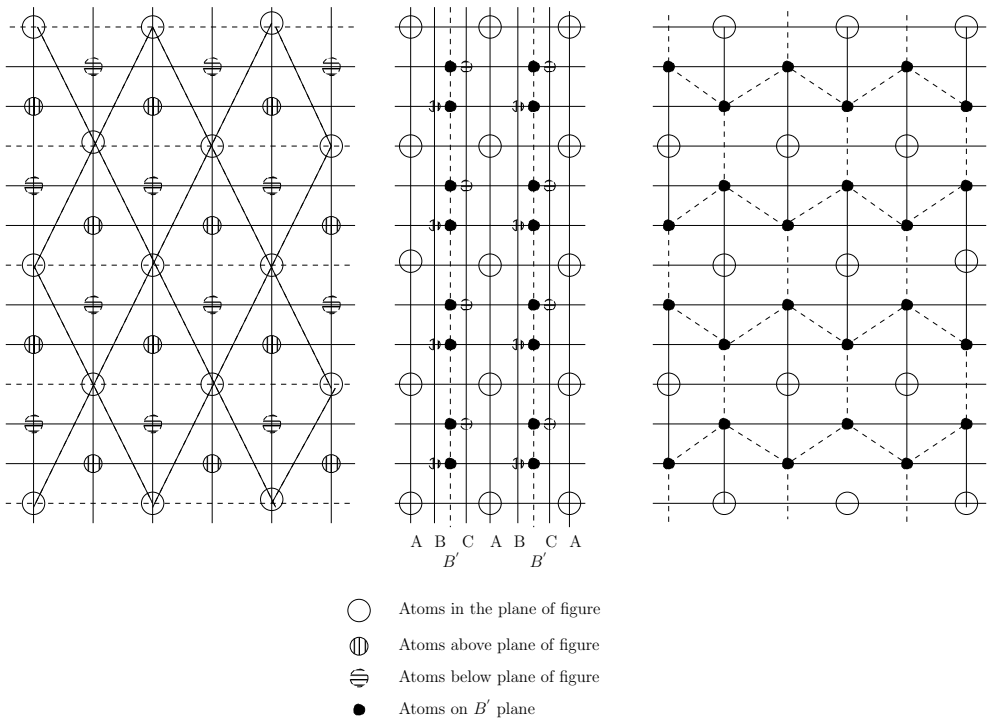

Fig. 2.6.: Formation of ω from b.c.c-γ by the collapse of $\{111\}$ planes

corresponding phase diagram), α-Zr is retained at room temperature while at higher solute content ω phase along with α-Zr are obtained. At still higher concentrations, 100 per cent ω can be obtained. As one proceeds to the solute-rich end, ω phase is retained which does not produce sharp X$-$ray diffractions and is called diffuse ω and lacks long range order. With increasing solute content, diffuseness increases albeit ω phase volume fraction present might be as high as 70 percent [104]. The diffuseness observed through negligible XRD resolution has been attributed to the incomplete collapse of the $\{111\}_\gamma$ planes. In other words, the planes fail to reach $B^{'}$ shown in Figure 2.6 and the structure referred to as *rumpled-*ω or *diffuse-*ω is formed [95, 98, 99, 104]. Another view adapted from [106], depecting both b.c.c and ω crystal structures is shown in Figure 2.7.

In contrast to the metastable ω phase, the δ phase found in the U-Zr system is a stable phase and is a partially ordered ω phase [107, 108] with C32-AlB_2 type structure. In this phase, Zr atom occupies the (0, 0, 0) position and U and Zr atoms randomly occupy the ($\frac{2}{3}$, $\frac{1}{3}$, $\frac{1}{2}$) and ($\frac{1}{3}$, $\frac{2}{3}$, $\frac{1}{2}$) sites [107–110].

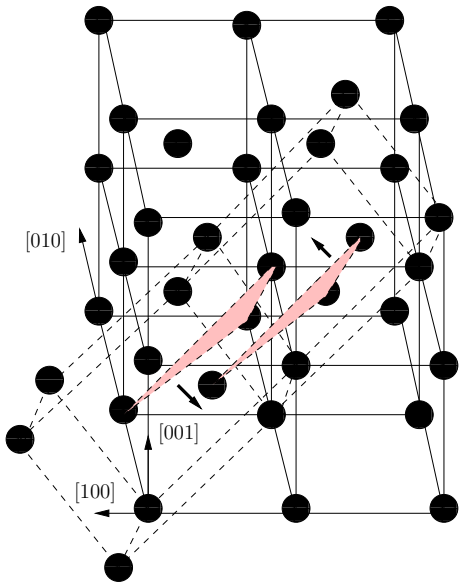

Fig. 2.7.: Collapse of (111) planes in b.c.c (colored) to form (0001) planes of ω. Unit cells of b.c.c-γ are shown in full lines while those of ω are shown by broken lines

This can be seen in Figure 2.8 where dark circles represent Zr atoms at (0, 0, 0) position while open circles and rectangles are randomly occupied by U and Zr at ($\frac{2}{3}$, $\frac{1}{3}$, $\frac{1}{2}$) and ($\frac{1}{3}$, $\frac{2}{3}$, $\frac{1}{2}$). This partial ordering has been shown to be a more stable configuration as compared to complete ordering[10] [111, 112]. The lattice parameters shown in Figure 2.8 correspond to those of high temperature b.c.c phase obtained at 702^{o}C and of δ phase [109]. The lattice parameters of δ phase are calculated using the relationship[11] between b.c.c and δ lattice parameters [109]:

[10]Complete ordering refers to U atoms occupying the dark circles and Zr atoms occupying open circles and rectangles, resulting in the UZr_2 compound.

[11]The lattice parameter of γ phase is a_γ=3.592 $\mathring{A}$ and using the relation between the lattice parameters of b.c.c and δ, a_δ=5.0798 $\mathring{A}$ and c_δ=3.110 $\mathring{A}$. The distance between <111> planes is 1.037

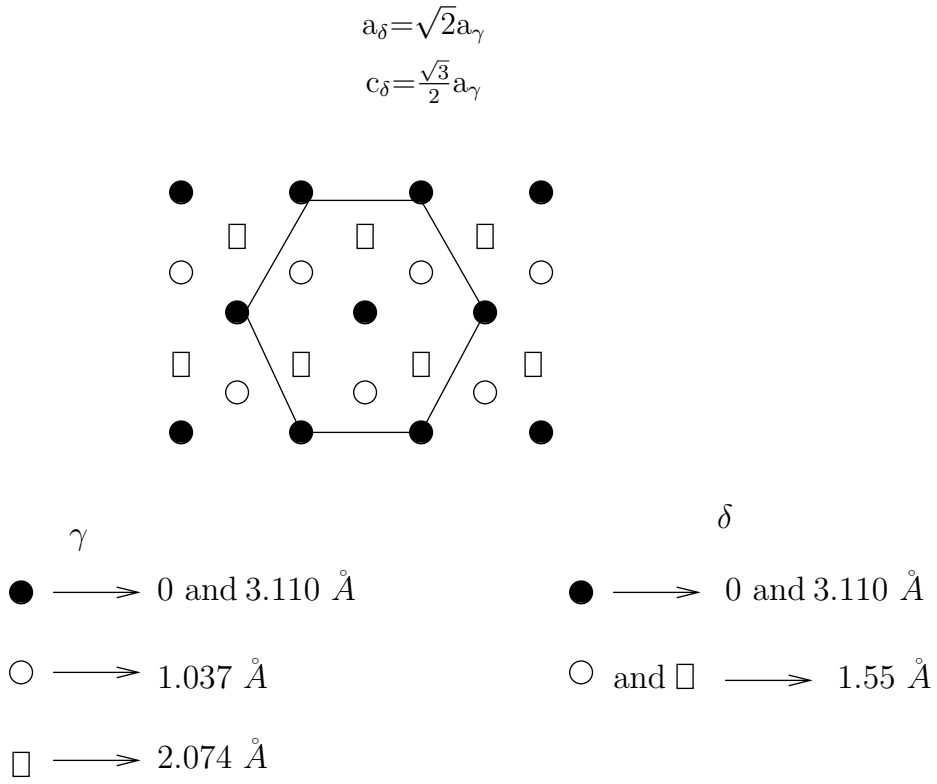

Fig. 2.8.: Projection of atomic positions on $(111)_\gamma$ and $(0001)_\delta$

2.3 The U-Zr System

The U-Zr system has been studied in the past by several investigators [113–118] and the equilibrium phase diagram assessed by Sheldon and Peterson [119] is shown[12] in Figure 2.9. The assessed phase diagram however is not without any controversies. The phase boundaries have been shown to be affected due to the presence of oxygen and nitrogen [115, 118].

Å. So, two successive [111] planes collapse to form an intermediate plane by moving a distance of $\frac{1}{12}[111]a_\gamma$=0.518 Å in opposite directions (1.037 + 0.518 and 2.074 − 0.518). Hence the intermediate plane is at 1.55 Å as shown in Figure 2.8.

[12]Bulletin of Alloy Phase Diagrams, Vol.10, 1989, p.165, The U-Zr (Uranium-Zirconium) System, R. I. Sheldon and D.E. Peterson, Figure: 1. With kind permission from Springer Science+Business Media B.V.

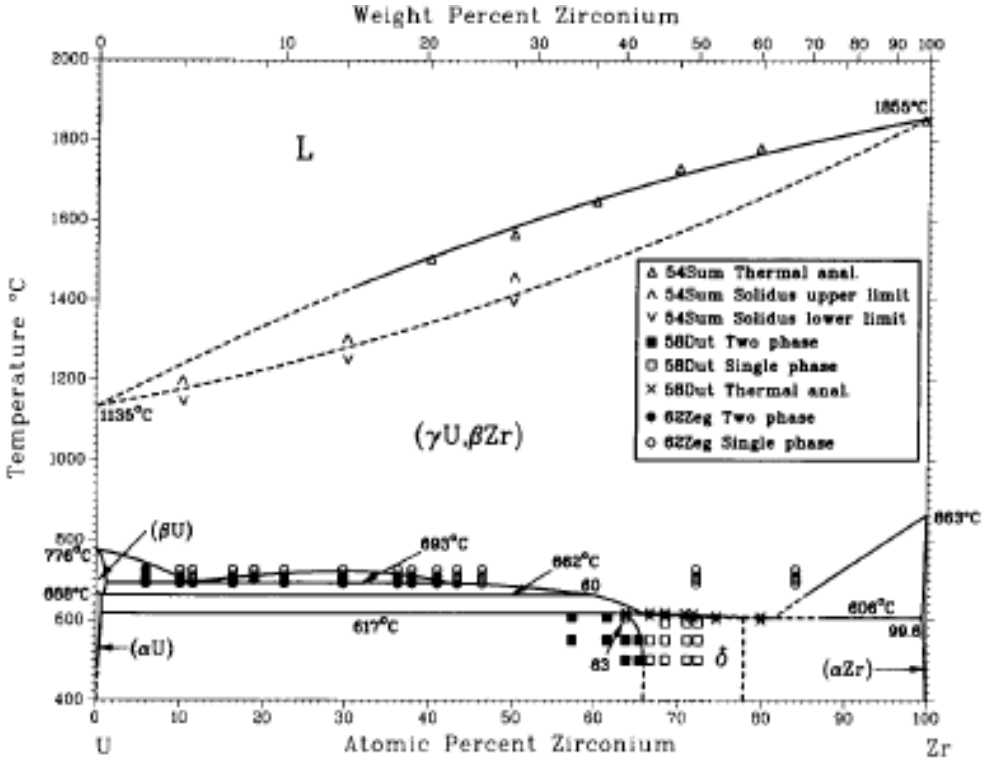

Fig. 2.9.: Assessed phase diagram of U-Zr system by Sheldon

The phase diagram by Sheldon and Peterson [119] was assessed using the experimental data obtained by several investigators, principally from [113–118]. It has the drawback of gleaning the information from data which have been generated by researchers using different source materials of varying purity. Data obtained in the present research indicates a possible discrepancy in the extent spanned by $(\beta + \gamma)$ phase field and the stability of δ phase at 600^oC needs further investigation as well. Considering the above, it can be concluded that without a quantitative impurity analysis, a strong statement regarding the fidelity of the current accepted phase diagram cannot be made.

An initial controversy regarding the stability of δ phase was resolved by Duffey et al [116], Holden et al [117] and more recently by Akabori et al [109,110] by metallog-

raphy, dilatometry, and high temperature XRD. Rather than being an intermetallic line compound (UZr_2) with 56.6 and 43.4 wt% of U and Zr respectively, it exists over a compositional range. At 600^{o}C, the Zr content in the δ phase was reported to range between 40.7 to 57.8 wt% while the room temperature values could not be determined [110].

It is interesting to note that there is no published literature on low temperature synthesis of δ phase except for the technical report published by Rough [120] in which it was mentioned that δ phase formed after annealing compacted powders of α-U and α-Zr at 540^{o}C. However, no data on the pressure used for compaction was provided. It must be noted that pressure induced ω transformation occurs in elemental zirconium at $\sim$3 GPa depending on the impurities present and this pressure range is not uncommon while making U-Zr pellets via powder metallurgy route[13]. With such high pressures, formation of ω and probably b.c.c phase cannot be ruled out. Without confirmatory experiments, it still appears that δ phase forms as a transitioning phase from high temperature b.c.c phase. Literature on phase transformations in U-Zr system will be further reviewed while discussing the results from present investigation. The transformation temperatures along with pertinent reaction types involved in U-Zr system are shown in Table 2.2 [119].

[13]In some experiments conducted in our lab on α phase sintering of U-Zr alloys, pressures of $\sim$625 GPa were used [121]. It has been established experimentally that $\omega \rightarrow b.c.c$ occurs at $\sim$35$\pm$5 GPa at room temperature [92].

Table 2.2: Transformation temperatures and the reaction types in U-Zr system

Reaction	Composition of Zr in respective phases			Temperature (C)	Reaction type
	(wt%)	(wt%)	(wt%)		
L$\longleftrightarrow$U	-	0	-	1135	Freezing point
γU $\longleftrightarrow$ βU	-	0	-	776	Allotropic transformation
βU $\longleftrightarrow$ αU	-	0	-	669	Allotropic transformation
$\gamma 1 \longleftrightarrow \gamma 2 + \beta$U	4.48	22	0.42	693	Monotectoid
βU $\longleftrightarrow$ αU+γ2	0.31	0.19	36.5	662†	Eutectoid
αU+γ2 $\longleftrightarrow$ δ	$\sim$0.19	$\sim$42.66	39.49	617‡	Peritectoid
$\gamma 2 \longleftrightarrow \gamma + \alpha$Zr	$\sim$62.03	$\sim$57.61	98.96	606	Eutectoid
L$\longleftrightarrow$ βZr	-	100	-	1855	Freezing point
βZr $\longleftrightarrow$ αZr	-	100	-	862	Allotropic transformation

†This temperature was consistently measured at $\sim 685^{o}$C in present investigation

‡Samples annealed at 600^{o}C never showed peaks for δ phase in XRD data as will be discussed later

3. EXPERIMENTAL METHODS AND ANALYSES

In this chapter, melt casting of the U-Zr alloys, heat treatment procedures, and optimized sample preparation methods for various characterization techniques (Electron Probe Micro Analysis (EPMA), optical imaging, X-ray diffraction (XRD), Differential Scanning Calorimetry (DSC), Transmission Electron Microscopy (TEM) will be discussed. Depleted uranium was used for all experiments.

3.1 Alloy Preparation

Prior to melt casting, depleted uranium (DU) chunks were cleaned thoroughly to remove the oxide layer that formed during storage. The procedure involved immersing DU chunks in 25 vol% nitric acid followed by cleaning with deionized water and ethanol after the chunks turned silvery in color. This was carried out in an argon filled glove bag to minimize re-oxidation before melt casting. Acid washed DU chunks and crystal bar zirconium were then weighed and prepared in proportion (for 2, 5, 10, 20, 30, and 50 wt%Zr alloys) and melt cast in yttrium oxide crucibles under argon atmosphere in a high temperature furnace. A heating rate of 50^oC/min was employed and the alloys were held isothermally at 1900^oC for 1 hr after which they were cooled at a rate of 40^oC/min to ambient temperature. The slugs were flipped and re-melted under the same conditions to ensure homogeneity of the alloy. Henceforth, furnace cooled alloys are referred to as as-cast alloys. The as-cast cylindrical slugs were typically 3cm in length and 1.25cm in diameter. The amounts of DU and zirconium used in casting the alloys for this study are shown in Table 3.1. Figures 3.1a and 3.1b show the furnace used for casting the alloys and typical as-cast alloy slugs.

Two features were seen in the microstructures of as-cast alloys. One is the variation in Zr content because of macro-segrigation in the alloy, and the other is the

Table 3.1: Weights of DU and Zr used in casting the alloys

Alloy Composition	DU (gm)	Zr (gm)
U-2wt%Zr	40.6069	0.8472
U-5wt%Zr	54.3520	2.8808
U-10wt%Zr	41.2332	4.6
U-20wt%Zr	25.740	6.5417
U-30wt%Zr	28.5021	12.0751
U-50wt%Zr	12.940	12.99

formation of yttrium oxide and Zr rich precipitates. Macro-segregation occurred during melting, which lead to chemical banding [58, 122].

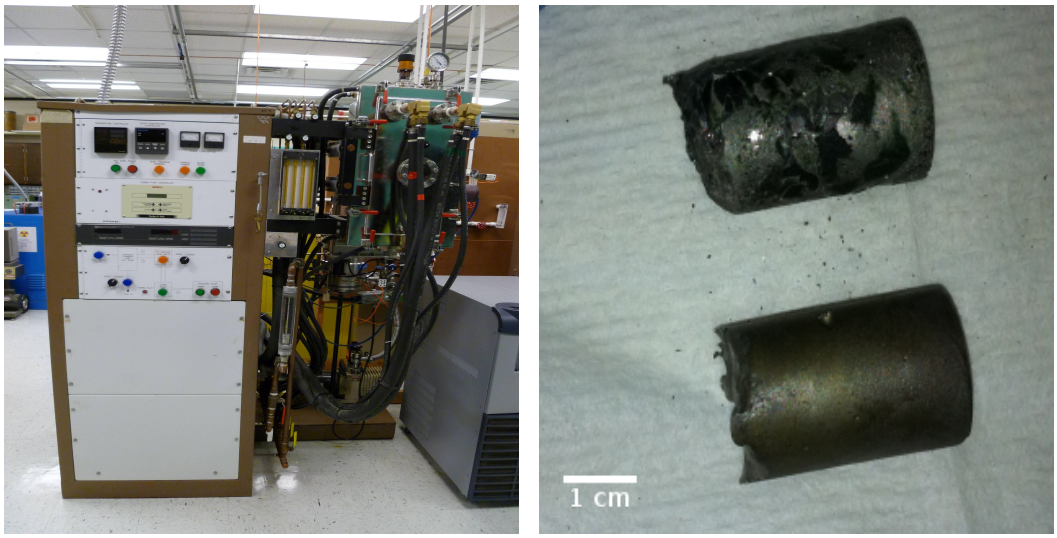

(a) High temperature furnace used for casting the alloys

(b) As cast alloy slugs

Fig. 3.1.: Melt casting of U-Zr alloys

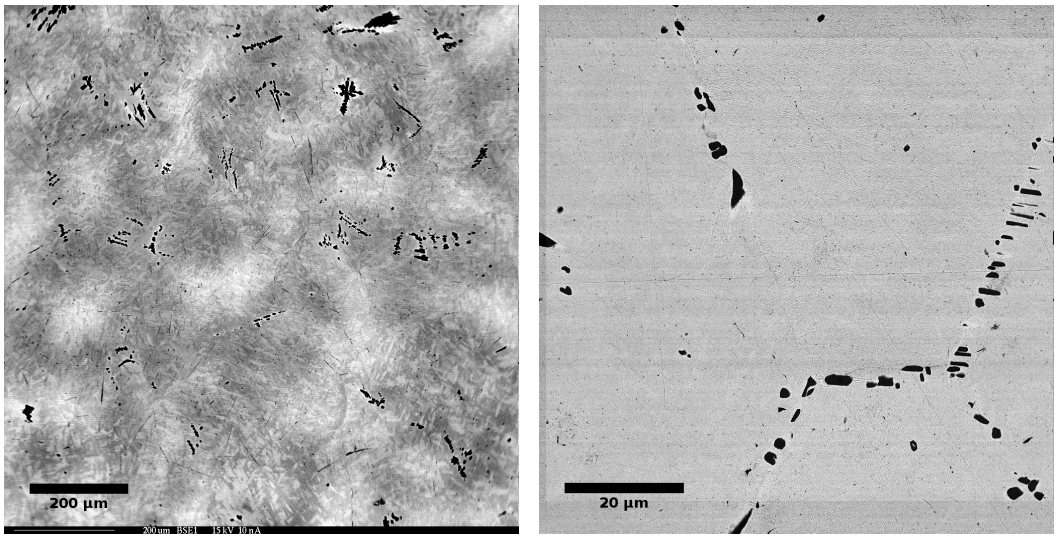

(a) Macro-segregation of Zr seen as bright and dark regions

(b) Oxygen stabilized Zr rich precipitates

Fig. 3.2.: Microstructural features of as-cast U-10wt%Zr alloy

The Zr precipitates are consistent with impurity stabilized α-Zr observed in other studies [14]. These phases have the impact of depleting the bulk material of Zr while internally gettering impurities and thus moderately purifying the alloy.

Table 3.2: WDS analysis indicating macro-segregation of Zr in U-10wt%Zr alloy

Region	Bright		Dark	
	U (wt%)	Zr (wt%)	U (wt%)	Zr (wt%)
1	95.32	6.21	93.12	8.76
2	95.35	6.32	91.44	10.54
3	94.30	7.05	89.90	11.71
4	94.95	6.27	87.84	12.82
5	94.93	5.81	90.04	11.42

The precipitates primarily consisted of yttrium oxide incorporated into the alloy from the melt crucible and the impurity-stabilized Zr noted above. These phases were found to be very stable even after prolonged heat treatments. Figures 3.2a and 3.2b show macro-segregation seen as bright and dark regions in U-10wt%Zr alloy and the precipitates respectively. Table 3.2 shows wavelength dispersive spectrometry (WDS) analysis of the bright and dark areas observed in Figure 3.2a.

3.1.1 Heat Treatments of Specimens

In order to investigate phase transformations in U-Zr system, alloys were subjected to various heat treatments using different techniques. For heat treating experiments, U-Zr alloy buttons of 1mm thickness were sectioned from the slugs using a slow speed diamond saw. These buttons were cleaned and wrapped in tantalum foil. A molten salt bath was designed to quench the alloys from the γ phase in order to study diffusionless transformations. Cartecsal neutral salt (Heatbath Corporation - Park Metallurgical) was used [123]. Specifically developed for U.S DOE for heat treating uranium alloys, it has a working range between 454^oC to 954^oC. Samples were placed in a stainless steel (SS) bag and using a nichrome wire, gently suspended into the molten salt.

(a) Molten salt bath (b) Quartz tube sealing

Fig. 3.3.: U-Zr alloy sample heat treatments

After holding at 850^{o}C for 30 min, the SS bag was quickly dropped into ice water for quenching. Figure 3.3a shows the set up of the molten salt bath, with the inset showing top view of the molten salt. For annealing experiments, the alloy buttons were wrapped in tantalum foil and vacuum sealed in a quartz tube and annealed in a furnace at various temperatures depending on the objective of the investigation. Figure 3.3b shows the set up for sealing the quartz tubes along with the inset showing a sealed quartz tube ready to be put in a furnace.

Thermal profiles studied and the corresponding objectives are summarized below:

- Alloys quenched from γ phase (850^{o}C, salt bath): To investigate phases obtained via diffusionless transformation.
- As-cast alloys (furnace cooled after melt casting): To investigate phases formed when cooled slowly from γ phase.
- As-cast alloys annealed for 1, 3, 7, and 30 days at 600^{o}C and furnace cooled: To investigate isothermal growth kinetics of δ phase.

- Gamma quenched alloys annealed for 1, 3, 7, and 30 days at 600^{o}C and furnace cooled: To investigate decomposition/isothermal growth kinetics of quenched-in phases.

- Alloys step cooled from γ phase and annealed 650^{o}C for 3 days and quenched: To investigate the retention of α and γ phases.

- Alloys step cooled from γ phase to 650^{o}C, held for 2 days, and then to 600^{o}C, held for 3 days and furnace cooled: To investigate the formation of δ phase.

3.2 Specimen Sample Preparation

In order to characterize the alloys, EPMA, optical microscopy, XRD, DSC, and TEM were used. Since sample preparation is a crucial step for obtaining best possible results, methods have been optimized for U-Zr alloys and will be discussed here.

3.2.1 Electron Probe Micro Analysis

Back scattered electron (BSE) imaging and compositional analysis of elements in various phases using WDS analysis was carried out using EPMA. The electron microprobe at the Geology Department of Texas A&M University was used for this purpose. For metallographic examination (BSE, WDS, and optical imaging), samples were mounted on cold setting epoxy resin and polished using a Buehler [1] MiniMet® semi-automatic grinder-polisher. The polishing steps shown in Table 3.3 gave excellent micrographs with little or no visible scratches on the sample surfaces.

[1] MiniMet®, CarbiMet®, MetaDi®, MicroCloth® are products of Buehler

Table 3.3: Metallographic preparation steps for U-Zr alloys

Step	Description
Grinding	Sequentially grind with 180, 240, 320, 400, and 600 grit CarbiMet® SiC abrasive discs with 4 lbs force, for 3.5 min, at 35 rpm using water as lubricant
Rough polishing	Polish with 800 and then with 1200 grit CarbiMet® SiC abrasive discs with 3 lbs force, for 3.5 min, at 30 rpm using water as lubricant
Fine polishing	Polish with 3 and then with 1μm MetaDi® oil based diamond suspensions on a MicroCloth® with 3 lbs force, for 15 min, at 30 rpm
Final polishing	Polish with $\frac{1}{4}\mu$m MetaDi® oil based diamond suspension on a MicroCloth® with 3 lbs force, for 15 min, at 30 rpm
Electropolishing	Using 5% phosphoric acid, electropolish at 3 V for 4 s with SS cathode and tantalum wire touching the specimen as anode
Electroetching	Using 10% oxalic acid, electroetch at 4 V for 4 s with SS cathode and tantalum wire touching the specimen as anode

After each step of grinding/polishing, the sample mount was thoroughly cleaned using ultrasonic cleaner with ethanol. This ensured that no SiC particles stuck to the sample surface when proceeding to higher grit sizes. After $\frac{1}{4}\mu$m finish, samples were carbon coated before mounting into the sample chamber in EPMA so as to reduce surface oxidation. BSE images were acquired with an accelerating voltage of 15 kV and a current of 1 nA, while for WDS analysis, the parameters were 15 kV and 20 nA. For all compositional analysis using WDS, data from at least 5 locations were collected and averaged. The error associated is $\pm$ 1 to 2% of the amount present.

Electropolishing and Electroetching were carried out only when optical images were to be taken.

3.2.2 Optical Microscopy

When quenched from γ phase, samples undergo diffusionless transformation and there is little time for diffusion of chemical species to form equilibrium phases at room temperature. In such a scenario, BSE images don't produce any conspicuous features (contrast in BSE images is due to difference in atomic number of the elements present) and optical imaging with Differential Interference Contrast (DIC) serves as the best tool for metallographic examination. For DIC imaging, samples were electropolished and electroetched as suggested in [122]. A Zeiss Axiophot optical microscope at the Microscopy and Imaging Center (MIC), Texas A&M University was used to obtain images.

3.2.3 X-ray Diffraction

In order to obtain crystallographic information on the phases present in the alloys after heat treatments, XRD was used. Majority of the XRD data were collected using Bruker AXS instrument at Microstructural Engineering of Structural and Active Materials lab, Mechanical Engineering department, Texas A&M University. Some data were also collected using Bruker AXS D8 instrument at University of Nevada, Las Vegas. Samples were un-mounted from the epoxy resin after EPMA analysis for XRD data collection. XRD patterns for the samples were obtained with 0.01 degrees step size, 2 s per step dwell time, and 20 to 80 degrees as the scan limits. No internal standard was used as the data were only used to identify the phases present. TOPAS[2] was used to refine lattice parameters as a function of Zr content and thermal profile of the alloys. It must however be noted that the accuracy of

[2]TOPAS is a product of Bruker

refinement was modest as bulk samples were used and data were collected without any internal standard.

3.2.4 Differential Scanning Calorimetry

Phase transitions in the alloys were investigated using a Netzsch STA 409 PC *Luxx* Differential scanning calorimeter. All measurements were taken with a heating rate of 5^oC/min with the sample placed in an alumina crucible with argon gas flowing at a rate of 50 ml/min. The system was backfilled with argon thrice before any measurement was taken. Temperature and sensitivity calibrations were performed using In, Sn, Bi, Al, and Ni standards supplied by Netzsch. Baseline measurements with empty crucibles without the sample were obtained to account for the instrument buoyancy effects that arise due to the flowing argon gas in the system. The sample was placed in one of the crucibles with the reference crucible empty and data were collected. Actual data were then obtained by subtracting the baseline signal from the data collected with the sample placed in the crucible. Enthalpies of transformation were not calculated for this study since the objective was to identify phase transition temperatures (and hence pertinent reactions involved) and glean information from them on the possible transformation sequence of the γ phase when the alloys were quenched.

3.2.5 Transmission Electron Microscopy

A TEM not only produces images at much higher magnifications and better resolution than an SEM, but also gives crystallographic information on the phases present using electron diffraction. For metallurgical characterization, it is a powerful tool to obtain information about orientation relationships (OR) between the matrix and precipitate using diffraction patterns and obtain chemical compositions of nano scale precipitates using EDS. For present research, the microscope at University of

Nevada, Las Vegas (UNLV) was used for imaging and electron diffraction and is a 300kV Tecnai G2 F30 S-TWIN TEM. Sample preparation consisted of following steps:

1. Mechanically grinding the sample button to $\sim 150\mu$m using 600 grit SiC abrasive disc on a Struers TenuPol grinder polisher.

2. Punching 3 mm discs using Fischione disc punch.

3. Dimpling using a Southbay Technology Model D500i Dimpler until the thickness of the dimpled sample was $\sim 20\mu$m.

4. Using a Low Angle Ion Mill (Fischione Instrument Model 1010 LAMP), remove the material using 5 kV, 5 mA and 14 degrees milling angle till a small hole was formed. The areas surrounding this hole were electron transparent and suitable for TEM examination.

Samples prepared using above steps gave satisfactory results. During the sample preparation process of quenched samples, it was found that they were extremely brittle and several samples crubmled during punching process. This probably was due to the presence of ω phase in quenched samples, which made them extremely brittle.

4. RESULTS

Metallurgical characterization results will be presented in this Chapter as a function of increasing alloy content (i.e, U-2Zr to U-50Zr). For a particular alloy composition, results are grouped for:

- As-cast and γ-quenched samples
- Samples step-cooled from γ phase
- Samples annealed at 600^oC

4.1 Metallurgy of U-2wt%Zr Alloy

4.1.1 As-cast and γ-Quenched Samples

The back scattered image of the as-cast U-2Zr alloy (Figure 4.1a) reveals that the alloy has a lamellar microstructure with bands of interpenetrating fine lamellae. Segregation of Zr into Zr-rich (lamellae) and Zr-lean (matrix) phases is seen as a consequence of slow cooling from γ phase. The fine structure could not be resolved in the optical image (Figure 4.1b) and only a fleck type microstructure is seen. All peaks in the XRD pattern (Figure 4.2) of as-cast alloy correspond to α-U with no indication of presence δ phase.

Back scattered image of the γ-quenched alloy (Figure 4.3a) contains small regions of varying Zr composition indicating the segregation of Zr even with rapid cooling from γ phase. Martensitic plates in the optical image (Figure 4.3b) are clearly seen with $\alpha_a^{'}$ microstructure. However, features within the individial martensitic plates (twinning or slip) could not be resolved. Figure 4.4 shows XRD pattern of the quenched alloy with peaks corresponding to only α-U.

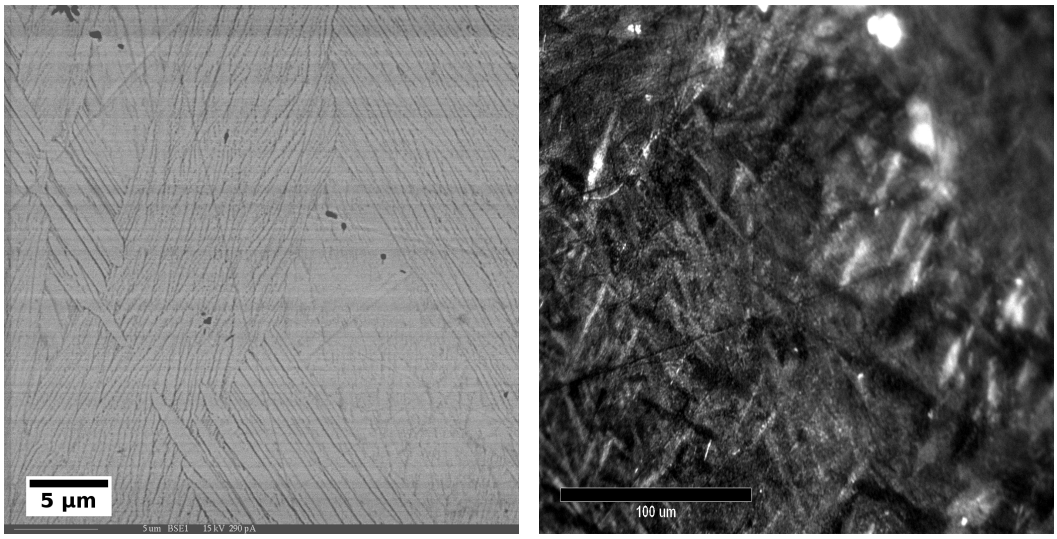

(a) BSE image (b) Optical (DIC) image

Fig. 4.1.: Back scattered and optical images of as cast U-2Zr alloy

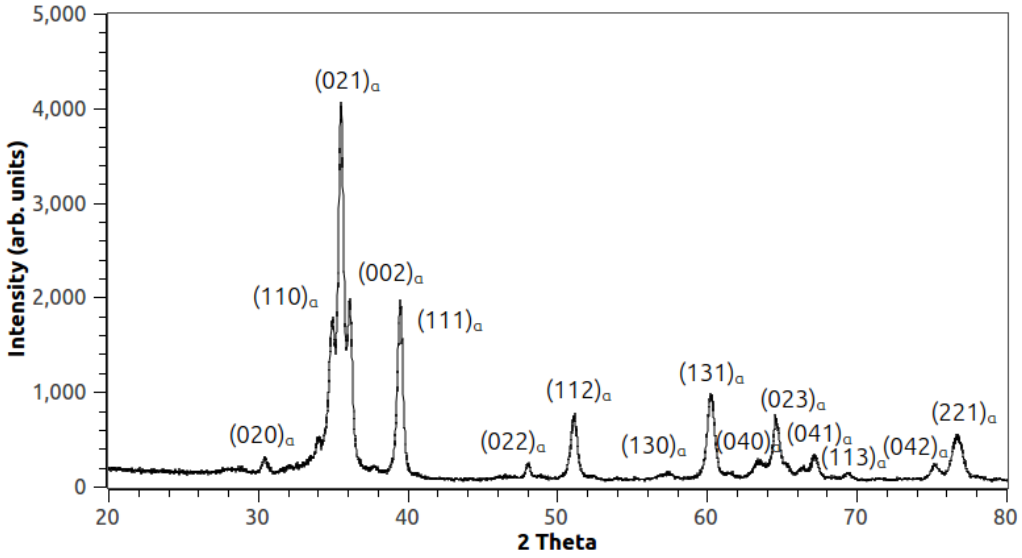

Fig. 4.2.: XRD pattern of as-cast U-2Zr alloy

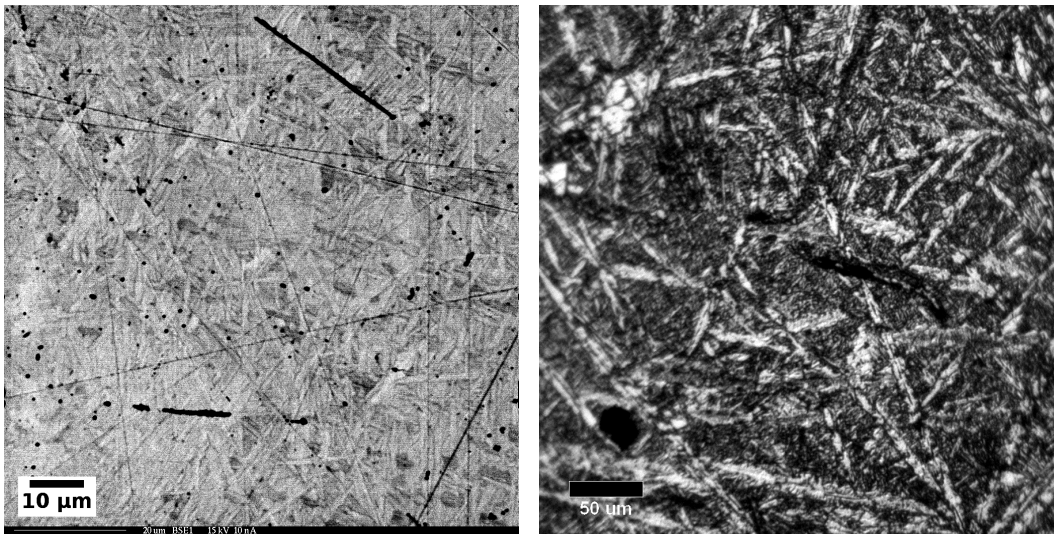

(a) BSE image (b) Optical (DIC)

Fig. 4.3.: Back scattered and optical images of γ-quenched U-2Zr alloy

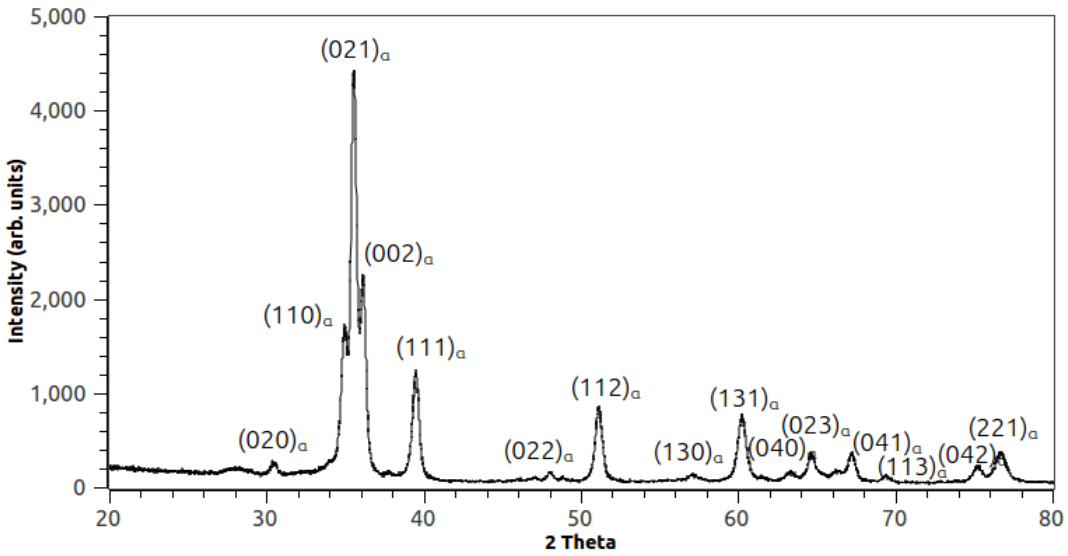

Fig. 4.4.: XRD pattern of γ-quenched U-2Zr alloy

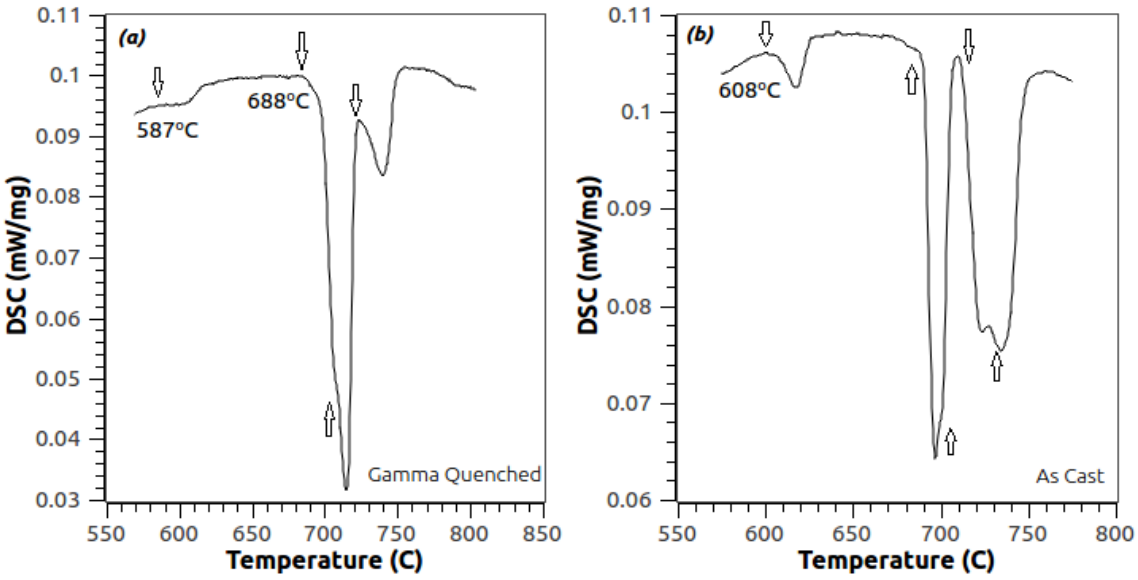

Fig. 4.5.: DSC curves of γ-quenched and as-cast U-2Zr alloy showing various transformations (indicated by arrows)

Phase transformation temperatures in quenched and as-cast alloy are indicated in the DSC curves (Figure 4.5). For the quenched alloy (Part a of Figure 4.5), the first transformation is seen at 587^{o}C followed by another transformation at 688^{o}C. A change in the slope at $\sim$ 700^{o}C is seen indicating overlapping of two transformation curves, though the precise temperature for this transformation could not be inferred. Final transformation to the γ phase is seen to occur at 725^{o}C. In the case of as-cast alloy (Part b of Figure 4.5), the first transformation occurred at 608^{o}C and the second one at 688^{o}C. Similar to the γ-quenched alloy, a change in slope is seen at $\sim$ 710^{o}C, indicating two transformations. Next two transformations which are seen as overlapping curves indicate sluggish kinetics for transformation.

4.1.2 Samples Step-Cooled from the γ Phase

Figure 4.6 shows BSE images of the alloy step cooled from γ phase. Figure 4.6a is BSE image of the alloy which was homogenized at 850^{o}C for 6 hours, step cooled to 650^{o}C i.e, in the $(\alpha + \gamma)$ phase field, and held for 2 days, step cooled to 600^{o}C i.e, in the $(\alpha + \delta)$ phase field, and held for 3 days, and then furnace cooled. Since the XRD pattern for the as-cast alloy only had peaks corresponding to α-U, this thermal profile was chosen to study δ phase formation. Precipitates rich in Zr, with sizes less than 1 μm are seen. Since the spot size of the electron microprobe was larger than the precipitate size, WDS analysis was not performed. However, WDS on the matrix phase indicated (Table 4.1) that it is α-U.

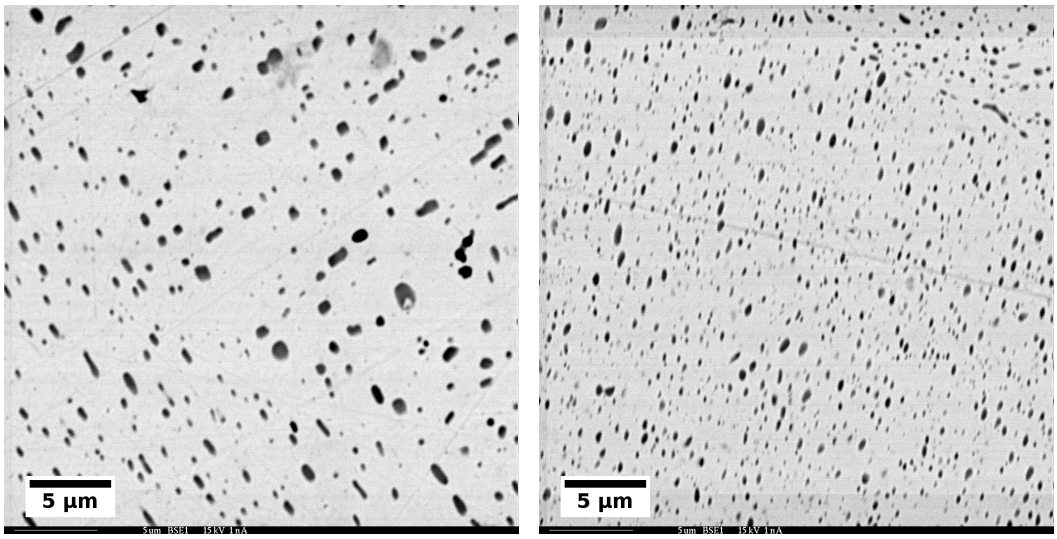

(a) $\gamma \xrightarrow[650C]{(\alpha+\gamma)}$ 2 days $\xrightarrow[600C]{(\alpha+\delta)}$ 3 days

(b) $\gamma \xrightarrow[650C]{(\alpha+\gamma)}$ 2 days and quenched

Fig. 4.6.: Back scattered images of step-cooled U-2Zr alloys

To study the microstructure of $(\alpha + \gamma)$, the sample was homogenized at 850^{o}C for 6 hours, step-cooled to 650^{o}C i.e, in the $(\alpha + \gamma)$ phase field, held for 2 days, and quenched. Figure 4.6b is the corresponding BSE image. Zr-rich precipitates of sizes

less than 0.5 μm are seen. WDS analysis on the matrix phase indicated that it is α-U. XRD patterns for both alloys are shown in Figures 4.7 and 4.8. For the alloy annealed in $(\alpha + \delta)$ phase field (i.e, $\gamma \xrightarrow[650C]{(\alpha+\gamma)}$ 2 days $\xrightarrow[600C]{(\alpha+\delta)}$ 3 days), peaks for only α-U are seen. Since the peaks for γ-U coincide with those of α-U, it was difficult to ascertain it's presence in XRD pattern of the sample annealed in $(\alpha + \gamma)$ phase field (i.e, $\gamma \xrightarrow[650C]{(\alpha+\gamma)}$ 2 days and quenched; Figure 4.8). Quantitative phase analysis on the phases present was not attempted as bulk sample was used.

Table 4.1: WDS analysis of step-cooled U-2Zr alloy

Alloy	Matrix		Precipitate	
	U (wt%)	Zr (wt%)	U (wt%)	Zr (wt%)
U-2Zr†	99.62	0.38	-	-
U-2Zr‡	99.23	0.77	-	-

†Step-cooled from $\gamma \xrightarrow[650C]{(\alpha+\gamma)}$ 2 days $\xrightarrow[600C]{(\alpha+\delta)}$ 3 days

‡Step-cooled from $\gamma \xrightarrow[650C]{(\alpha+\gamma)}$ 2 days and quenched

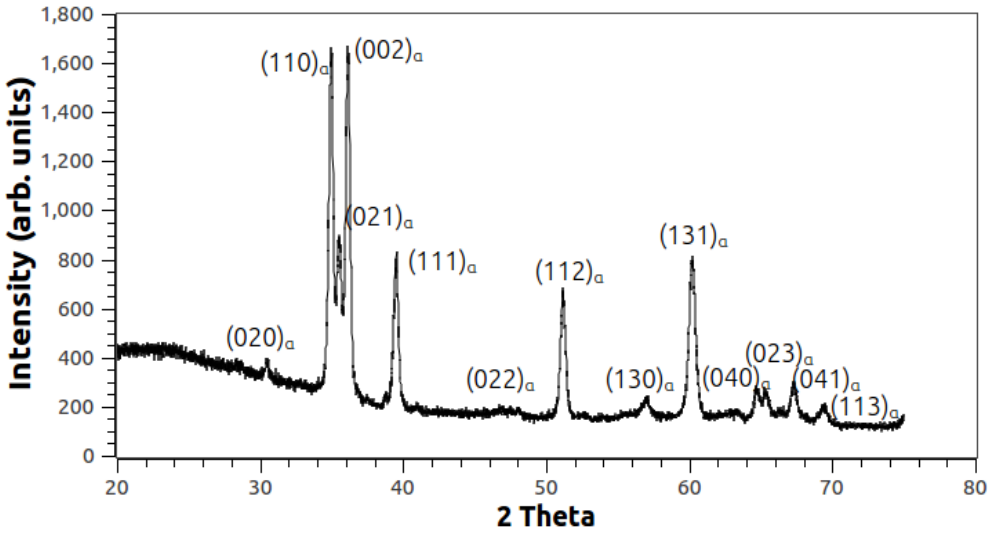

Fig. 4.7.: XRD pattern of U-2Zr alloy step-cooled from $\gamma \xrightarrow[650C]{(\alpha+\gamma)}$ 2 days $\xrightarrow[600C]{(\alpha+\delta)}$ 3 days

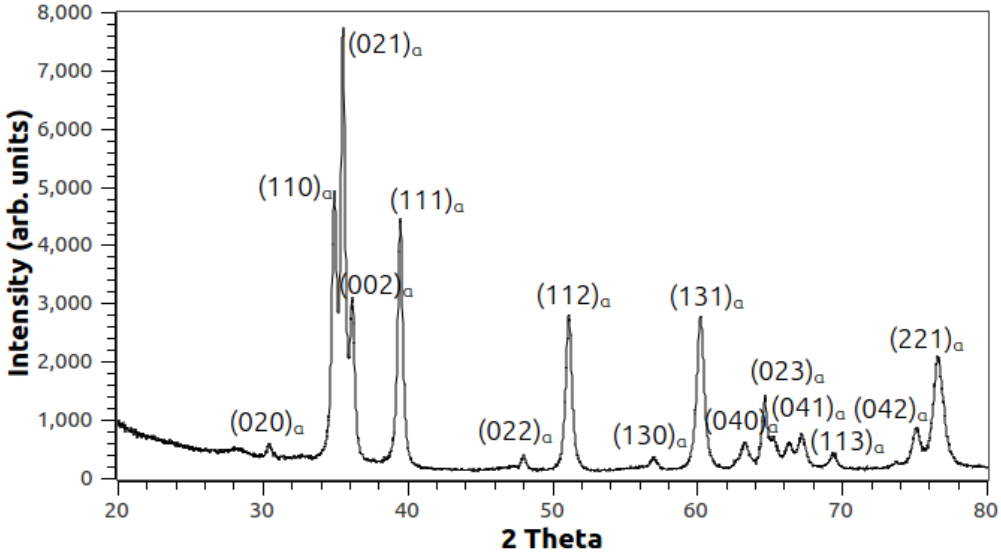

Fig. 4.8.: XRD pattern of U-2Zr alloy step-cooled from $\gamma \xrightarrow[650C]{(\alpha+\gamma)}$ 2 days and quenched

4.1.3 Samples Annealed at 600^{o}C

Both as-cast and γ-quenched alloys were annealed at 600^{o}C, in the $(\alpha + \delta)$ phase field for various times in order to study the coarsening kinetics of the Zr-rich lamellae and the quenched-in phases respectively. Figures[1] 4.9a, 4.9b, and 4.9c are the BSE images of as cast alloy annealed for 1, 7, and 30 days. Precipitates have grown as a function of time and it is seen that after 1 day anneal, a large number of small precipitates have formed while after 7 days, the number has reduced but their size has increased. After 30 days of annealing, the size of the precipitates is more or less unchanged compared to 7 day annealed sample ($\sim$ 1 μm). Initial growth rate of the precipitates is high and has fallen as a function of annealing time, which is a characteristic feature of precipitation reactions [124].

[1]Images shown in Figures 4.9a and 4.9b were taken by Sangjoon Ahn.

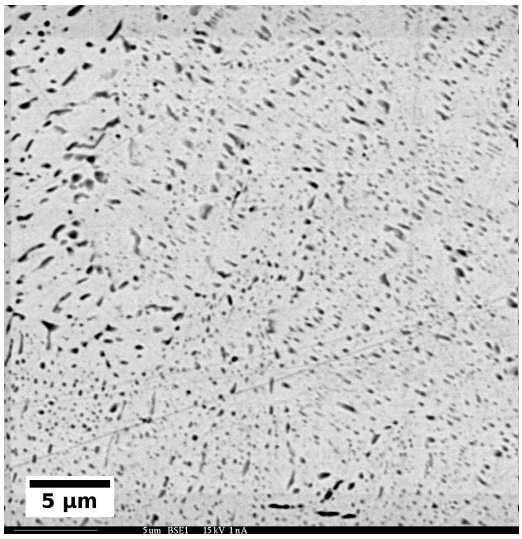

(a) Annealed for 1 day

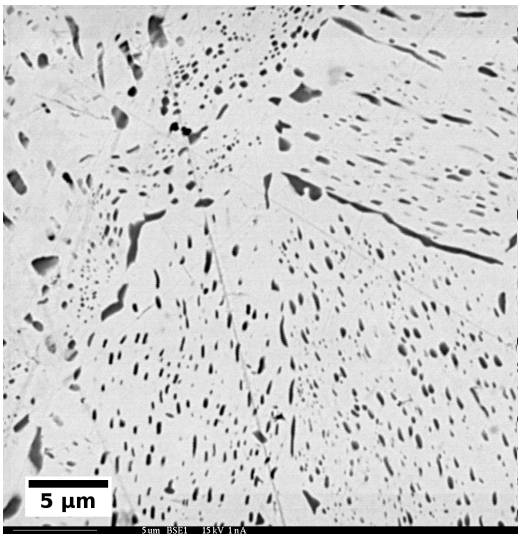

(b) Annealed for 7 days

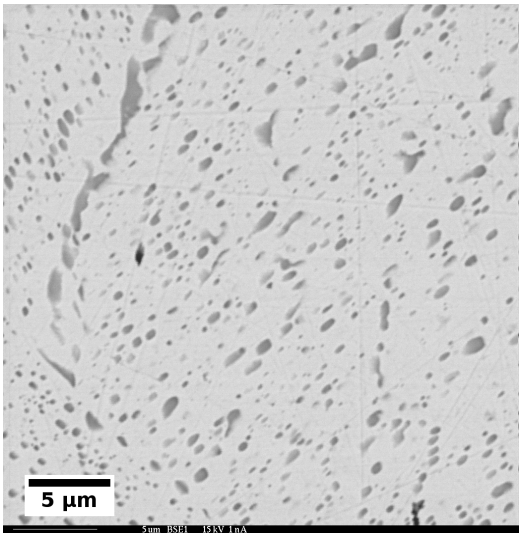

(c) Annealed for 30 days

Fig. 4.9.: Back scattered images of as-cast U-2Zr alloys annealed at 600^oC

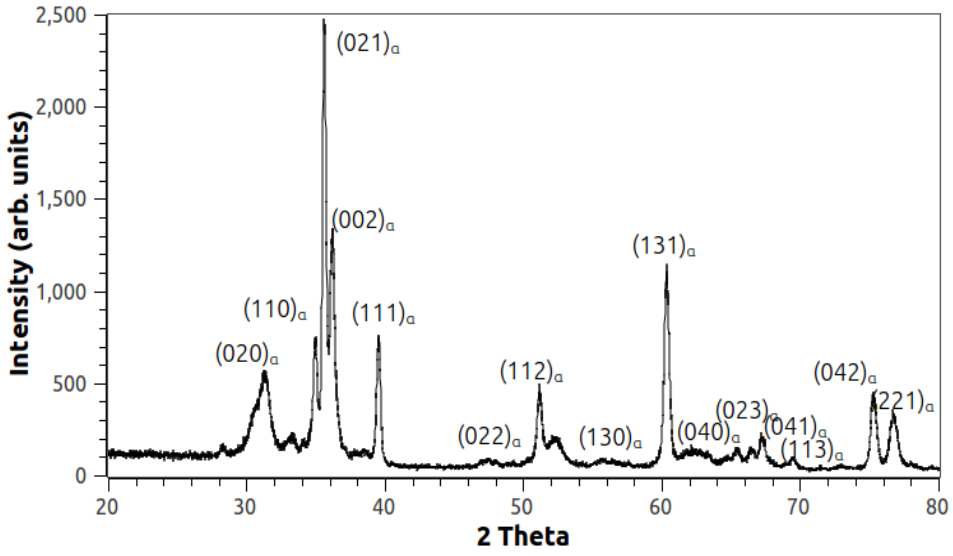

Fig. 4.10.: XRD pattern of as-cast U-2Zr alloy annealed for 7 days

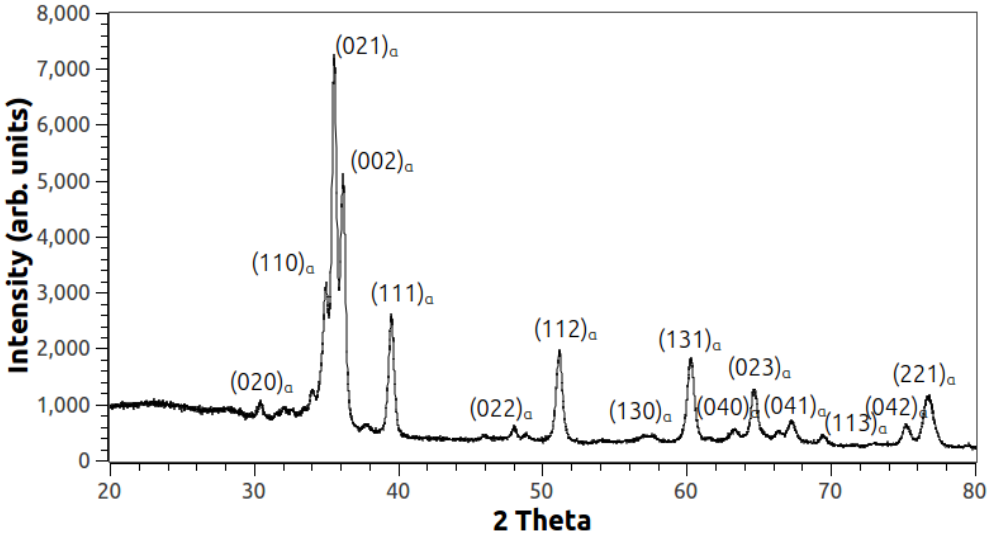

Fig. 4.11.: XRD pattern of as-cast U-2Zr alloy annealed for 30 days

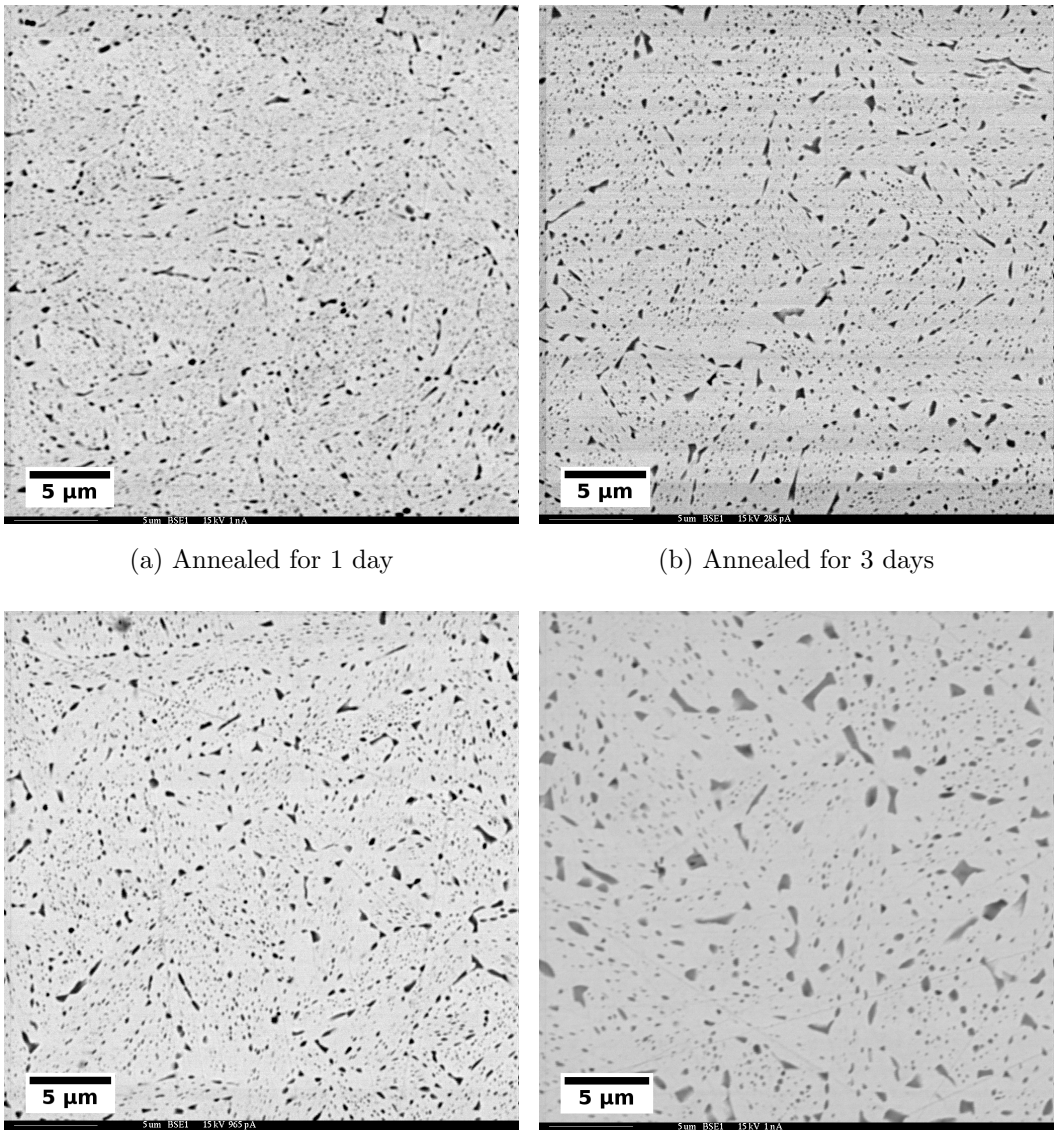

(a) Annealed for 1 day

(b) Annealed for 3 days

(c) Annealed for 7 days

(d) Annealed for 30 days

Fig. 4.12.: BSE images of U-2Zr alloy quenched from γ phase and annealed for various times at 600^{o}C

X-ray diffraction data could not confirm the presence of δ phase in 7 day and 30 day annealed samples and only peaks corresponding to α-U are seen (Figures 4.10 and 4.11). According to the U-Zr equilibrium phase diagram [119], the volume

fraction of δ phase in this alloy is $\sim$5% which is at the detection limit of XRD. BSE images of γ-quenched and annealed samples are shown in Figures 4.12a, 4.12b, 4.12c, and 4.12d. It is seen that the phase boundaries are quite diffuse during the initial stages of annealing and by the 30 day annealing time, the boundaries became sharp and the size of the precipitates also increased.

WDS analyses on the matrix and precipitates have been carried out and are shown in Table 4.2. It is seen that the Zr content in matrix matches with that in α-U phase. The second-phase precipitates (dark phase) were too small for the probe to obtain any compositional analysis. XRD data could not confirm the presence of δ phase in γ-quenched and annealed samples (Figures 4.13 and 4.14), similar to the as-cast and annealed samples.

Table 4.2: WDS analysis of annealed U-2Zr alloy samples

Alloy	Matrix		Precipitate	
	U (wt%)	Zr (wt%)	U (wt%)	Zr (wt%)
U-2Zr_AC1d[†]	99.62	0.38	-	-
U-2Zr_AC7d	99.45	0.55	-	-
U-2Zr_AC30d	99.88	0.12	-	-
U-2Zr_GQ1d[‡]	98.17	1.83	-	-
U-2Zr_GQ3d	99.61	0.39	-	-
U-2Zr_GQ7d	99.01	0.99	-	-
U-2Zr_GQ30d	99.87	0.13	-	-

[†]ACxd: As-cast alloy annealed for x=1, 7, 30 days

[‡]GQxd: γ-quenched alloy annealed for x=1, 3, 7, 30 days

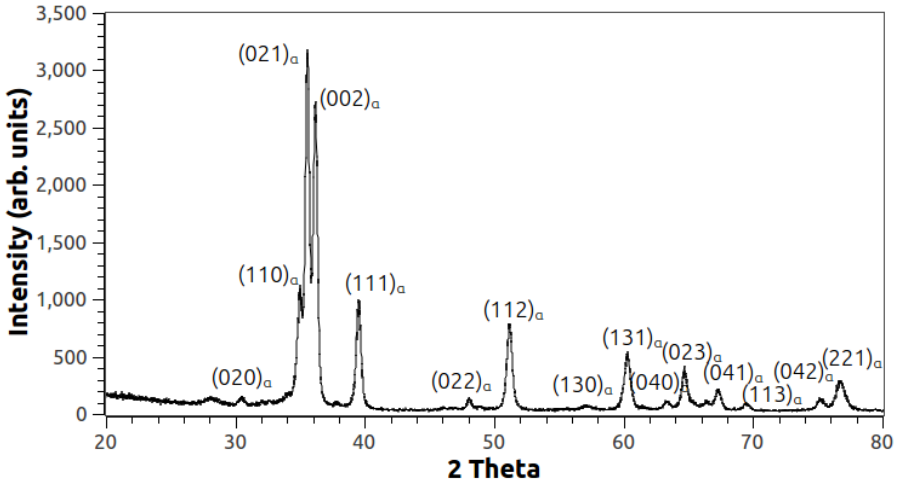

Fig. 4.13.: XRD pattern of U-2Zr alloy quenched from γ phase and annealed for 7 days

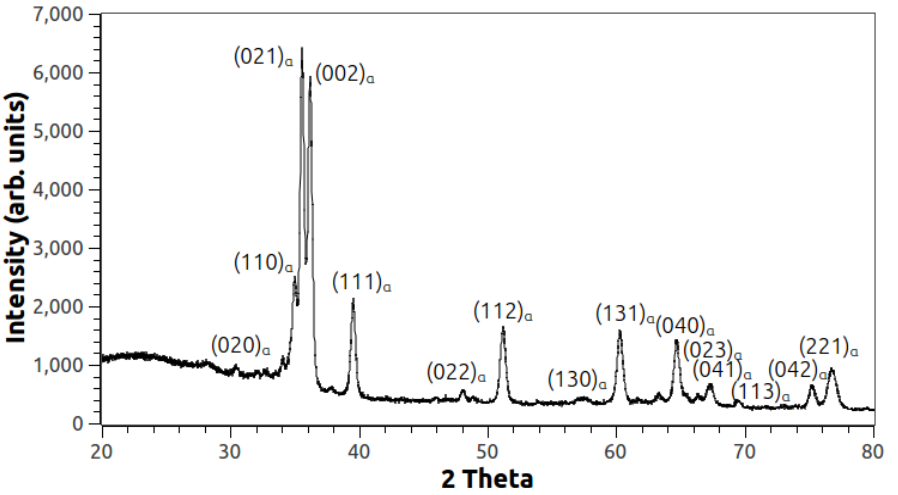

Fig. 4.14.: XRD pattern of U-2Zr alloy quenched from γ phase and annealed for 30 days

4.2 Metallurgy of U-5wt%Zr

4.2.1 As-cast and γ-Quenched Samples

Back scattered and optical images of the as-cast U-5Zr alloy are shown in Figures 4.15a and 4.15b. The Zr rich lamellae in the BSE image are very fine with no clear phase boundaries seen between the lamellae and the matrix. The optical image (Figure 4.15b) contains a fleck type microstructure with no lamellae resolved. The XRD pattern (Figure 4.16) contains only peaks for α-U even though two distinct phases are seen in the micrographs.

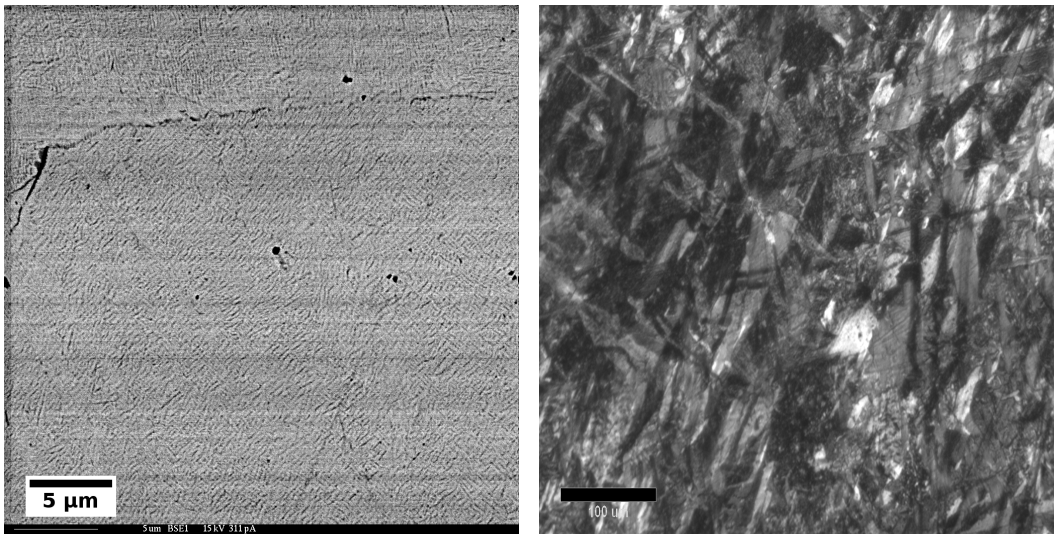

(a) BSE image (b) Optical (DIC) image

Fig. 4.15.: Back scattered and optical images of as-cast U-5Zr alloy

For the alloy quenched from γ phase, rapid cooling could not prevent Zr segregation and can be seen as bright and dark regions in Figure 4.17a. Prior γ grain boundaries are clearly evident in the optical micrograph (Figure 4.17b) clearly indicating that there was a direct $\gamma \rightarrow \alpha^{'}$ transformation. The morphology within the grains (i.e, $\alpha_a^{'}$ or $\alpha_b^{'}$) could not be observed. However, the TEM image (Figure 4.18a)

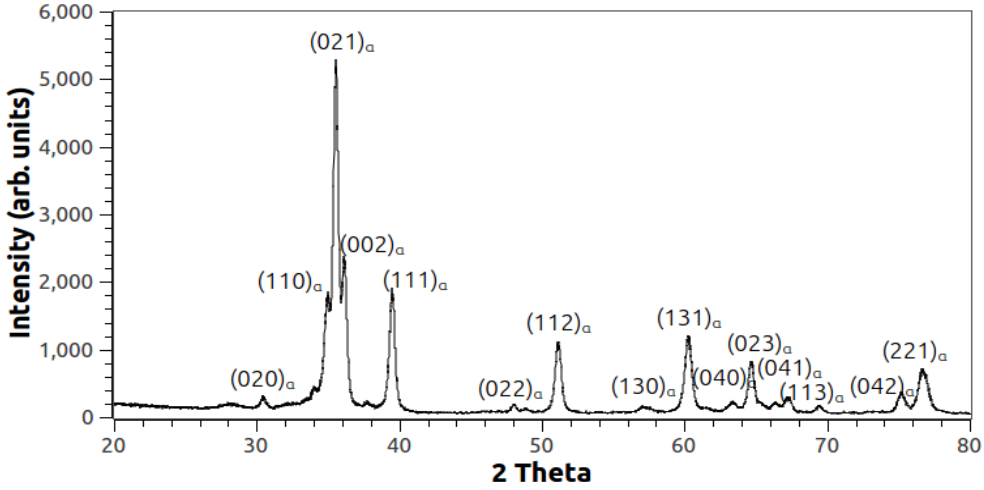

Fig. 4.16.: XRD pattern of as-cast U-5Zr alloy

clearly shows two phase microstructure in the form of bands rich in U (dark) and rich in Zr (bright). The γ phase has decomposed into alternate bands presumably of α-U and ω phase[2] when quenched. This form of ω formed when rapidly quenched is called athermal-ω and particles of ω are usually ellipsoidal in shape and aligned along $\langle 111 \rangle$direction of the parent b.c.c phase [125].

Plate like morphology of ω phase has also been observed in shock loaded Zr and it's alloys [96, 126]. Formation of ω phase from high temperature b.c.c phase is accomplished by alternate glide of $\{112\}_\gamma$ planes with a glide component of $\frac{\sqrt{3}}{12}a_\gamma$ in the $\langle 111 \rangle_\gamma$ direction contained in that plane [104]. The plate morphology represents a shear process and as mentioned in section 2.2.1, the $\gamma \rightarrow \alpha^{'}$ transformation is accomplished by a shear on $\{112\}_\gamma$ planes in a $\langle 111 \rangle_\gamma$ direction. So, both mechanisms (i.e, $\gamma \rightarrow \omega$, and $\gamma \rightarrow \alpha^{'}$) are similar to the extent that they occur on same planes

[2]As mentioned in Section 2.2.4, δ phase is purportedly formed after partial ordering of Zr atoms in ω phase. The ordering process requires diffusion of Zr atoms and is thermally activated. In the present study in all quenched alloys, since there is little or no time for diffusion, it is concluded that ω phase is formed instead of the δ phase. This will be elaborated in Chapter 5.

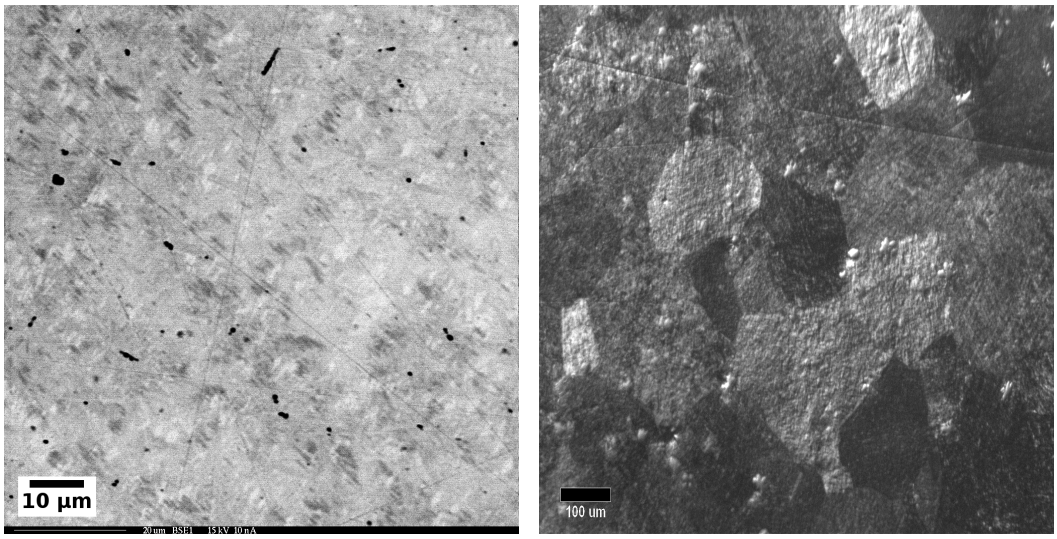

(a) BSE image (b) Optical (DIC)

Fig. 4.17.: Back scattered and optical images of γ-quenched U-5Zr alloy

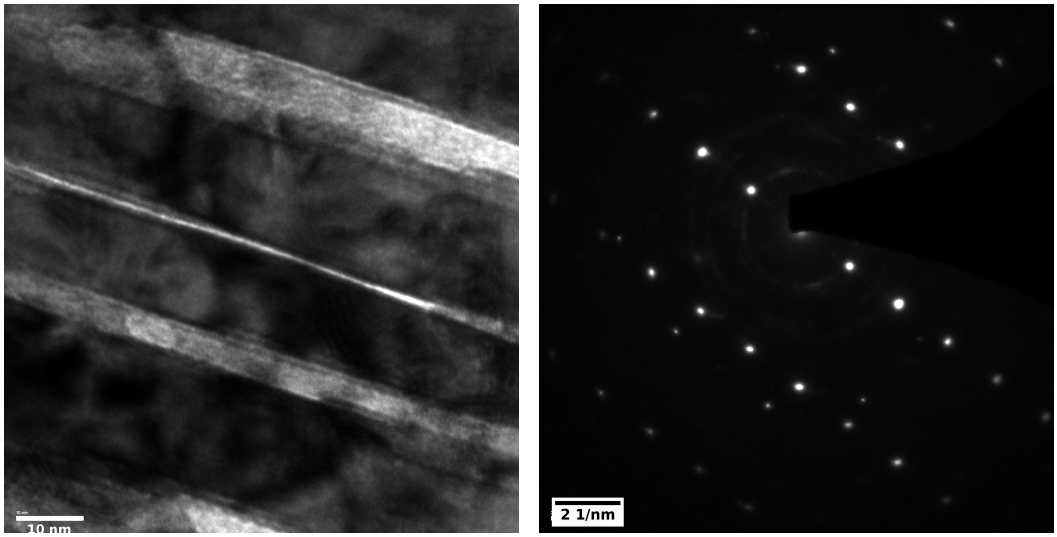

(a) Bright field image (b) SAD pattern

Fig. 4.18.: TEM images of γ-quenched U-5Zr alloy

but the sense of atomic movements is opposite and this could explain the plate morphology of ω in U-Zr alloys. The selected area diffraction (SAD) pattern corresponding to the bright field image is shown in Figure 4.18b. Since the data was acquired using a single tilt holder, the zone axis could not be aligned to a low index *hkl* plane. Indexing turned out to be very difficult and it was not pursued any further. The XRD pattern shown in Figure 4.19 contains peaks for α-U and no appreciable contraction in the b lattice parameter could be observed during Rietveld refinement. Phase transformation temperatures in quenched and as-cast alloys are shown in Figure 4.20. In the case of quenched alloy, only two transformations are seen at 601^{o}C and 700^{o}C during heating. In the case of as-cast alloy, four transformations are seen, consistent with the U-Zr phase diagram. Pertinent phases involved in these transformations will be discussed in Chapter 5.

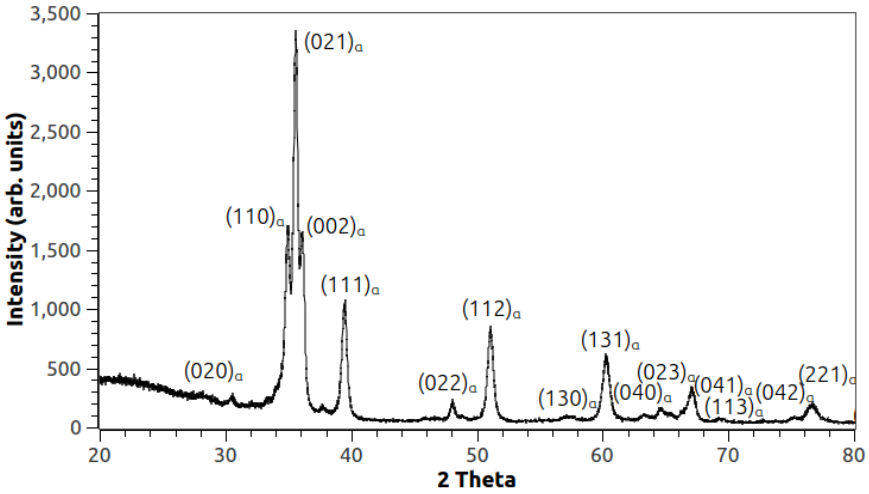

Fig. 4.19.: XRD pattern of γ-quenched U-5Zr alloy

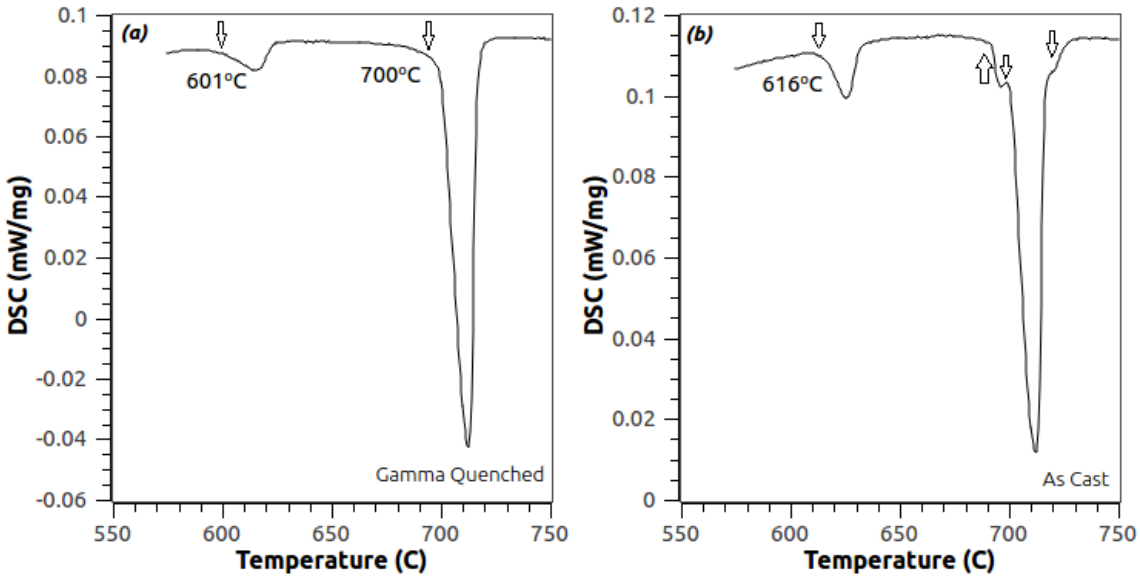

Fig. 4.20.: DSC curves of quenched and as-cast U-5Zr alloy showing various transformations (indicated by arrows)

4.2.2 Samples Step-Cooled from the γ Phase

Figure 4.21a is the BSE image of the alloy step-cooled from γ phase and held in $(\alpha + \delta)$ phase field for 3 days and cooled. Zr-rich precipitates are seen in a matrix composed of α-U. Figure 4.21b is a BSE image of the alloys quenched from $(\alpha + \gamma)$ phase field after homogenizing at 650^{o}C for 2 days. Similar morphology is seen but the number of precipitates is much higher. The XRD pattern for the step-cooled alloy ($\gamma \xrightarrow[650C]{(\alpha+\gamma)}$ 2 days $\xrightarrow[600C]{(\alpha+\delta)}$ 3 days) consisted of peaks for α-U with very faint and a broad peak at $\sim 72^o$ for δ phase (Figure 4.22). Since almost all peaks for γ phase coincide with those of α-U, it is difficult to ascertain it's presence from XRD data (Figure 4.23) of the step-cooled alloy quenched from 650^{o}C ($\gamma \xrightarrow[650C]{(\alpha+\gamma)}$ 2 days and quenched). WDS analysis on the precipitate and the matrix shown in Table 4.3 indicate that they are δ phase and α-U, and γ phase and α-U respectively.

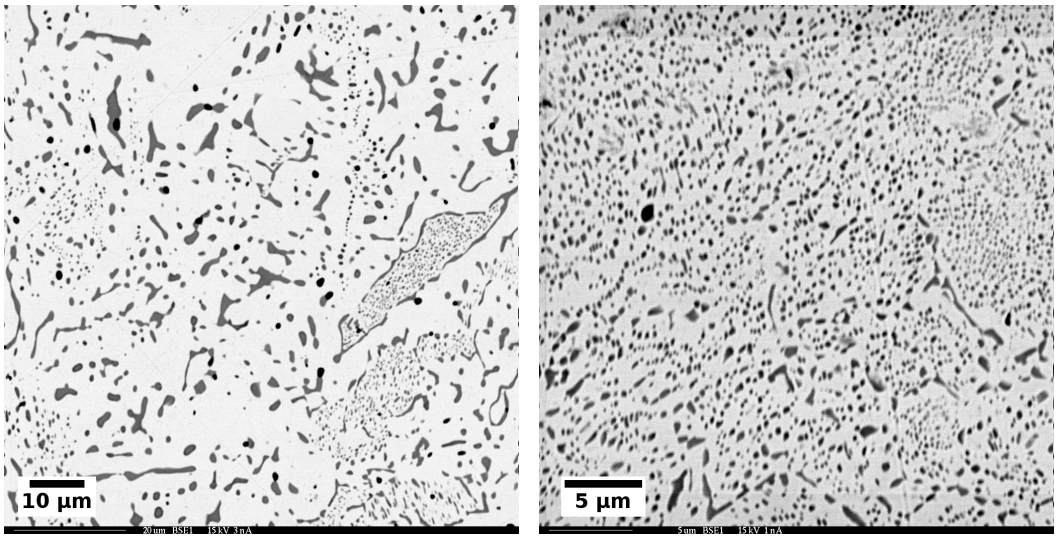

(a) $\gamma \xrightarrow[650C]{(\alpha+\gamma)}$ 2 days $\xrightarrow[600C]{(\alpha+\delta)}$ 3 days

(b) $\gamma \xrightarrow[650C]{(\alpha+\gamma)}$ 2 days and quenched

Fig. 4.21.: Back scattered images of step-cooled U-5Zr alloys

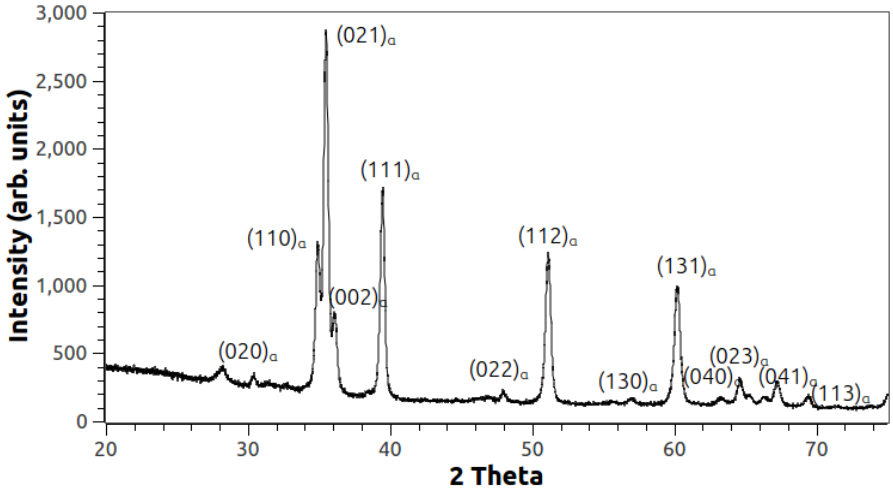

Fig. 4.22.: XRD pattern of U-5Zr alloy step-cooled from $\gamma \xrightarrow[650C]{(\alpha+\gamma)}$ 2 days $\xrightarrow[600C]{(\alpha+\delta)}$ 3 days

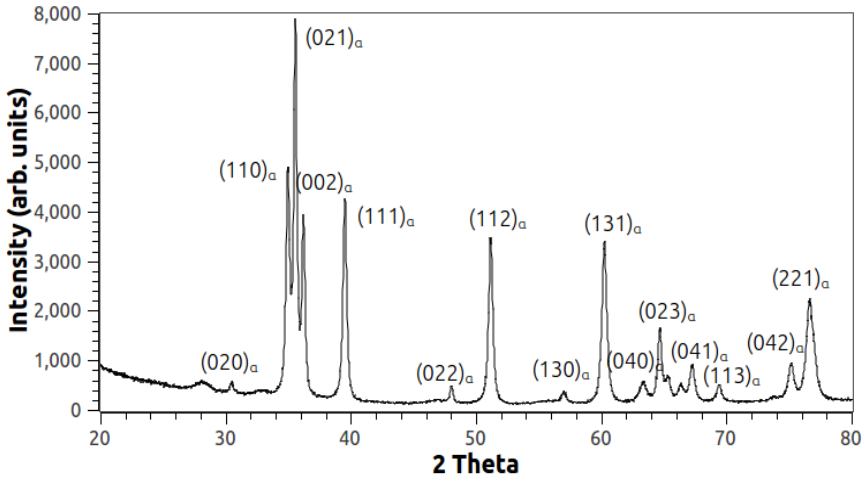

Fig. 4.23.: XRD pattern of U-5Zr alloy step-cooled from $\gamma \xrightarrow[650C]{(\alpha+\gamma)}$ 2 days and quenched

Table 4.3: WDS analysis of step-cooled U-5Zr alloy

Alloy	Matrix		Precipitate	
	U (wt%)	Zr (wt%)	U (wt%)	Zr (wt%)
U-5Zr†	99.70	0.30	56.01	43.99
U-5Zr‡	99.38	0.62	62.28	37.72

†Step-cooled from $\gamma \xrightarrow[650C]{(\alpha+\gamma)}$ 2 days $\xrightarrow[600C]{(\alpha+\delta)}$ 3 days

‡Step-cooled from $\gamma \xrightarrow[650C]{(\alpha+\gamma)}$ 2 days and quenched

4.2.3 Samples Annealed at 600^{o}C

As-cast alloy samples and γ-quenched samples were annealed at 600^{o}C, in the $(\alpha+\delta)$ phase field for 1, 3, 7, and 30 days. BSE images for as-cast annealed samples are shown in Figures 4.24a, 4.24b, 4.24c, 4.24d respectively.

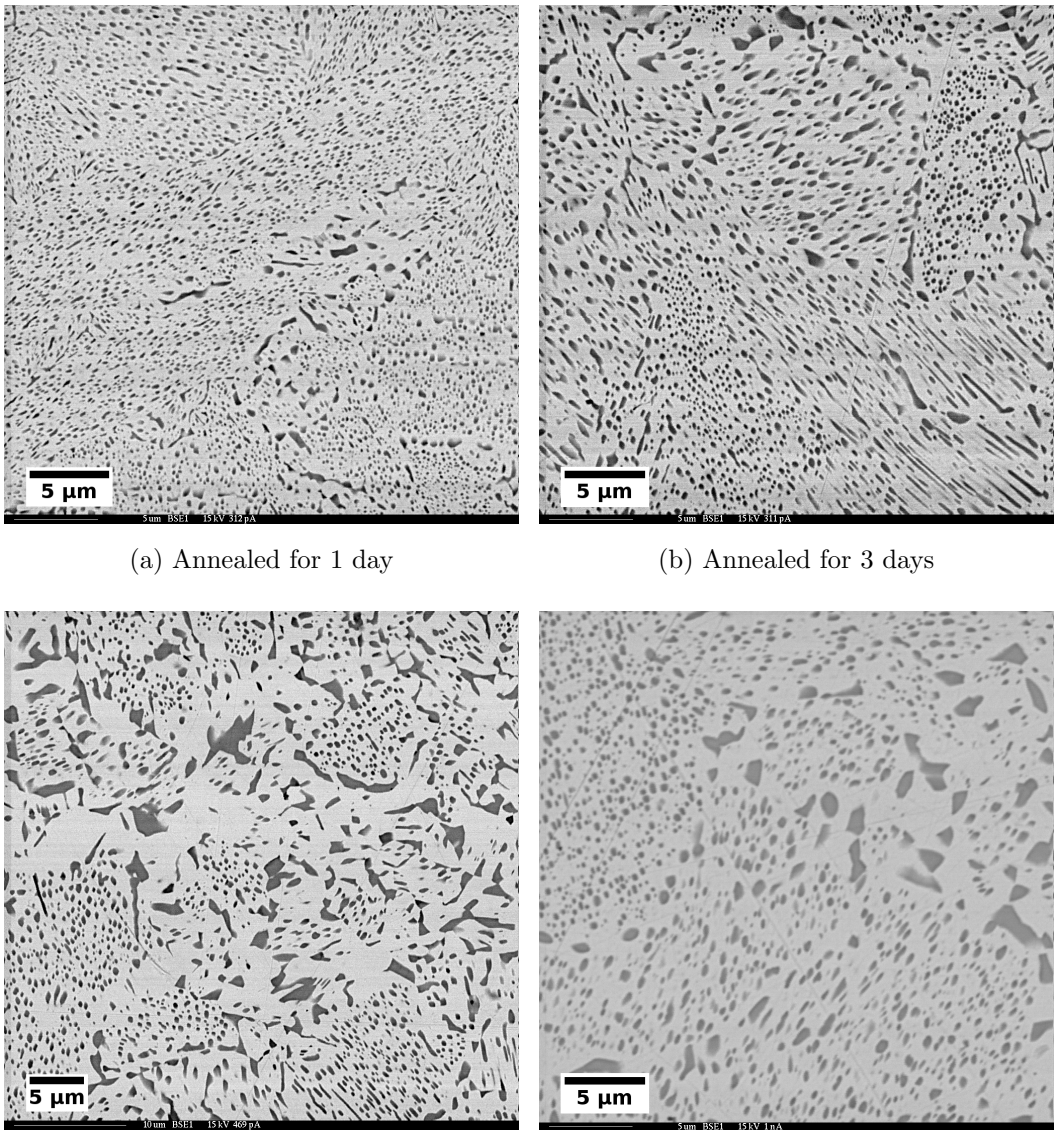

(a) Annealed for 1 day

(b) Annealed for 3 days

(c) Annealed for 7 days

(d) Annealed for 30 days

Fig. 4.24.: Back scattered images of as-cast U-5Zr alloy annealed for various times at 600^{o}C

It is seen that the precipitates grow as a function of annealing time. WDS analysis on the matrix and precipitate phase revealed that they correspond to α-U and δ phase respectively (Table 4.4). However XRD patterns in the case of 7 and 30 day

Table 4.4: WDS analysis of annealed U-5Zr alloy samples

Alloy	Matrix		Precipitate	
	U (wt%)	Zr (wt%)	U (wt%)	Zr (wt%)
U-5Zr_AC1d[†]	98.04	1.96	-	-
U-5Zr_AC3d	99.51	0.49	65.03	34.97
U-5Zr_AC7d	99.80	0.20	57.69	42.31
U-5Zr_AC30d	-	-	59.94	40.06
U-5Zr_GQ1d[‡]	99.26	0.74	-	-
U-5Zr_GQ3d	99.49	0.51	-	-
U-5Zr_GQ7d	99.44	0.56	67.08	32.92
U-5Zr_GQ30d	99.70	0.30	57.01	42.99

[†]ACxd: As-cast alloy annealed for x=1, 3, 7, 30 days

[‡]GQxd: γ-quenched alloy annealed for x=1, 3, 7, 30 days

annealed samples did not have any peaks associated with δ phase (Figures 4.25 and 4.26). The volume fraction of δ phase in α-U matrix according to phase diagram is $\sim$12%. This should be detectable by XRD and possible reasons are discussed in Chapter 5. BSE images for the γ-quenched samples annealed for 1, 3, 7, and 30 days are shown in Figures 4.27a, 4.27b, 4.27c, 4.27d respectively. In the case of the 1 day annealed sample (Figure 4.27a), the phase boundaries between matrix and the precipitates are diffuse, as in spinodal decomposition. However, the time scale here is too long to be associated with a spinodal decomposition. The phase boundaries became sharp by the end of 30 day annealing period. Appearance of diffuse phase boundaries could also be due to a Zr gradient present in the samples due to the ongoing diffusion process. XRD patterns for 7 day and 30 day annealed samples shown in Figures 4.28 and 4.29 do not contain any peaks for δ phase though the Zr content in the precipitates is consistent with the δ phase composition.

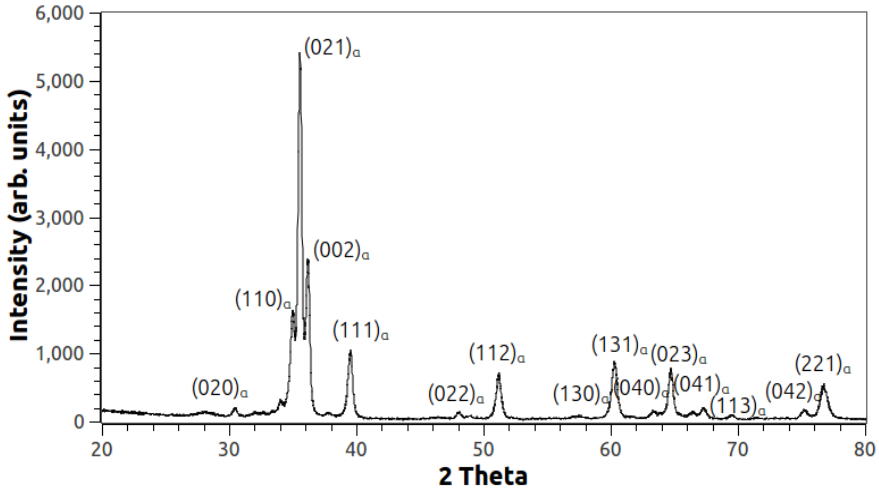

Fig. 4.25.: XRD pattern of as-cast U-5Zr alloy annealed for 7 days

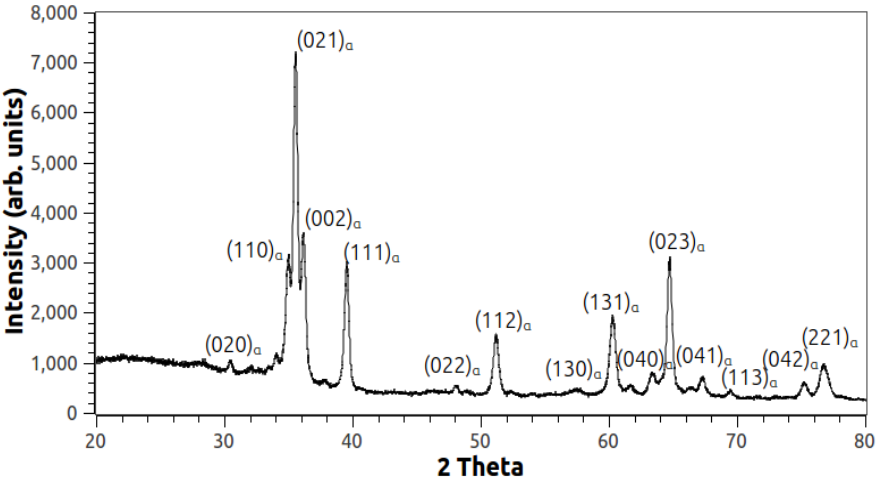

Fig. 4.26.: XRD pattern of as-cast U-5Zr alloy annealed for 30 days

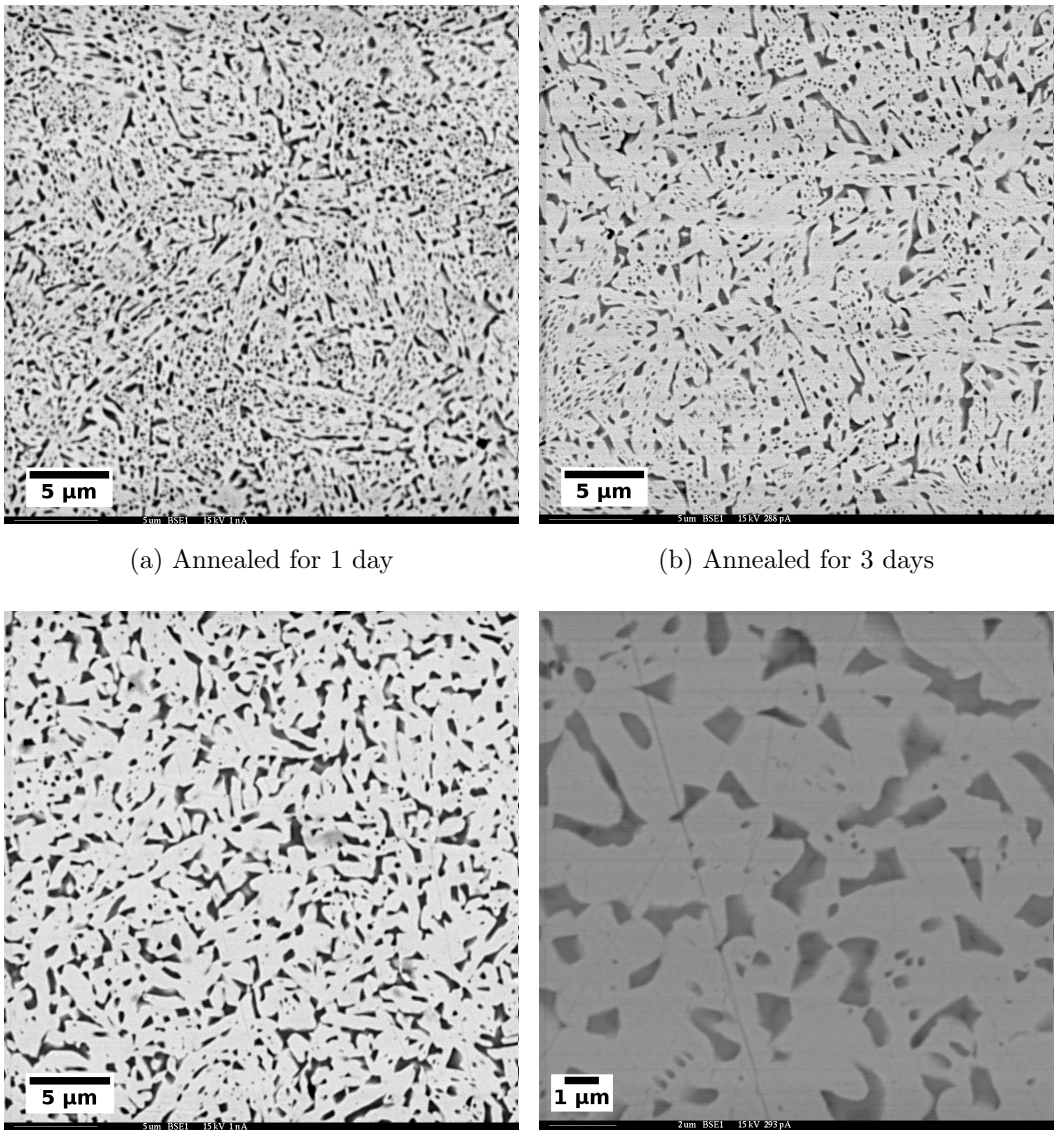

(a) Annealed for 1 day

(b) Annealed for 3 days

(c) Annealed for 7 days

(d) Annealed for 30 days

Fig. 4.27.: BSE images of U-5Zr alloy quenched from γ phase and annealed for various times at 600^{o}C

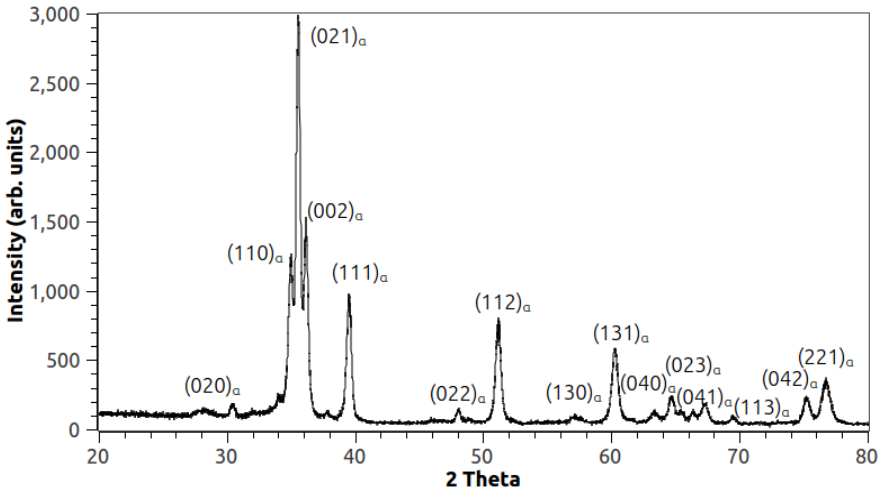

Fig. 4.28.: XRD pattern of U-5Zr alloy quenched from γ phase and annealed for 7 days

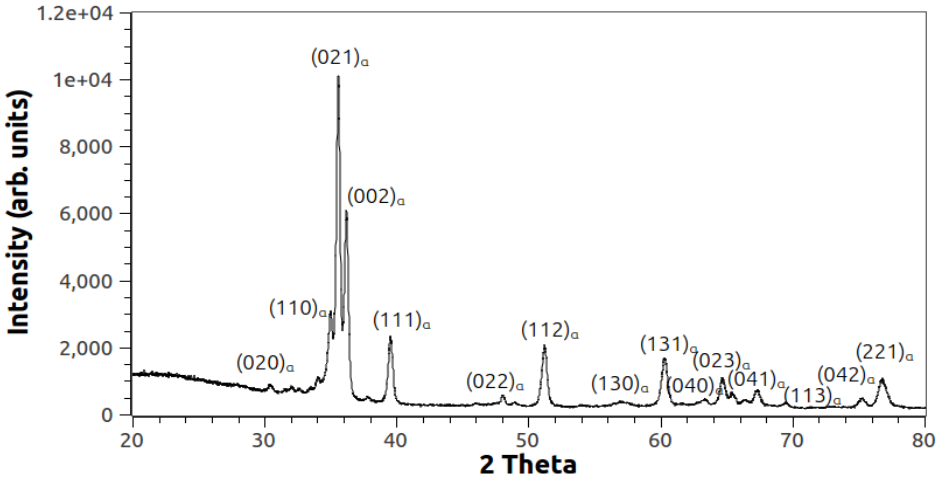

Fig. 4.29.: XRD pattern of U-5Zr alloy quenched from γ phase and annealed for 30 days

4.3 Metallurgy of U-10wt%Zr

4.3.1 As-cast and γ-Quenched Samples

Microstructures of as-cast U-10Zr alloy are shown in Figure 4.30. In the back scattered image (Figure 4.30a), a lamellar microstructure is seen with Zr-rich (dark) and Zr-lean (bright) phases spaced less than ~ 0.5 μm. No compositional analysis could be performed on the individial phases because of spatial resolution of the features. In the optical mode, as seen in Figure 4.30b, bright and dark regions are likely to have different Zr contents and the variation is clearly brought out by etching. At higher magnification (Figure 4.31), substructure within each region is clearly seen as fine lamellae. No remnant γ grain boundaries could be seen and the irregular grain features indicate a sequential $\gamma \rightarrow \beta \rightarrow \alpha$ double transformation. The XRD pattern of the as-cast alloy, though containing a two phase microstructure, only showed peaks corresponding to α-U (Figure 4.32) .

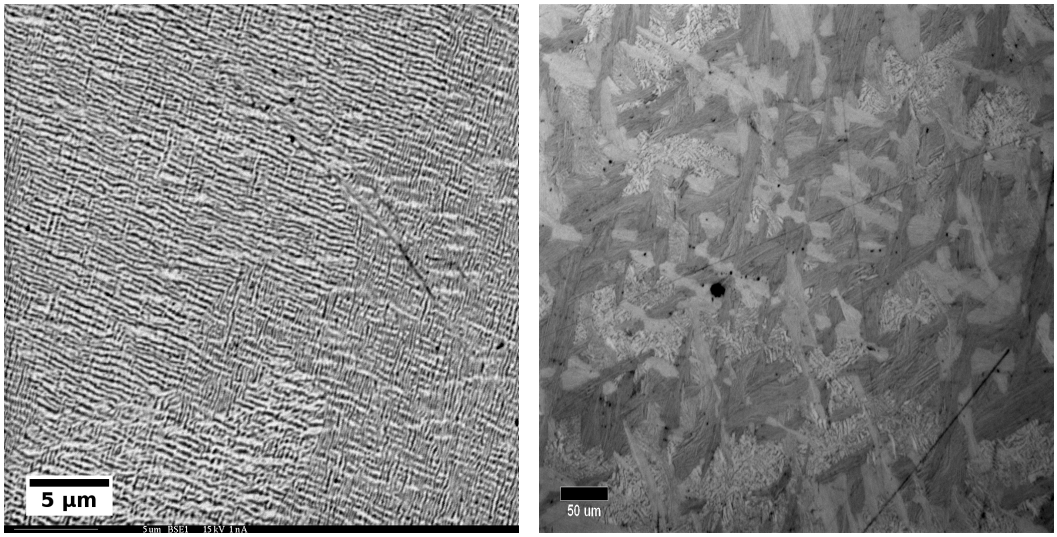

(a) BSE image (b) Optical (DIC) image

Fig. 4.30.: Back scattered and optical images of as-cast U-10Zr alloy

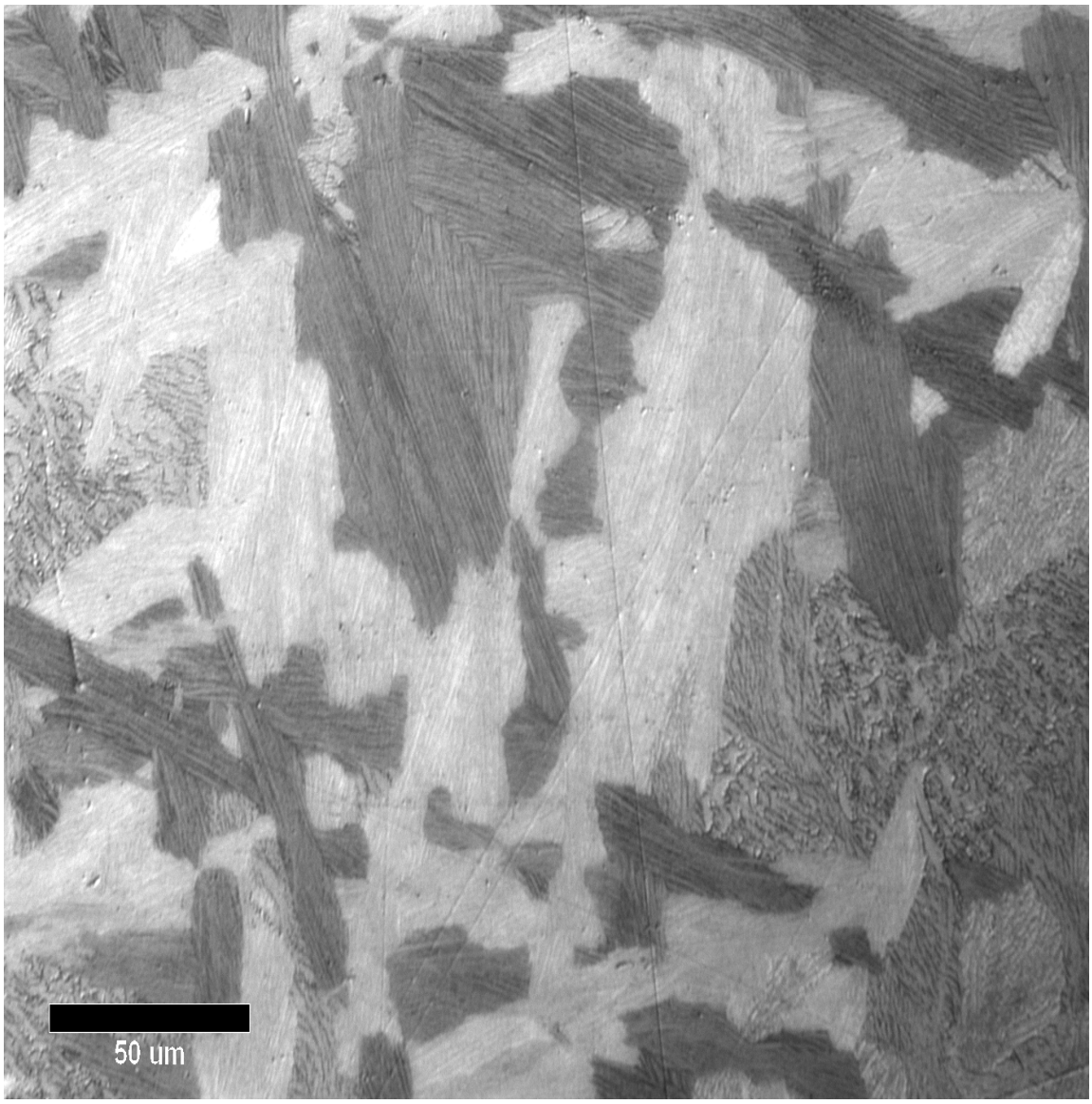

Fig. 4.31.: Optical image of as-cast U-10Zr at higher magnification showing lamellae within each grain

Back scattered and optical images of γ-quenched U-10Zr alloy are shown in Figures 4.33a and 4.33b. In contrast to the slow cooled as-cast alloy, the BSE image shows little but visible segregation of Zr, seen as bright regions in Figure 4.33a. In

the optical micrograph, remnant gamma grain boundaries are clearly seen which indicates a direct $\gamma \rightarrow \alpha^{'}$ transformation, similar to γ-quenched U-5Zr alloy.

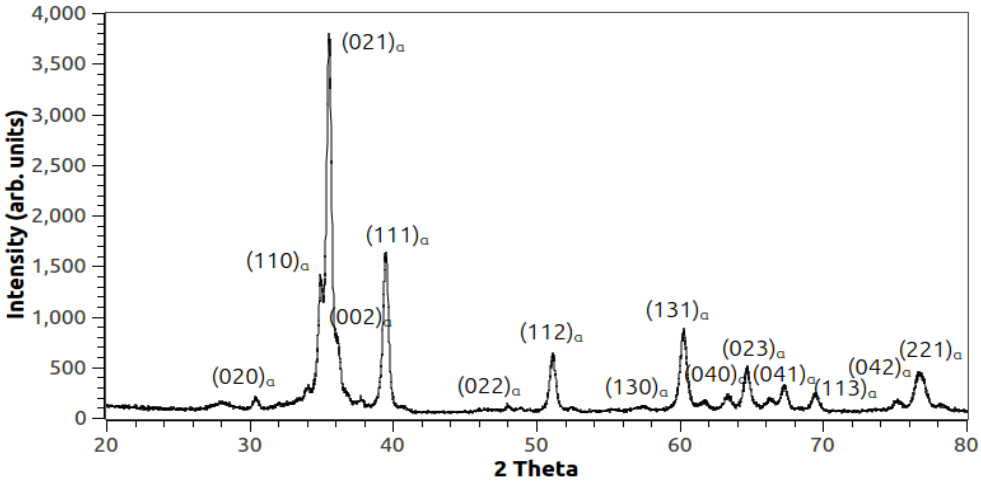

Fig. 4.32.: XRD pattern of as-cast U-10Zr alloy

In the TEM bright field image (Figure 4.34a) a two phase microstructure is seen as bright bands presumably of ω phase[3] in dark matrix consisting of α-U. This image is quite similar to the Bright field TEM image of γ-quenched U-5Zr alloy (Figure 4.18a. SAD pattern obtained from the same region is shown in Figure 4.34b. Since these bright features are less than 10 nm in size, diffraction spots corresponding to ω phase are not seen. If the diffraction pattern is obtained using a single tilt holder, the tilting freedom is restricted to only one axis. Using such a holder, recording a diffraction pattern which would give complete crystallographic information on the phases present (i.e, in the bright field TEM image; Figure 4.34a) manifests itself as a challenging task.

[3]As mentioned in the previous Section, when quenched from γ phase, the microstructure observed is the product of diffusionless transformation and the phases formed are ω and $\alpha^{'}$. This aspect is further elaborated in Chapter 5.

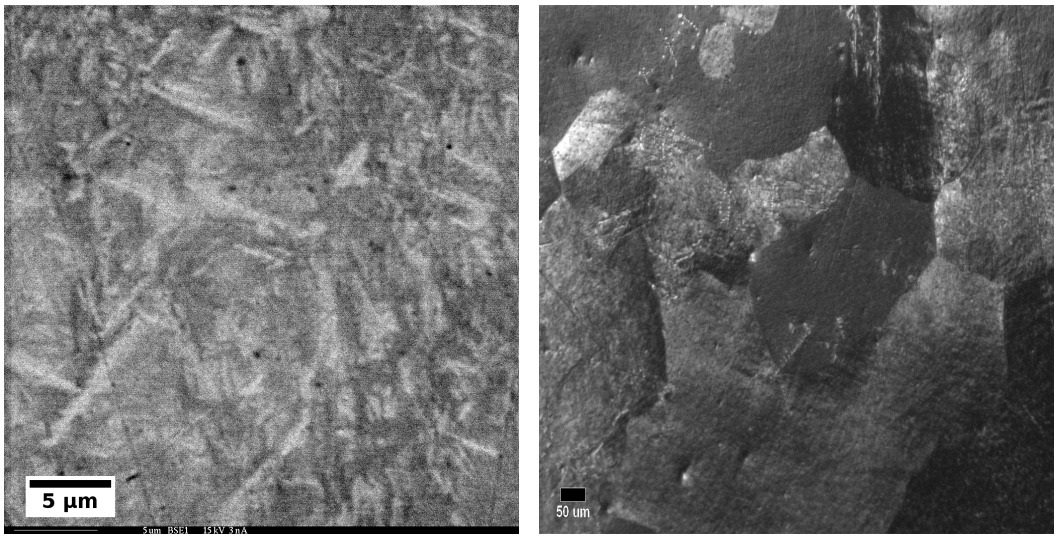

(a) BSE image (b) Optical (DIC)

Fig. 4.33.: BSE and optical images of γ-quenched U-10Zr alloy

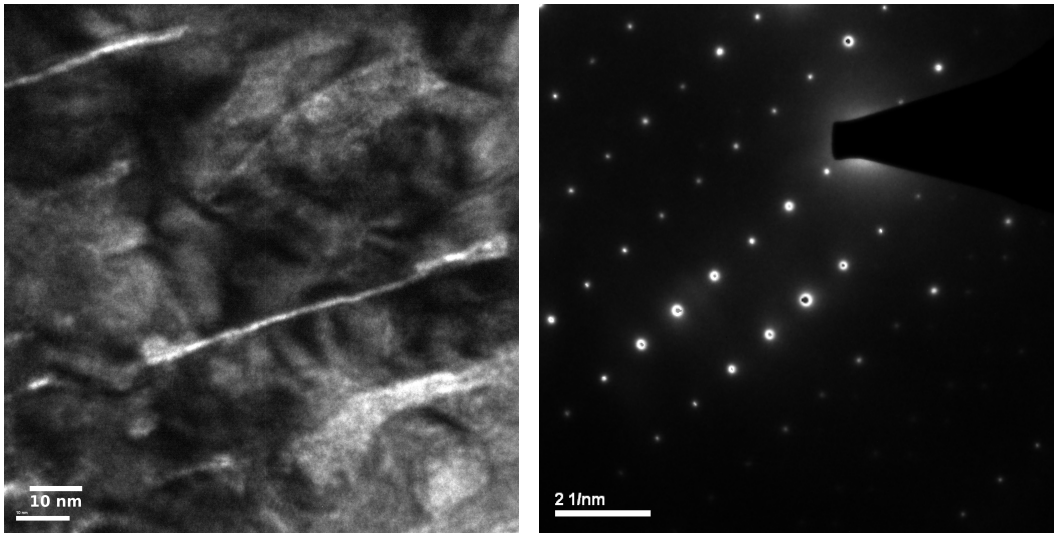

(a) Bright field image (b) SAD pattern

Fig. 4.34.: TEM images of γ-quenched U-10Zr alloy

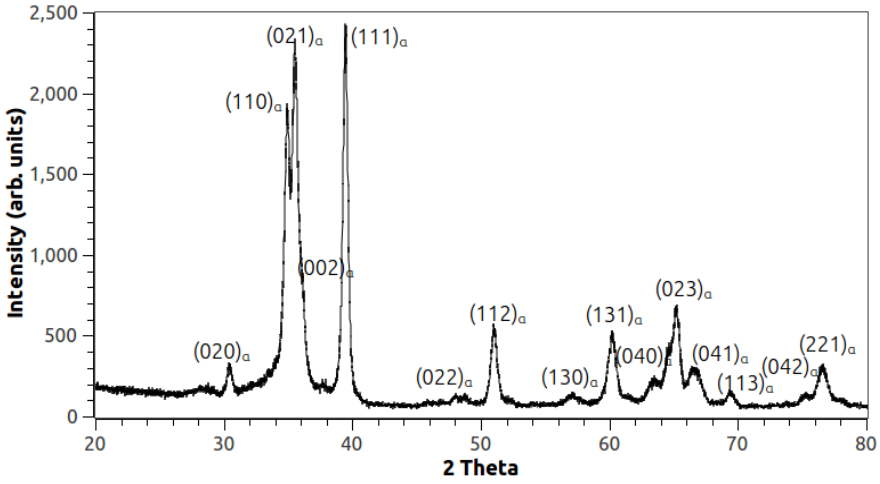

Fig. 4.35.: XRD pattern of γ-quenched U-10Zr alloy

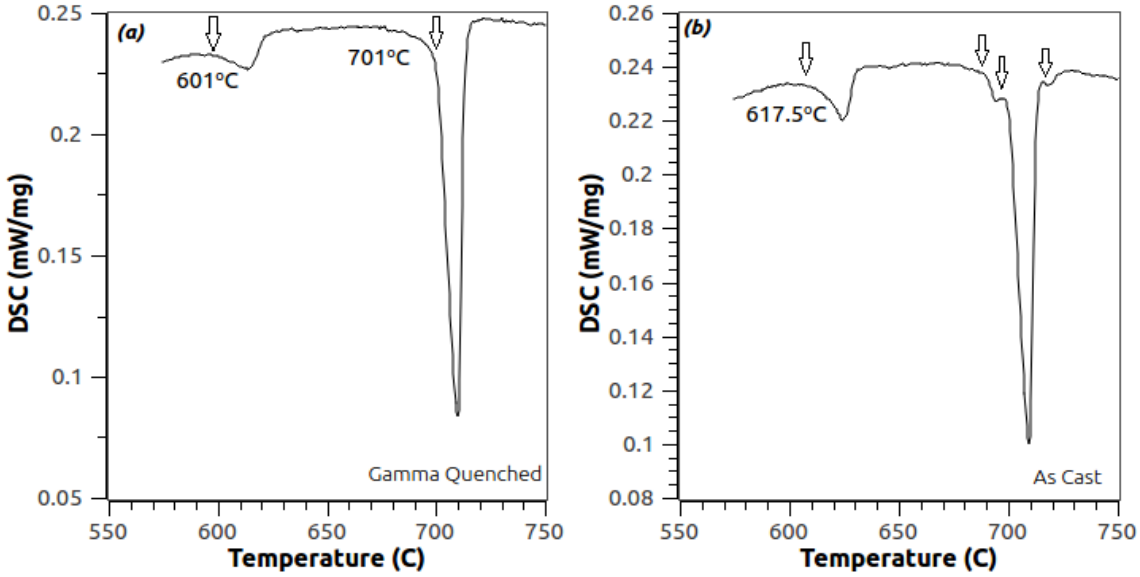

Fig. 4.36.: DSC curves of U-10Zr alloy showing various transformations (indicated by arrows)

XRD pattern of the γ-quenched alloy is shown in figure 4.35. There were no peaks associated with ω phase and all the peaks were indexed for α-U. Since the features of ω phase are of the order of few nanometers (Figures 4.18a and 4.34a), it is below the detection limit of XRD and only peaks for α-U are seen. It is also seen that there is visible overlapping of $(021)_\alpha$ and $(002)_\alpha$ lines. DSC curves of γ-quenched and as-cast alloy are shown in Figure 4.36. Only two transformations, one at 601^oC and another at 701^oC are seen in quenched alloy while the curve for as-cast alloy consists of four transformations. It is also seen that the transformation at 617.5^oC in as-cast alloy shifted to a lower temperature in the case of quenched alloy and occurs at 601^oC.

4.3.2 Samples Step-Cooled from the γ Phase

Back scattered image of the sample step-cooled from γ and annealed at 600^oC (i.e, $\gamma \xrightarrow[650C]{(\alpha+\gamma)}$ 2 days $\xrightarrow[600C]{(\alpha+\delta)}$ 3 days) is shown in Figure 4.37a. A two phase microstructure is seen with α-U matrix and Zr-rich precipitates. Microstructure of the alloy quenched from 650^oC (i.e, $\gamma \xrightarrow[650C]{(\alpha+\gamma)}$ 2 days and quenched) is shown in back scattered mode in Figure 4.37b. This thermal profile was chosen to retain $(\alpha + \gamma)$ microstructure at ambient temperature. In this Figure, the γ phase lamellae are observed in α-U matrix. WDS analysis for both thermal profiles are shown in Table 4.5. The compositions are consistent with α-U and δ phase, and α-U respectively.

Table 4.5: WDS analysis of step-cooled U-10Zr alloy

Alloy	Matrix		Precipitate	
	U (wt%)	Zr (wt%)	U (wt%)	Zr (wt%)
U-10Zr†	99.65	0.35	56.11	43.89
U-10Zr‡	98.28	1.72	-	-

†Step-cooled from $\gamma \xrightarrow[650C]{(\alpha+\gamma)}$ 2 days $\xrightarrow[600C]{(\alpha+\delta)}$ 3 days

‡Step-cooled from $\gamma \xrightarrow[650C]{(\alpha+\gamma)}$ 2 days and quenched

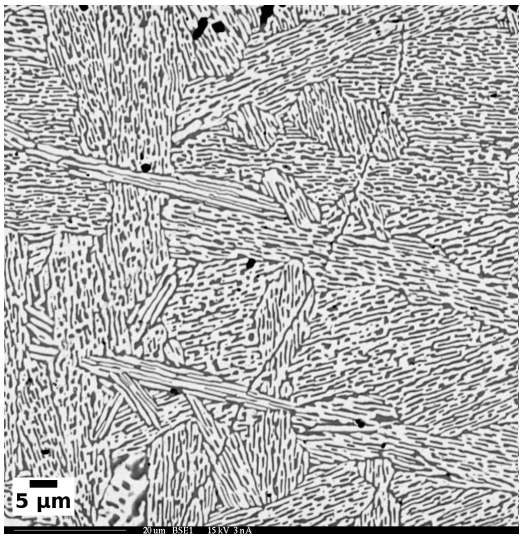

(a) $\gamma \xrightarrow[650C]{(\alpha+\gamma)}$ 2 days $\xrightarrow[600C]{(\alpha+\delta)}$ 3 days

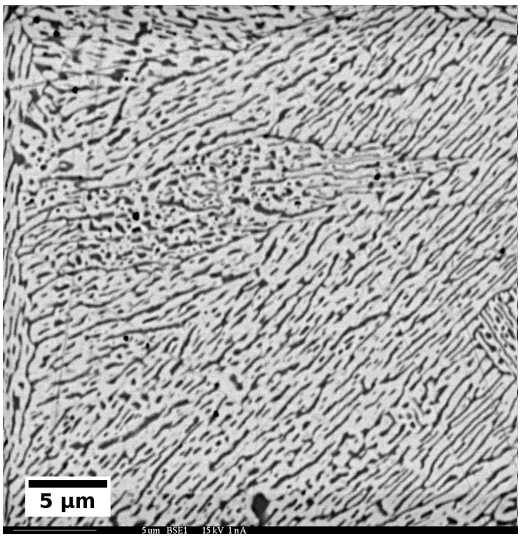

(b) $\gamma \xrightarrow[650C]{(\alpha+\gamma)}$ 2 days and quenched

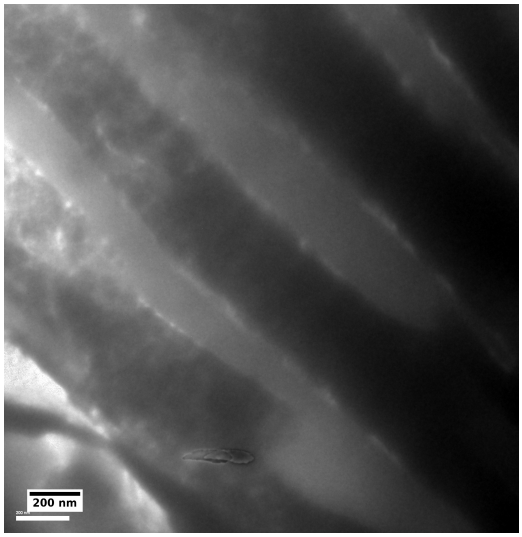

(c) Bright field TEM image showing γ lamellae

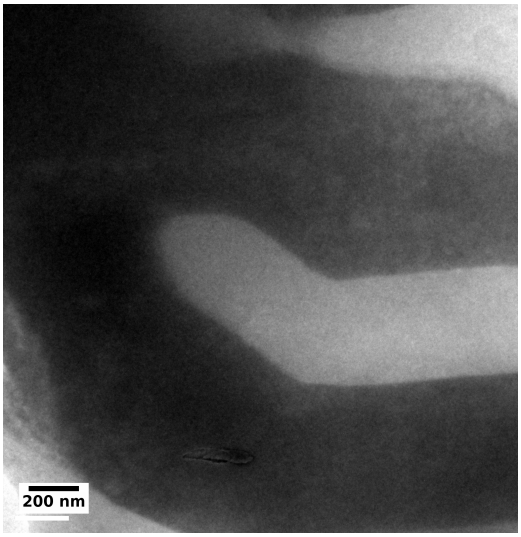

(d) Bright field TEM imaging showing γ lamellae at higher magnification

Fig. 4.37.: Back scattered and Bright field TEM images of step-cooled U-10Zr alloys

Bright field TEM images of the step-cooled sample (i.e, $\gamma \xrightarrow[650C]{(\alpha+\gamma)}$ 2 days and quenched) are shown in Figures 4.37c, 4.37d, and 4.38. The interconnected lamellae of γ phase are imaged at higher magnification (Figures 4.37c and 4.37d) and appear

as bright features. Dark feature in the image corresponds to α-U. Lattice fringes of α-U matrix are evident in Figure 4.38, which was taken at very high magnification (300 kx).

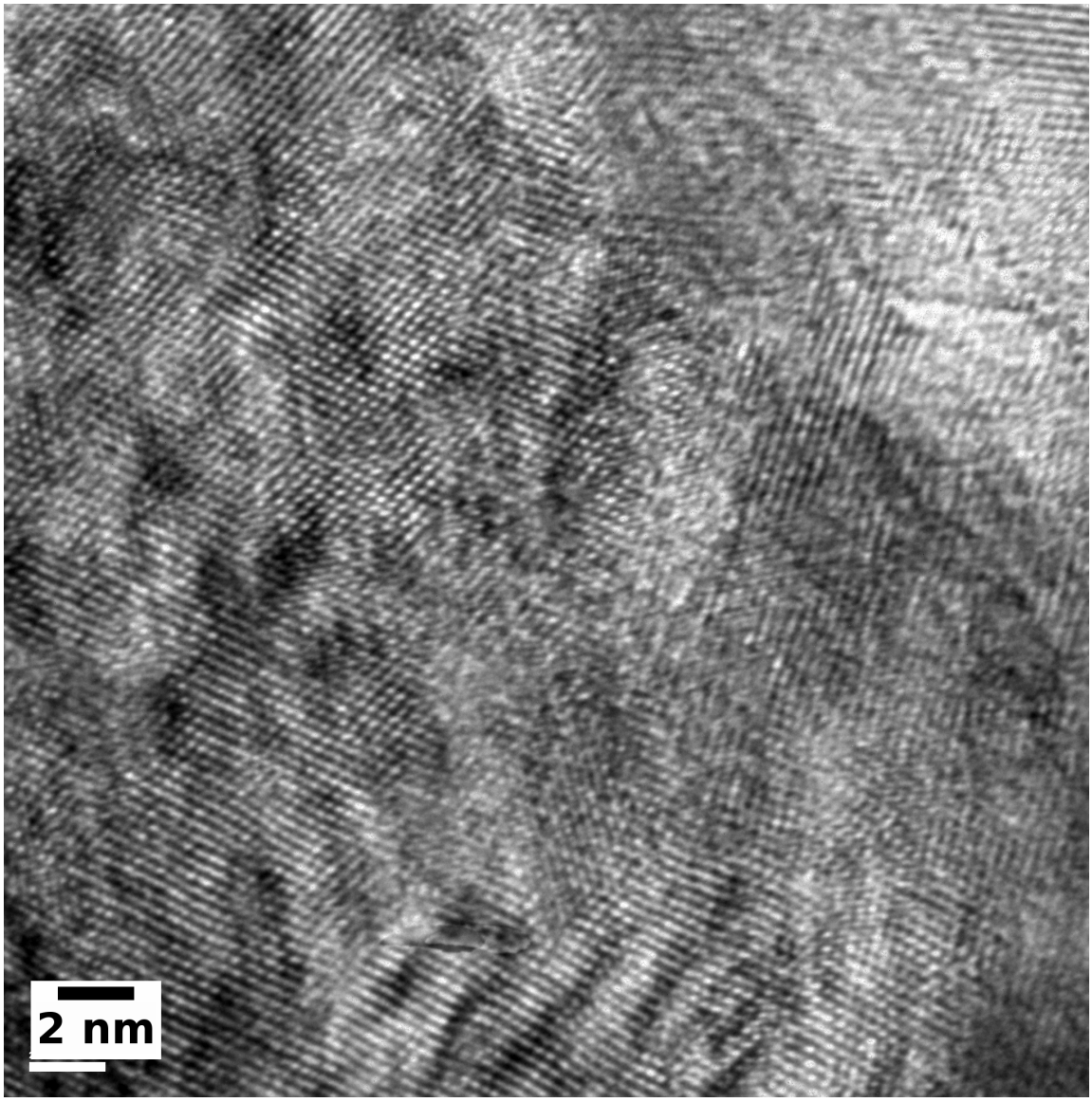

Fig. 4.38.: Bright field TEM image of U-10Zr alloy step-cooled from $\gamma \xrightarrow[650C]{(\alpha+\gamma)}$ 2 days and quenched showing lattice fringes

XRD patterns of the step-cooled samples are shown in Figures 4.39 and 4.40. For the alloy step-cooled and annealed at 600^{o}C (i.e, $\gamma \xrightarrow[650C]{(\alpha+\gamma)}$ 2 days $\xrightarrow[600C]{(\alpha+\delta)}$ 3 days), δ phase peaks are clearly seen (indexed in red color in Figure 4.39) while for the alloy annealed at 650^{o}C, (i.e, $\gamma \xrightarrow[650C]{(\alpha+\gamma)}$ 2 days and quenched), the pattern consisted of peaks for α-U. Presence of γ phase could not be detected as most of γ-U peaks overlap with α-U peaks. The broad δ phase peaks seen for the step-annealed sample clearly shows that the collapse of $\{111\}_\gamma$ planes is not complete[4]. Broad peaks in XRD can be explained if it lacks long range order and indicates that equilibrium has not been reached.

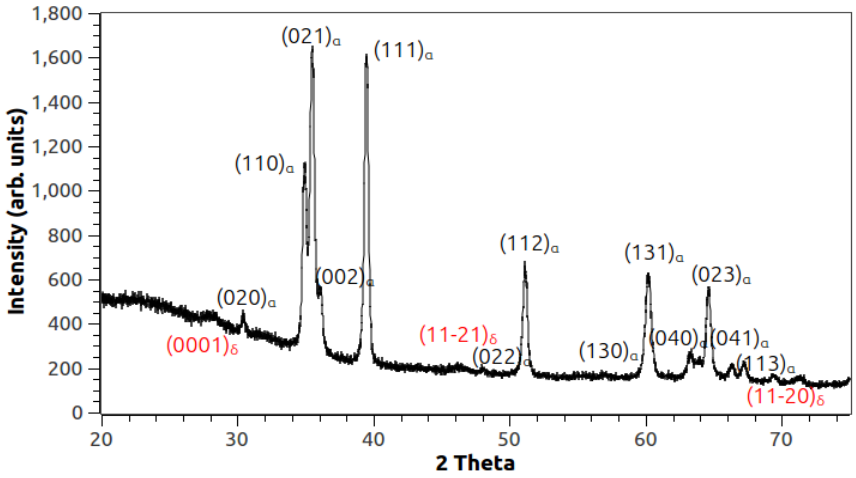

Fig. 4.39.: XRD pattern of U-10Zr alloy step-cooled from $\gamma \xrightarrow[650C]{(\alpha+\gamma)}$ 2 days $\xrightarrow[600C]{(\alpha+\delta)}$ 3 days

[4]It is worth noting here that as per literature [62], ω phase orders to δ phase once it has the required amount of Zr (i.e, atleast 40.7wt% [110]) in it. Regardless of the phase present (ω or δ), they are identified at the same 2θ positions in XRD data. It is more a matter of how the phase is formed (shear or diffusional means) and as discussed later, it might be more appropriate to call them ω_{ath} (shear) and ω_d (diffusional) instead of ω and δ. These aspects are elaborated in detail in Chapter 5.

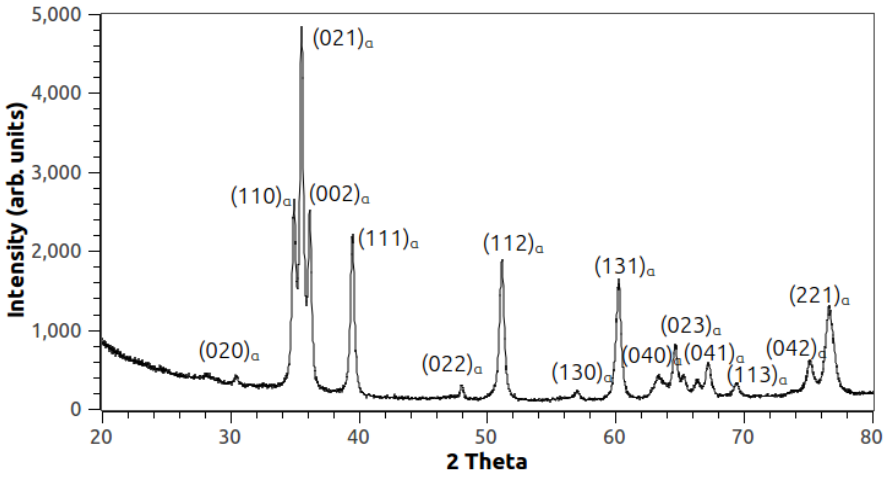

Fig. 4.40.: XRD pattern of U-10Zr alloy step cooled from $\gamma \xrightarrow[650C]{(\alpha+\gamma)}$ 2 days and quenched

4.3.3 Samples Annealed at 600^{o}C

Back scattered images of the as-cast U-10Zr alloy samples annealed at 600^{o}C for 1, 3, 7, and 30 days are shown in Figures 4.41a, 4.41b, 4.41c, and 4.41d. The lamellar microstructure in the as-cast alloy (Refer to Figure 4.30a) coarsened into precipitates rich in Zr. The size of the precipitates did not change after 7 days of annealing except for interconnection between them as seen in the 30 day annealed sample (Figure 4.41d). WDS analysis results are shown in Table 4.6 which indicate that the matrix is α-U and the precipitates have a composition consistent with the δ phase. An increase in the amount of zirconium in the δ phase is seen from 3 to 30 day anneal (41.74 to 45.94 wt%) indicating that Zr is rejected from the α-U matrix diffusing into the δ phase. It is poited out that at 600^{o}C, the Zr content in the δ phase was reported to range between 40.7 to 57.8 wt% [110].

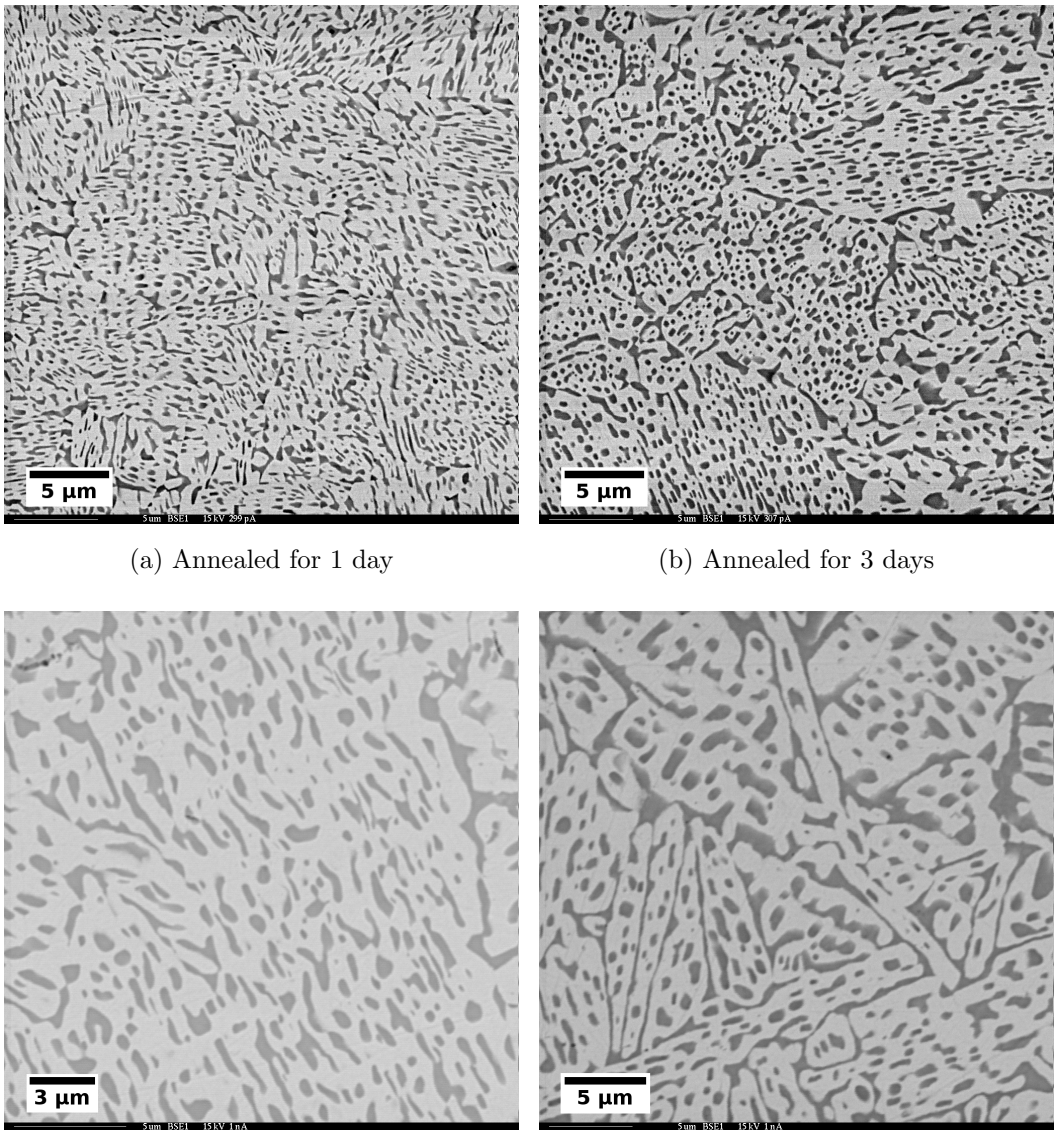

(a) Annealed for 1 day

(b) Annealed for 3 days

(c) Annealed for 7 days

(d) Annealed for 30 days

Fig. 4.41.: Back scattered images of as-cast U-10Zr alloy annealed for various times at 600^{o}C

Table 4.6: WDS analysis of annealed U-10Zr alloy samples

Alloy	Matrix		Precipitate	
	U (wt%)	Zr (wt%)	U (wt%)	Zr (wt%)
U-10Zr_AC1d†	-	-	-	-
U-10Zr_AC3d	-	-	58.26	41.74
U-10Zr_AC7d	99.88	0.12	57.10	42.90
U-10Zr_AC30d	99.70	0.30	54.06	45.94
U-10Zr_GQ1d‡	-	-	-	-
U-10Zr_GQ3d	99.49	0.51	62.03	37.97
U-10Zr_GQ7d	99.41	0.59	60.65	39.35
U-10Zr_GQ30d	99.86	0.14	51.95	48.05

†ACxd: As-cast alloy annealed for x=1, 3, 7, 30 days

‡GQxd: γ-quenched alloy annealed for x=1, 3, 7, 30 days

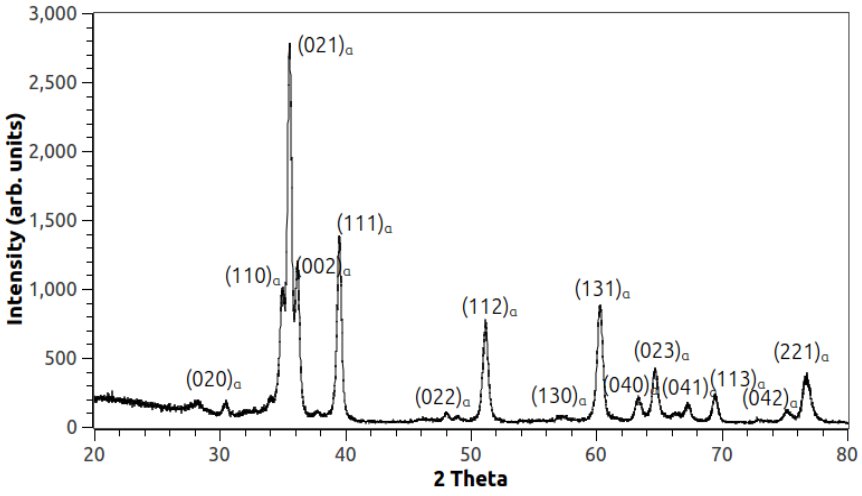

Fig. 4.42.: XRD pattern of as-cast U-10Zr alloy annealed for 7 days

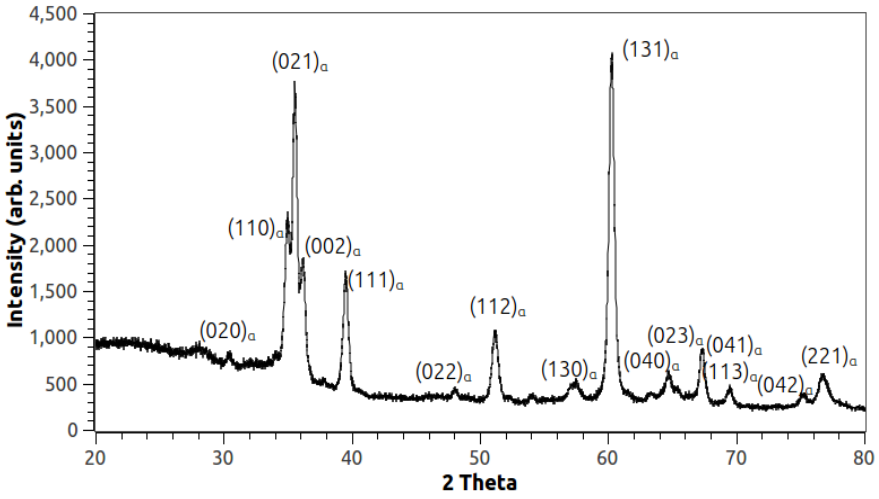

Fig. 4.43.: XRD pattern of as-cast U-10Zr alloy annealed for 30 days

XRD patterns of as-cast alloys annealed for 7 and 30 days are shown in Figures 4.42 and 4.43. Though the BSE images had two phase microstructure (Figures 4.41c and 4.41d), the XRD patterns only contained peaks for α-U.

Back scattered images of γ-quenched and annealed samples are shown in Figures 4.44a, 4.44b, 4.44c, and 4.44d. It is seen that after 1 day anneal the phase boundaries are diffuse while the diffuseness progressively decreased as the annealing time increased and they appear sharp after 30 days of annealing. WDS results are shown in Table 4.6 and are consistent with α-U as matrix and δ phase as Zr-rich regions. XRD data for samples γ-quenched and aged for 7 day and 30 days are shown in figures 4.45 and 4.46 respectively. Similar to as-cast and annealed samples, no peaks for δ phase were found and the only peaks observed were of α-U. Absence of δ phase peaks in both as-cast and annealed, and quenched and annealed samples is unusual considering the fact that peaks were observed in step-cooled sample (Figure 4.39). Moreover, the amount of Zr in the Zr-rich phase is very much consistent with δ phase composition. The only difference between the two thermal profiles is that, for step-

cooled sample, annealing was done cooling down from γ phase while these samples were annealed by raising from ambient temperature to 600^{o}C.

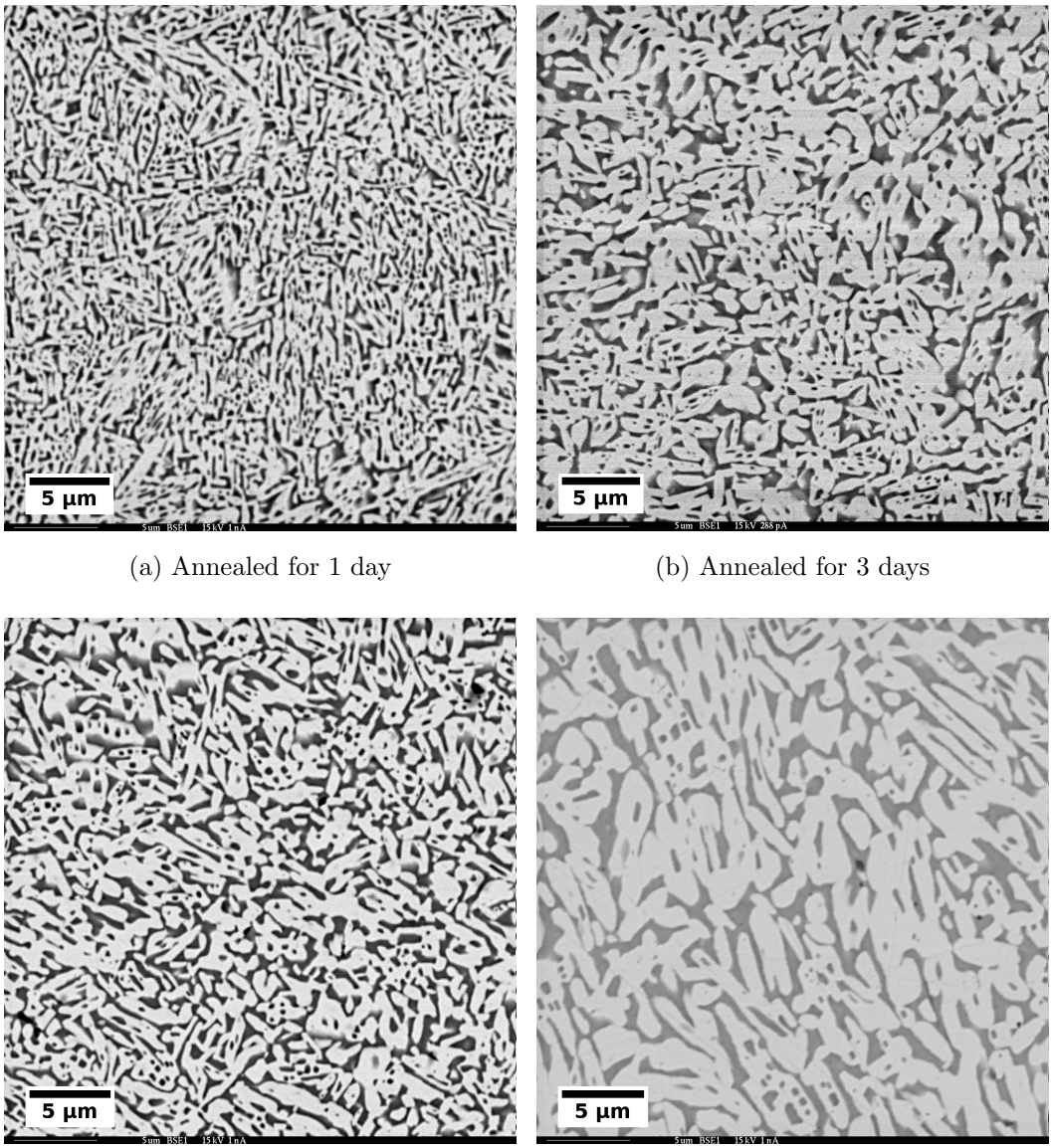

(a) Annealed for 1 day

(b) Annealed for 3 days

(c) Annealed for 7 days

(d) Annealed for 30 days

Fig. 4.44.: Back scattered images of U-10Zr alloy quenched from γ phase and annealed for various times at 600^{o}C

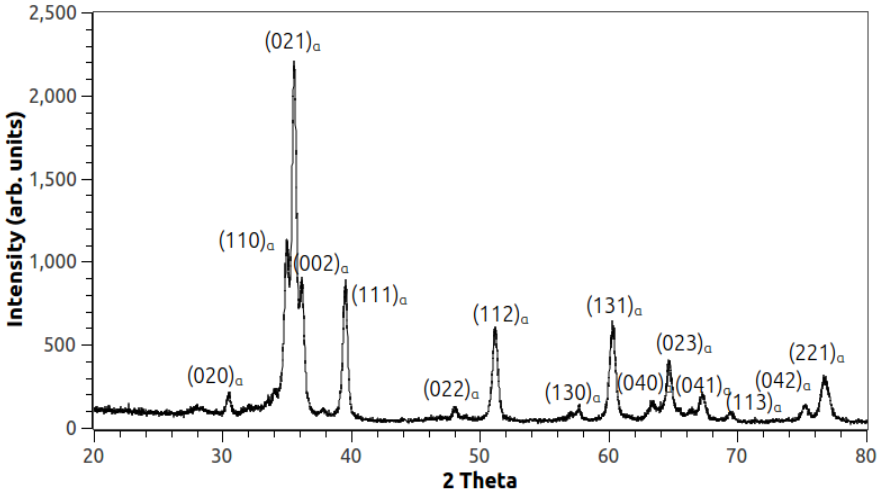

Fig. 4.45.: XRD pattern of U-10Zr alloy quenched from γ phase and annealed for 7 days

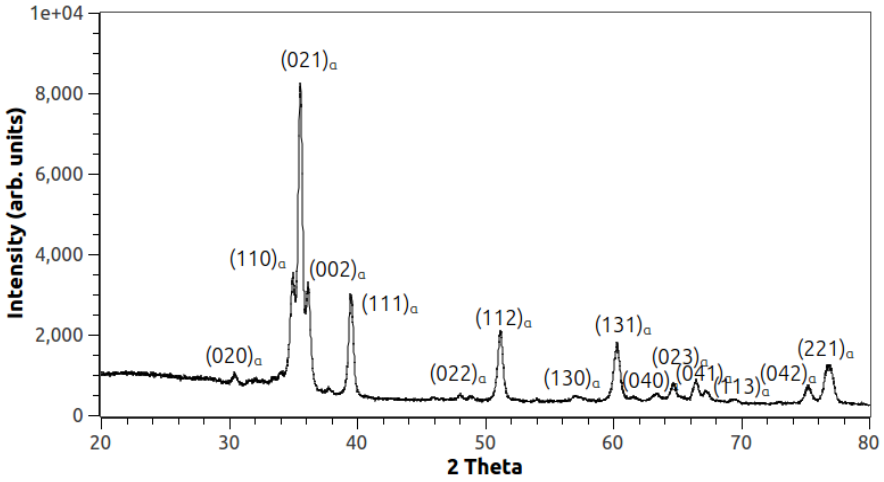

Fig. 4.46.: XRD pattern of U-10Zr alloy quenched from γ phase and annealed for 30 days

4.4 Metallurgy of U-20wt%Zr

4.4.1 As-cast and γ-Quenched Samples

Back scattered and optical images of as-cast U-20Zr alloy are shown in Figures 4.47a and 4.47b. It is seen that in the case of BSE image, α-U needles are formed in a matrix rich in Zr. This is in clear contrast with the images seen for U-2Zr, U-5Zr, and U-10Zr as-cast alloys where α-U was the matrix phase and the darker δ-type phase was the lamellae. The optical micrograph has regions rich in Zr, which are seen as bright regions (In the left grain in Figure 4.47b) and etching has brought this effect out quite well. Presence of α-U lamellae in Zr-rich matrix is clearly seen in the TEM bright field image shown in Figure 4.48a. The corresponding SAD pattern is shown in Figure 4.48b. From the XRD data shown in Figure 4.49, it is seen that both α-U and δ phase (indexed in red) are present which indicates that the matrix is infact the δ phase.

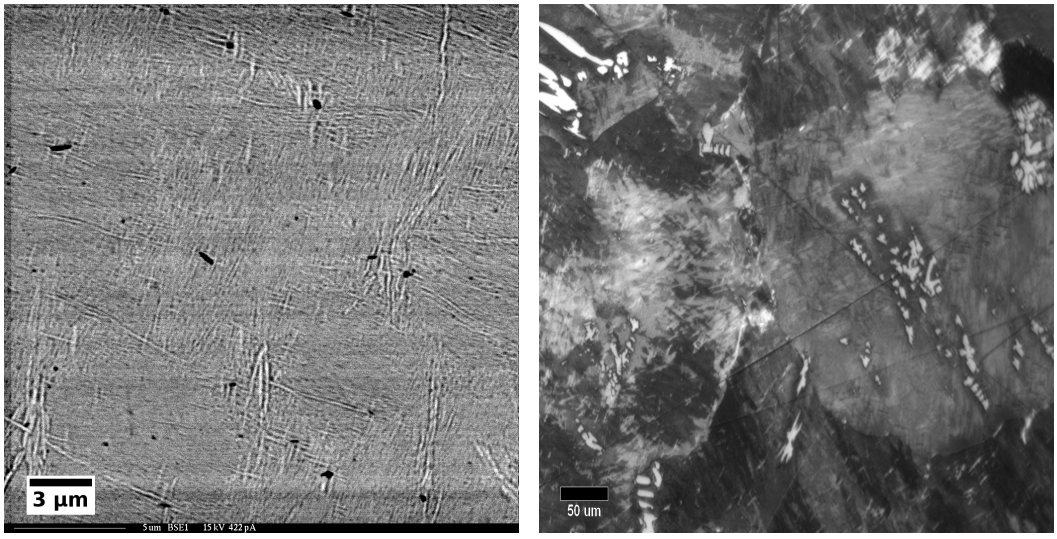

(a) BSE image (b) Optical (DIC) image

Fig. 4.47.: Back scattered and optical images of as-cast U-20Zr alloy

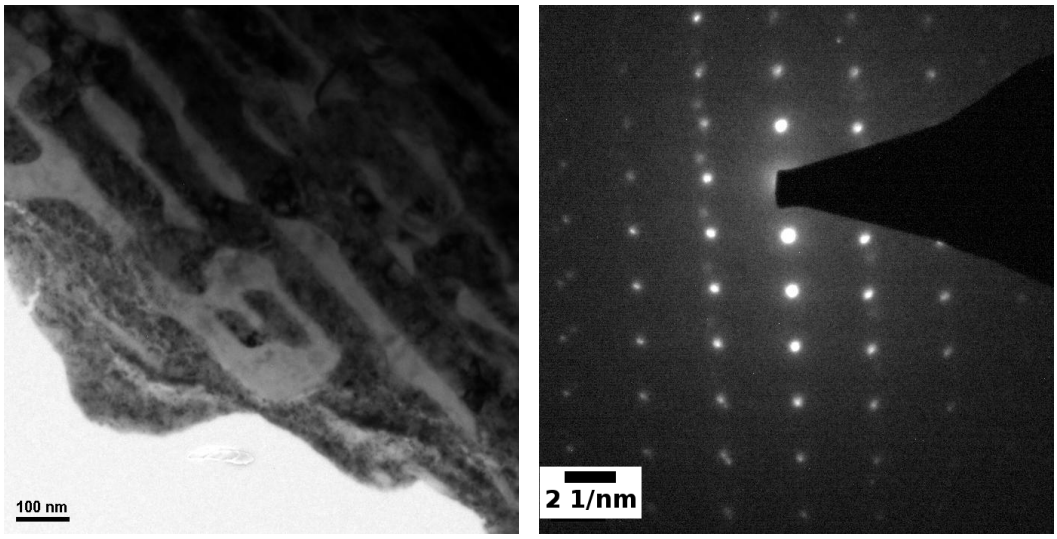

(a) Bright field image (b) SAD pattern

Fig. 4.48.: TEM images of as-cast U-20Zr alloy

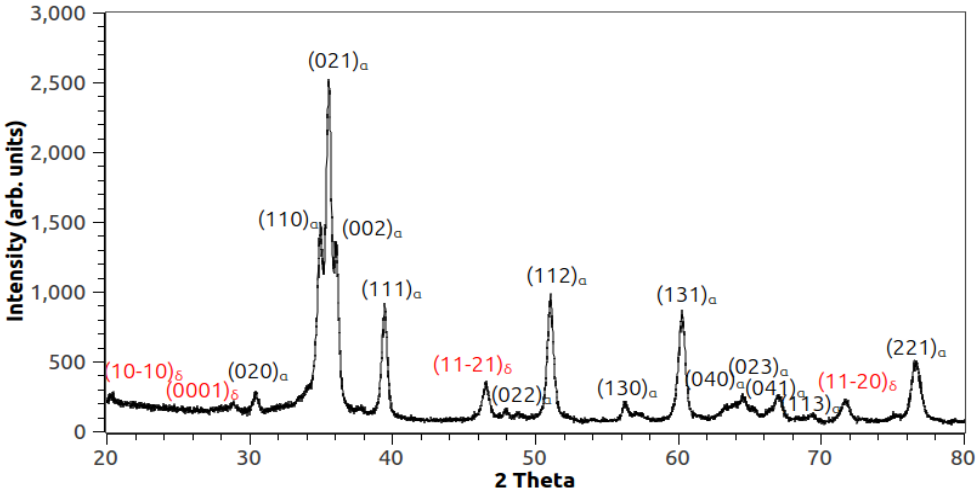

Fig. 4.49.: XRD pattern of as-cast U-20Zr alloy

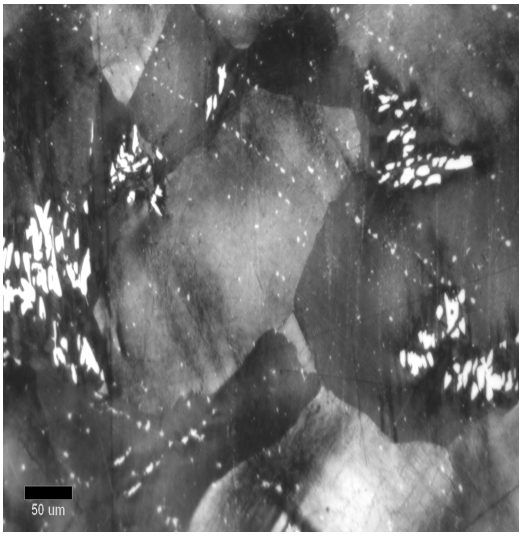

Fig. 4.50.: Optical (DIC) image of γ-quenched U-20Zr alloy

Optical micrograph of γ-quenched alloy is shown in Figure 4.50 and contains remnant γ grain boundaries of $\sim$100 μm size. Oxygen/Carbon stabilized Zr precipitates are seen as clusters (One such cluster is seen in the left side of the image) in the image. Figure 4.51 shows XRD pattern of the quenched alloy and peaks corresponding to ω phase are seen (indexed in red). Incomplete collapse of $(111)_\gamma$ planes is manifested in the form of broad peaks as seen in the XRD pattern. Comparing the XRD patterns of as-cast and γ-quenched alloy, it is seen that the 2θ positions for δ and ω are the same (peaks are seen at 20.4^o, 28.9^o, 46.6^o, and 71.8^o) with they appearing relatively broad in quenched alloy. It then becomes important to set some criteria for distinguishing these two phases. This aspect is taken up later in Chapter 6 and will be used to make a case on how it might be more appropriate to call these phases as diffusional-ω and athermal-ω in as-cast and quenched alloys respectively. But, in the present context, convention is maintained where they are referred to as δ and ω in as-cast and quenched alloys respectively.

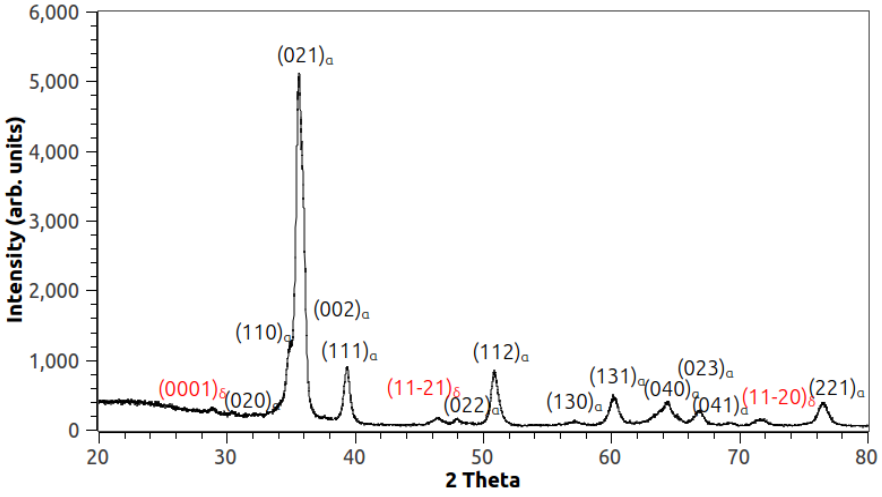

Fig. 4.51.: XRD pattern of γ-quenched U-20Zr alloy

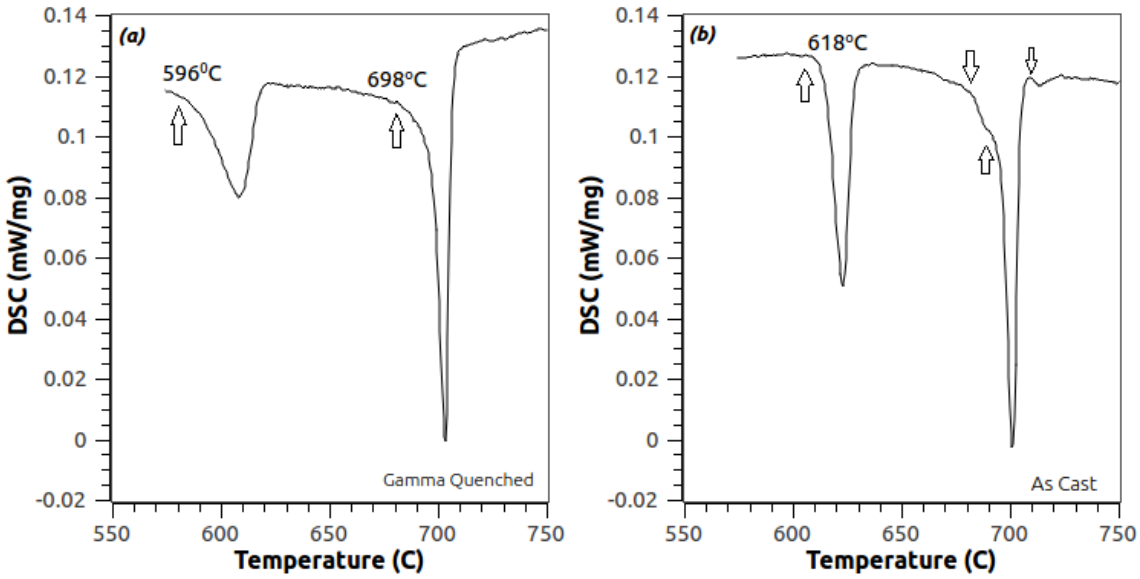

Fig. 4.52.: DSC curves of U-20Zr alloy showing various transformations (indicated by arrows)

DSC curves of γ-quenched and as-cast alloys are shown in Figure 4.52. Two transformations are seen in quenched alloy as opposed to four in as cast alloy. Moreover, the transformation at 618^{o}C in as-cast alloy which corresponds to $\delta \rightarrow \gamma$ has shifted to a lower temperature i.e 596^{o}C in quenched alloy and this transformation corresponds to $\omega \rightarrow \gamma$ since ω is present besides $\alpha^{'}$ as ambient temperature phase.

4.4.2 Samples Step-Cooled from the γ Phase

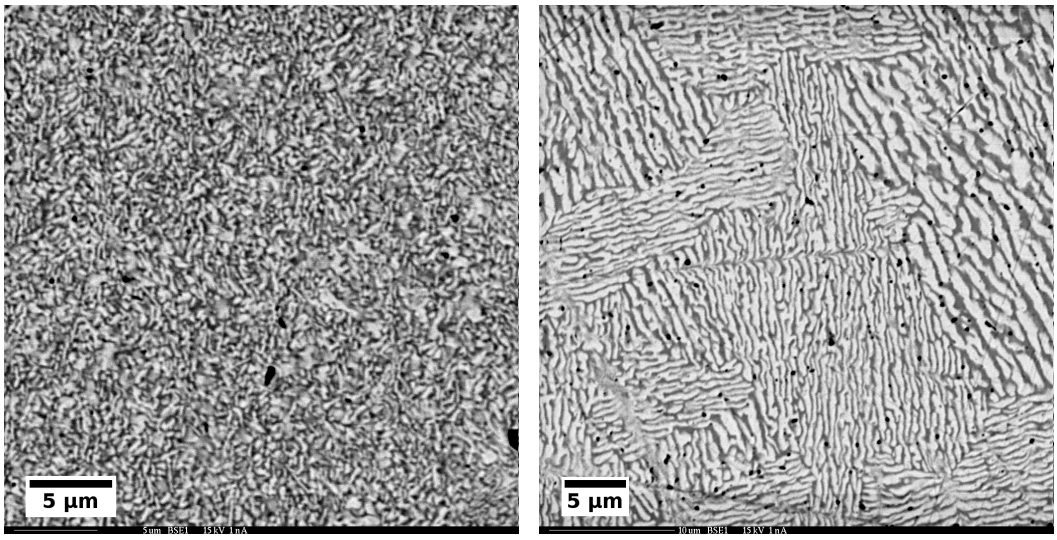

(a) $\gamma \xrightarrow{(\alpha+\gamma)}$ 30 min and quenched (b) $\gamma \xrightarrow{(\alpha+\gamma)}$ 2 days and quenched

Fig. 4.53.: BSE images of step-cooled U-20Zr alloys

An alloy button was annealed in a molten salt bath maintained at 640^{o}C for 30 min and quenched in water. This experiment was conducted to retain $(\alpha + \gamma)$ microstructure by annealing in molten salt bath. Back scattered image of corresponding sample is shown in Figure 4.53a and is seen to consist of diffuse bright and dark regions without sharp boundaries. This mode of heat treatment was not pursued further and alloy sample was step-cooled from γ phase and annealed at 650^{o}C

by sealing the alloy button in a fused quartz tube. Back scattered image of the sample is shown in Figure 4.53b. Bright and dark alternate lamellae are seen and XRD pattern corresponding to this sample consisted of only α-U peaks as shown in Figure 4.54.

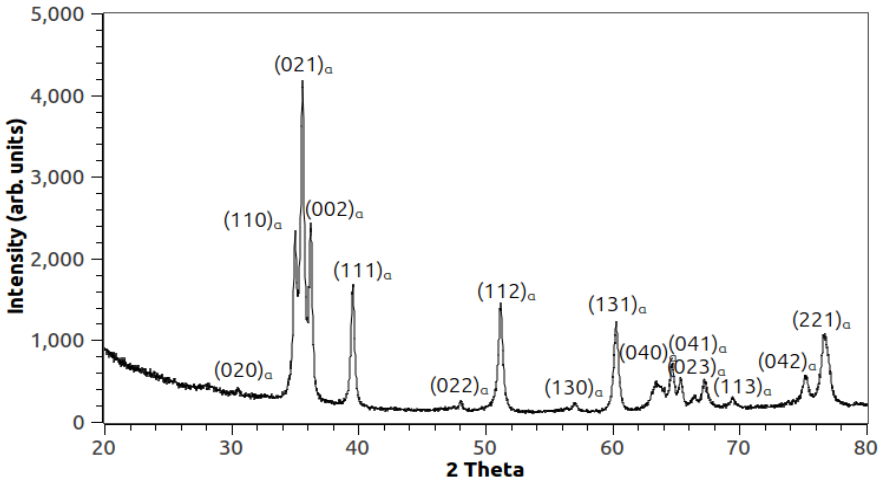

Fig. 4.54.: XRD pattern of U-20Zr alloy step-cooled from $\gamma \xrightarrow[650C]{(\alpha+\gamma)}$ 2 days and quenched

4.4.3 Samples Annealed at 600^{o}C

Back scattered images of as-cast samples annealed at 600^{o}C are shown in Figures 4.55a, 4.55b, 4.55c, and 4.55d. In contrast to annealed samples of U-2Zr, U-5Zr, and U-10Zr, the matrix here consists of Zr-rich phase and needle like precipitates primarily consisting of uranium. The microstructure essentially remains the same in all cases indicating that equilibrium has been reached after 1 day of annealing. Results on compositional analysis on these alloys are given in Table 4.7 and it can be inferred that the matrix is δ phase while the precipitates are α-U.

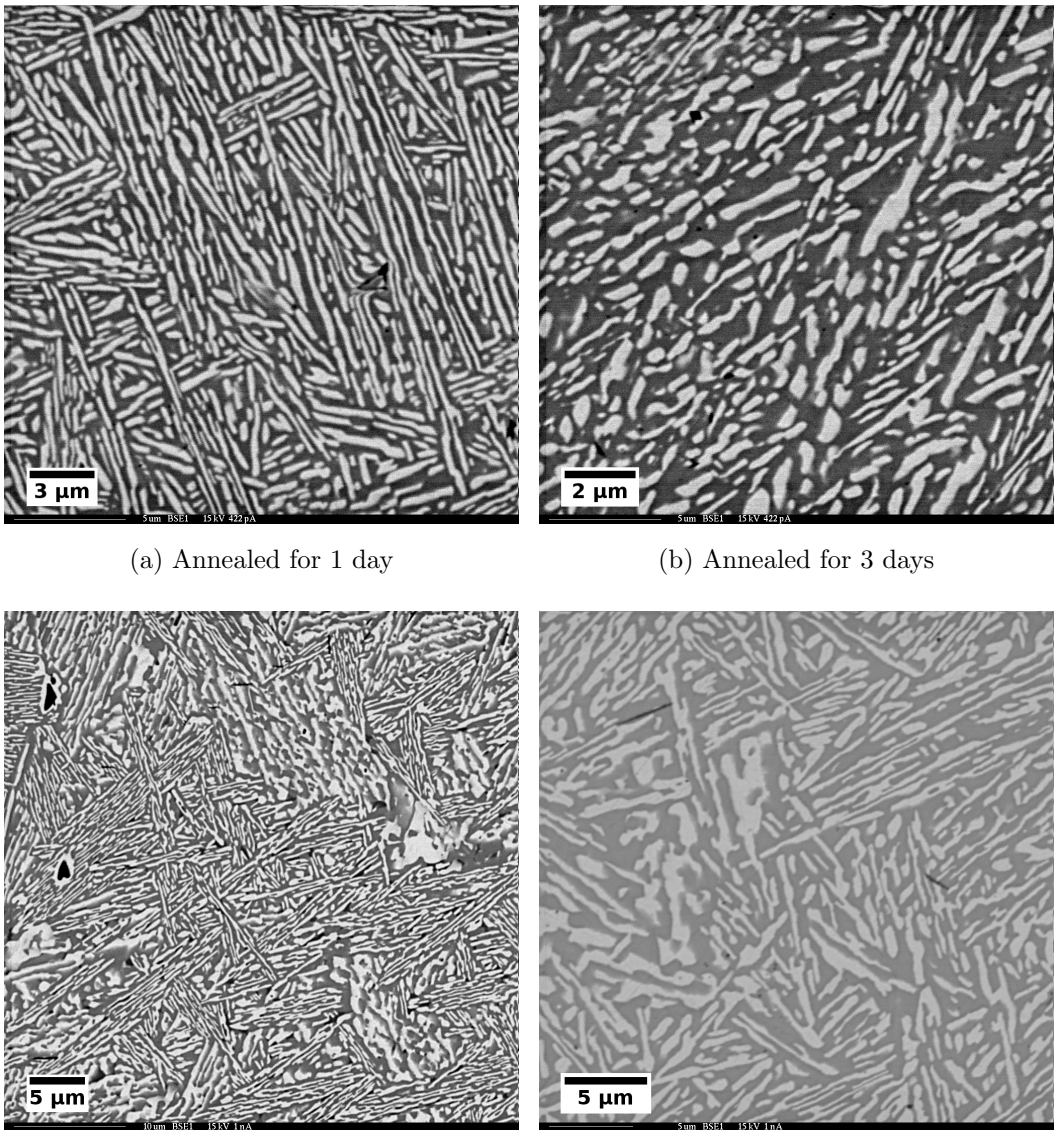

(a) Annealed for 1 day

(b) Annealed for 3 days

(c) Annealed for 7 days

(d) Annealed for 30 days

Fig. 4.55.: BSE images of as-cast U-20Zr alloy annealed for various times at 600^{o}C

It is also seen that the amount of Zr in the δ phase in all the annealed alloys is $\sim$40wt%, less than what was found for annealed U-5Zr and U-10Zr alloys. Detection of lower amount of Zr can be attributed to the microstructure in annealed alloys. Considering the close proximity of the two phases spatially, a significant contribution

from α-U from the precipitate can be expected which would amount to a reduction in the Zr contribution from the matrix (δ phase).

Table 4.7: WDS analysis of annealed U-20Zr alloy samples

Alloy	Precipitate		Matrix	
	U (wt%)	Zr (wt%)	U (wt%)	Zr (wt%)
U-20Zr_AC1d[†]	98.10	1.90	61.50	38.50
U-20Zr_AC3d	97.94	2.06	59.34	40.66
U-20Zr_AC7d	98.41	1.59	60.63	39.37
U-20Zr_AC30d	-	-	61.88	38.12
U-20Zr_GQ1d[‡]	-	-	-	-
U-20Zr_GQ3d	97.94	2.06	57.82	42.18
U-20Zr_GQ7d	99.42	0.58	55.26	44.74
U-20Zr_GQ30d	99.84	0.16	47.95	52.05

[†]ACxd: As-cast alloy annealed for x=1, 3, 7, 30 days

[‡]GQxd: γ-quenched alloy annealed for x=1, 3, 7, 30 days

X-ray diffraction patterns of 7 day and 30 day annealed samples of as-cast alloys are shown in Figures 4.56 and 4.57. The striking feature immediately apparent from these patterns is that the δ peaks which were present in the as-cast alloy (Figure 4.49) have vanished upon annealing. Disappearance of peaks after 7 days annealing cannot be explained if δ phase is present in as-cast alloy since it is the stable phase at room temperature as per the binary U-Zr phase diagram [119]. The only effect of annealing should be coarsening of the δ phase which is already present in the as-cast alloy which inturn should reflect as sharp peaks in XRD pattern. On the other hand, it can be explained if the diffusional-ω is present instead of δ. This idea will be pursued and built upon in Chapter 5.

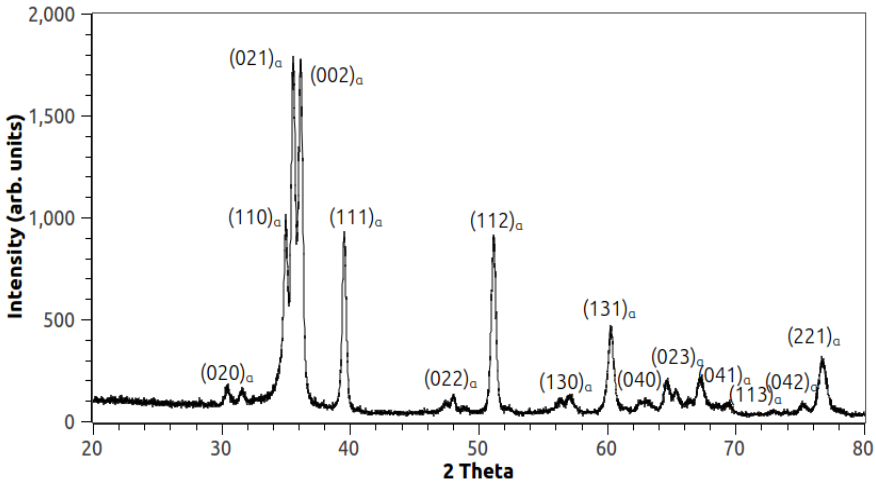

Fig. 4.56.: XRD pattern of as-cast U-20Zr alloy annealed for 7 days

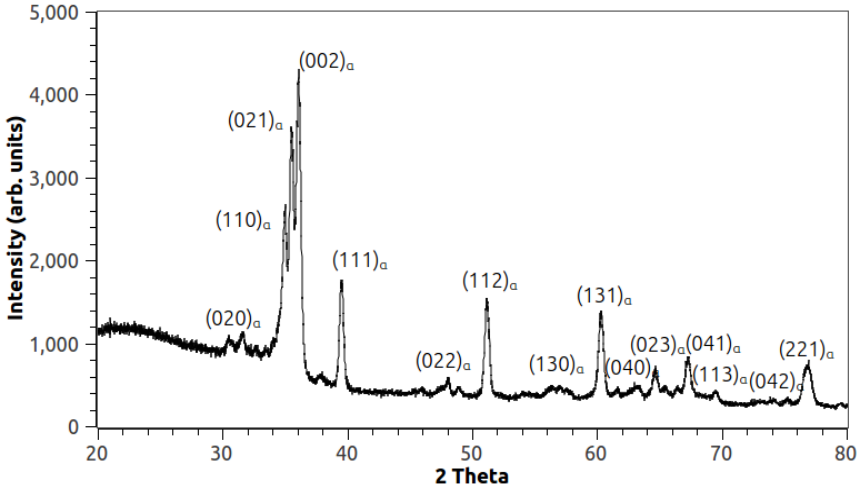

Fig. 4.57.: XRD pattern of as-cast U-20Zr alloy annealed for 30 days

Back scattered images of γ-quenched and annealed samples are shown in Figures 4.58a, 4.58b, 4.58c, and 4.58d. Diffuse phase boundaries are seen after 1 day annealing and they became progressively sharp as the annealing time increased.

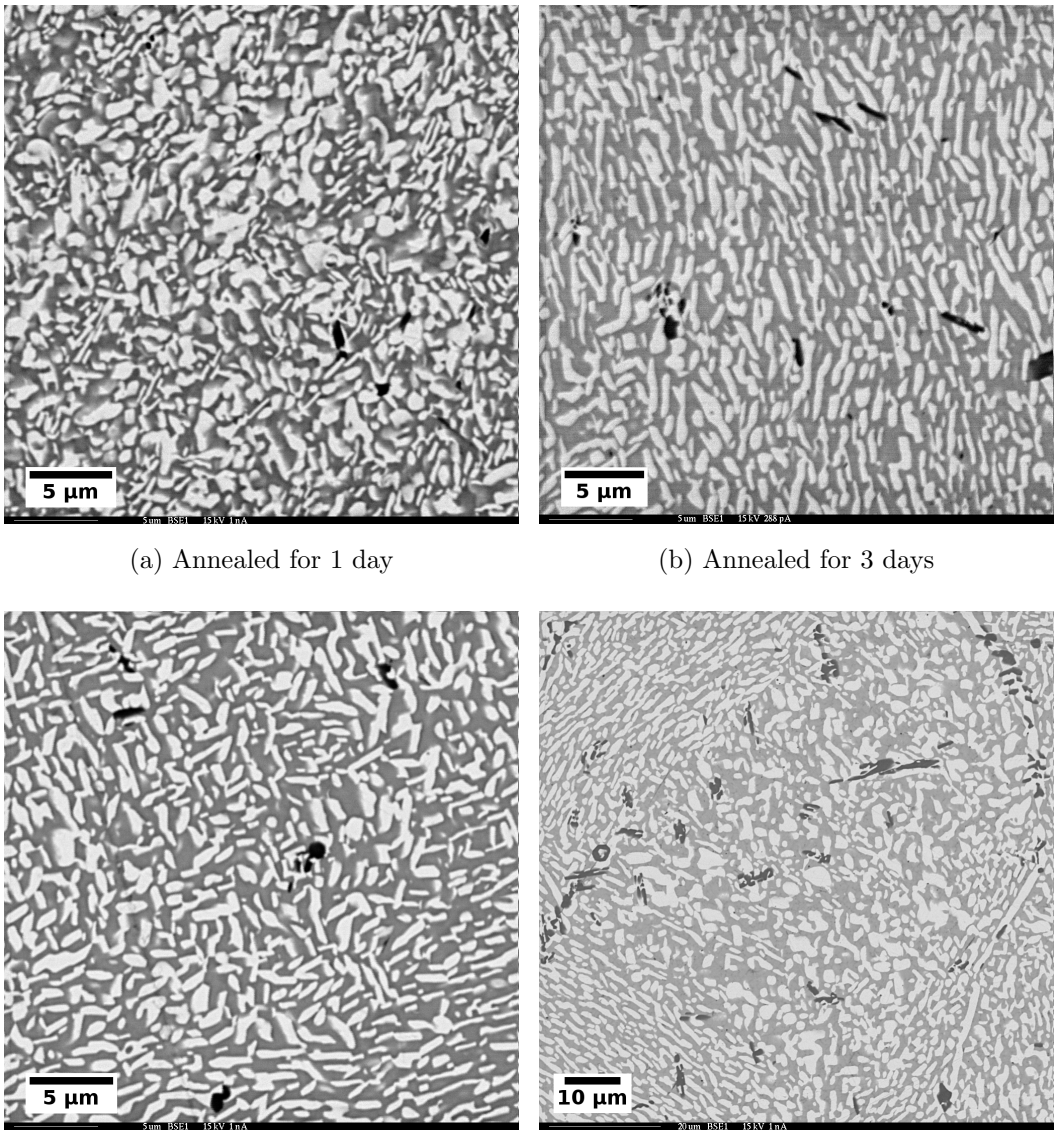

(a) Annealed for 1 day

(b) Annealed for 3 days

(c) Annealed for 7 days

(d) Annealed for 30 days

Fig. 4.58.: BSE images of U-20Zr alloy quenched from γ phase and annealed for various times at 600^{o}C

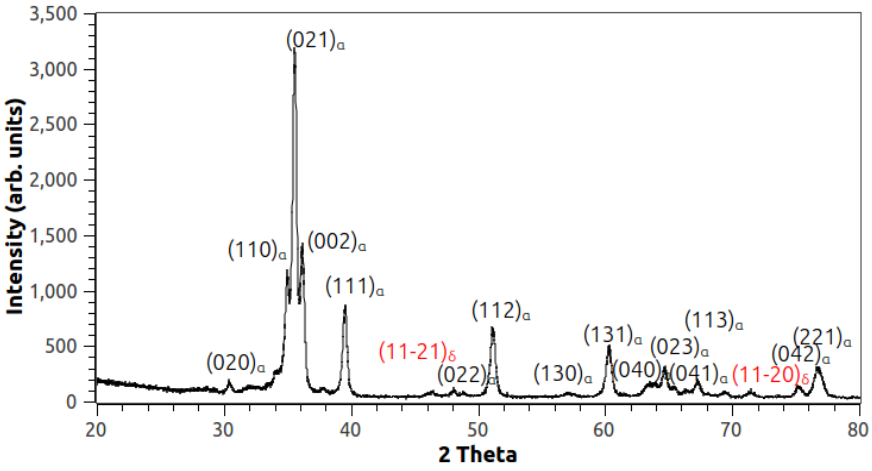

Fig. 4.59.: XRD pattern of U-20Zr alloy quenched from γ phase and annealed for 7 days

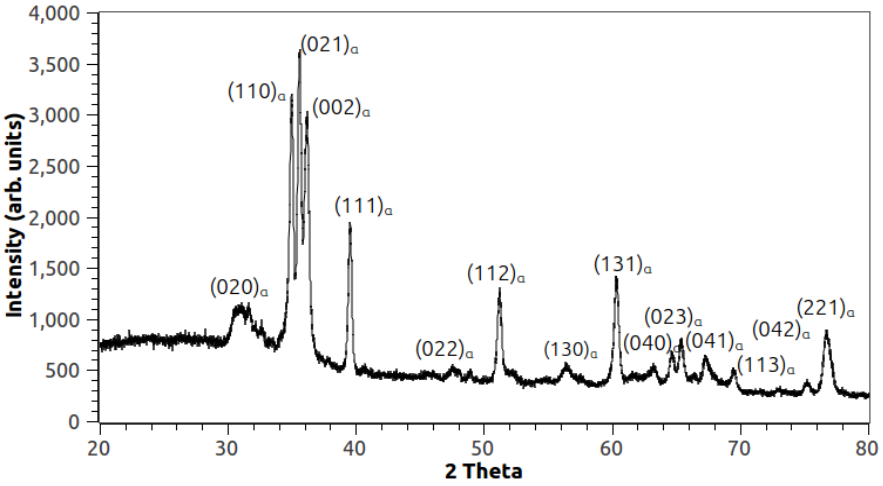

Fig. 4.60.: XRD pattern of U-20Zr alloy quenched from γ phase and annealed for 30 days

Also seen are α-U precipitates with oblong and in needle shapes. In contrast to as-cast and annealed samples, the U-rich precipitate needles in these samples are much smaller in size. Compositional analysis results are shown in Table 4.7 and it can be inferred that the amount of Zr in the δ phase is much higher as compared to the ones in as-cast and annealed samples. This again is explained by considering the microstructures of the quenched and annealed alloys. Here, the precipitates, as mentioned, are much smaller as compared to as-cast and annealed samples and hence the contribution of α-U from the precipitates to the δ phase composition is reduced. XRD patterns for γ-quenched samples annealed for 7 and 30 days are shown in Figures 4.59 and 4.60. Peaks for δ phase are seen after 7 day annealing but vanished after 30 day annealing. This again is one of the more provocative findings in this study and can be explained as follows. When this alloy is quenched from γ phase, $\alpha^{'}$ and athermal-ω are formed along with some retained[5] γ. During annealing, by the end of 7 days, the retained γ transforms to ω by isothermal ω transformation (Refer Section 2.2.2) which is reflected in the XRD pattern of the 7 day annealed sample (Figure 4.59) and after 30 days of annealing, has vanished (This is seen in XRD pattern of 30 day annealed sample shown in Figure 4.60) since ω is inherently a metastable phase in Zr alloys [94].

4.5 Metallurgy of U-30wt%Zr

4.5.1 As-cast and γ-Quenched Samples

Back scattered and bright field TEM images of as-cast U-30Zr alloy are shown in Figures 4.61a and 4.61b. In the BSE image, the microstructure is seen to consist of very fine lamellae which could not be resolved. On the other hand, bright field TEM image clearly shows α-U lamellae with a single orientation in a δ phase matrix.

[5]This is seen from Figure 4.51 as overlapping of $(021)_\alpha$ and $(002)_\alpha$ lines. This is an indication of retention of γ phase

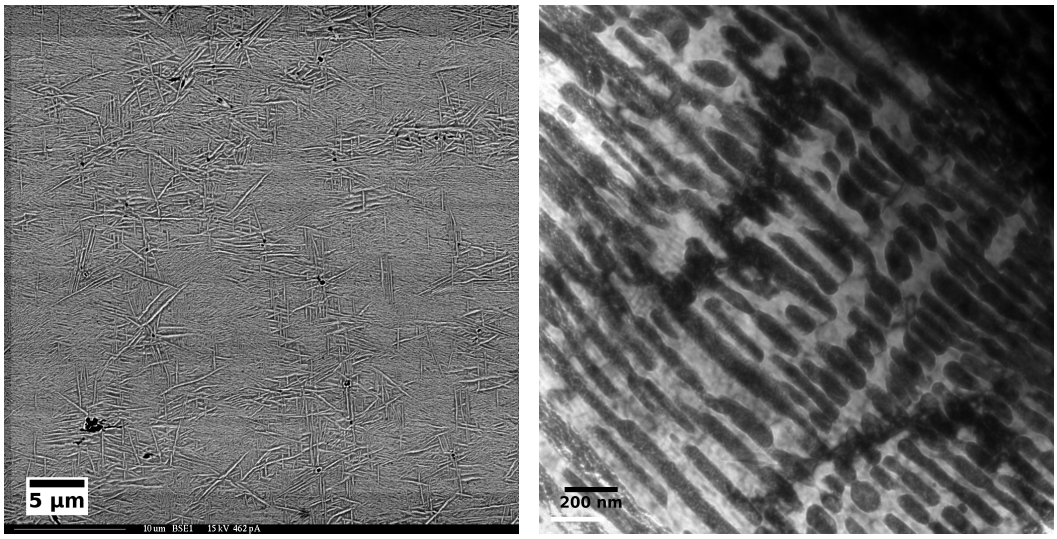

(a) BSE image (b) Bright field TEM image

Fig. 4.61.: Back scattered and TEM images of as-cast U-30Zr alloy

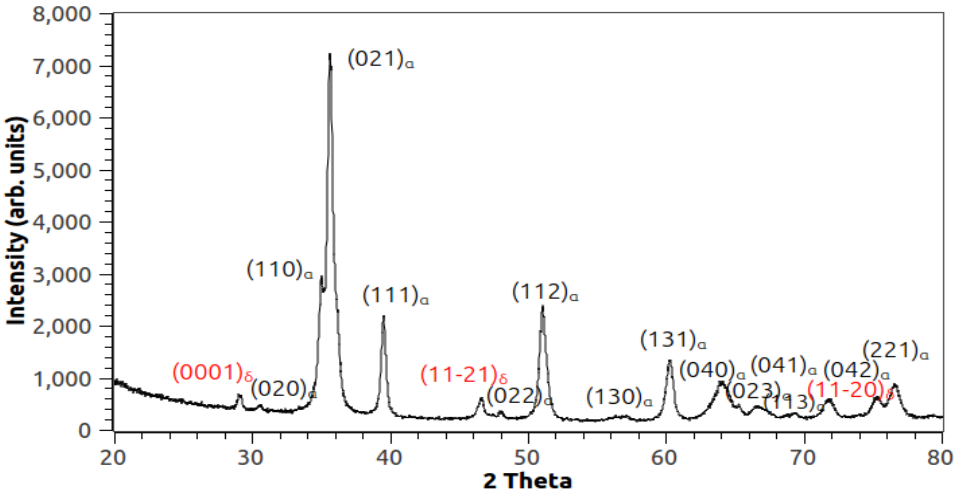

Fig. 4.62.: XRD pattern of as-cast U-30Zr alloy

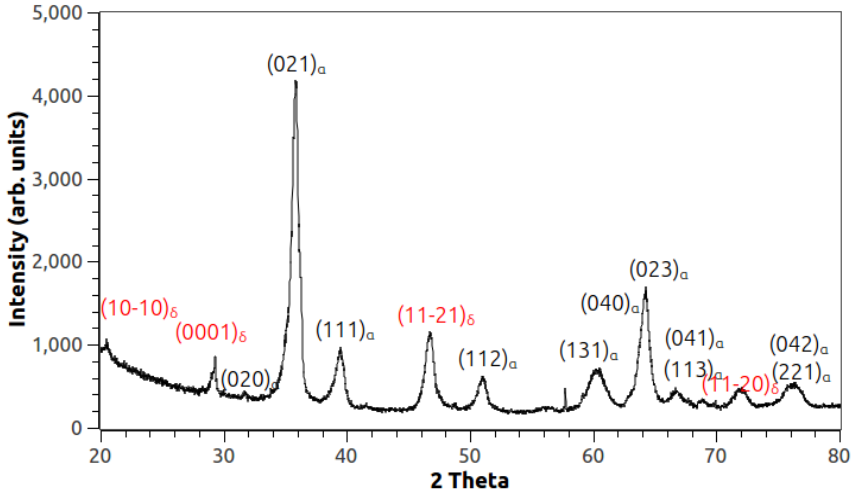

Fig. 4.63.: XRD pattern of γ-quenched U-30Zr alloy

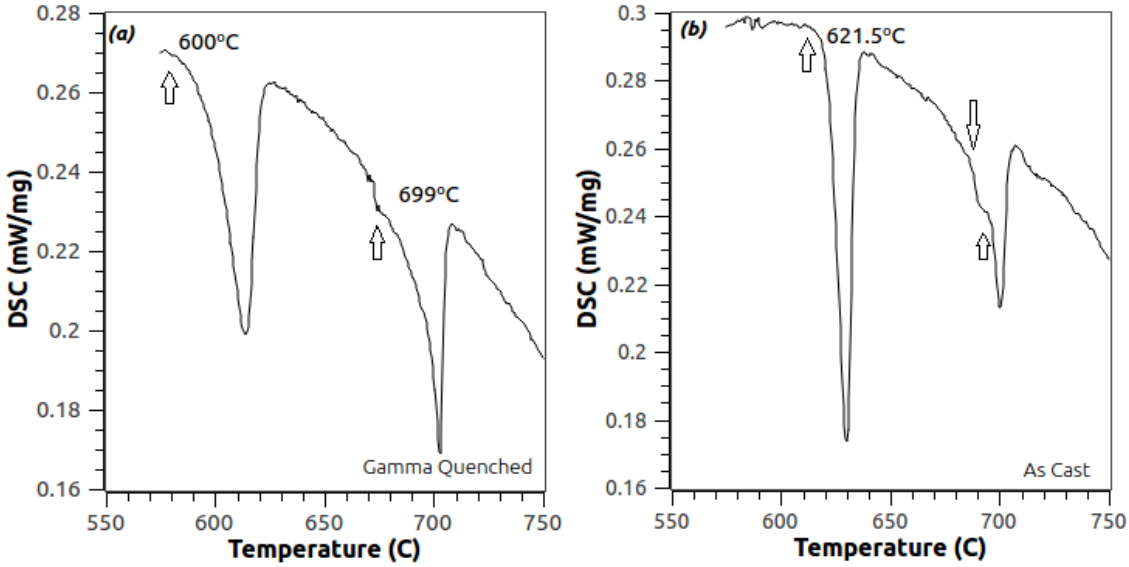

Fig. 4.64.: DSC curves of quenched and as-cast U-30Zr alloy showing various transformations (indicated by arrows)

XRD pattern of as-cast alloy shown in Figure 4.62 consists of α-U peaks and δ phase peaks (indexed in red). In the case of γ-quenched alloy, peaks for both α-U and ω phase are seen in the XRD pattern (Figure 4.63). A visible overlapping of $(002)_\alpha$ and $(021)_\alpha$ while $(110)_\alpha$ line is seen just as a faint shoulder peak to $(021)_\alpha$. This is a possible indication of retained γ in the quenched alloy as it was not observed in any of the quenched U-2Zr, U-5Zr, and U-10Zr alloys. It is pointed that XRD patterns for as-cast and quenched alloys are similar to the quenched alloy of U-20Zr (Figures 4.49 and 4.51).

DSC curves of γ-quenched and as-cast alloys are shown in Figure 4.64. Two transformations are seen in the case of quenched alloy while three transformations are seen in as-cast alloy. The transformation associated with $\delta \rightarrow \gamma$ in as-cast alloy shifted from 621.5^{o}C to 600^{o}C in quenched alloy. The transformation in latter case corresponds to $\omega \rightarrow \gamma$ since the phases present as $\alpha^{'}$, ω, and some retained γ.

4.5.2 Samples Step-Cooled from the γ Phase

Back scattered image of the alloy sample heat treated in a molten salt bath maintained at 640^{o}C is shown in Figure 4.65a. A two phase microstructure is seen but is not clearly resolved. This, along with a U-20Zr (Figure 4.53a) alloy were annealed in the salt bath to retain $(\alpha + \gamma)$ microstructure. As was the case with U-20Zr alloy, this sample was not analyzed any further. Instead, the sample was annealed in a vacuum sealed fused quartz tube and step-cooled and annealed at 650^{o}C. Back scattered image of this alloy sample is shown in Figure 4.65b. It is seen that the microstructure consists of γ phase matrix and α-U precipitates shaped as needles/rods. X-ray diffraction pattern for alloy step-cooled and annealed at 650^{o}C is shown in Figure 4.66. It is seen that only peaks corresponding to α-U are present.

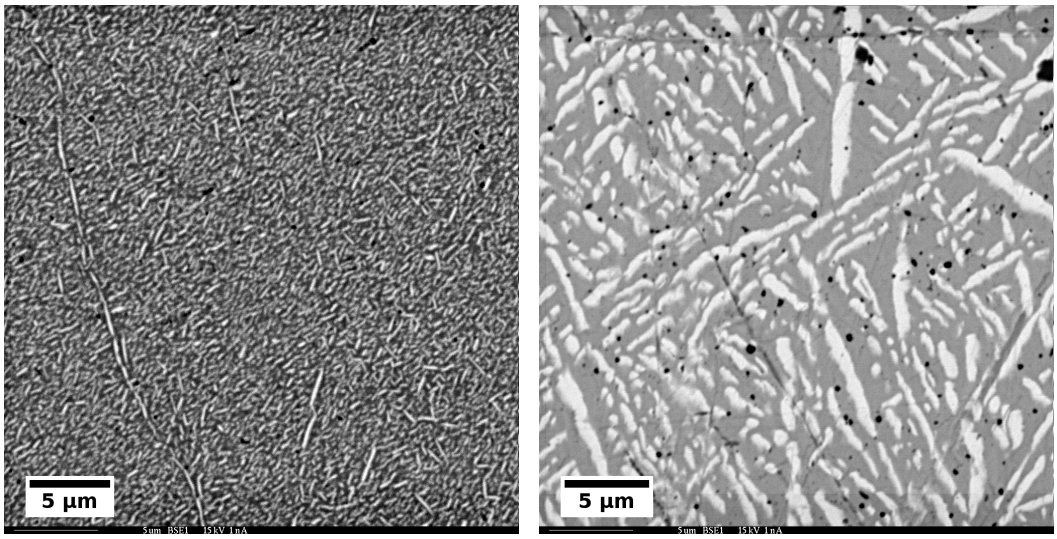

(a) $\gamma \xrightarrow{(\alpha+\gamma)}$ 30 min and quenched (b) $\gamma \xrightarrow{(\alpha+\gamma)}$ 2 days and quenched

Fig. 4.65.: BSE images of step-cooled U-30Zr alloys

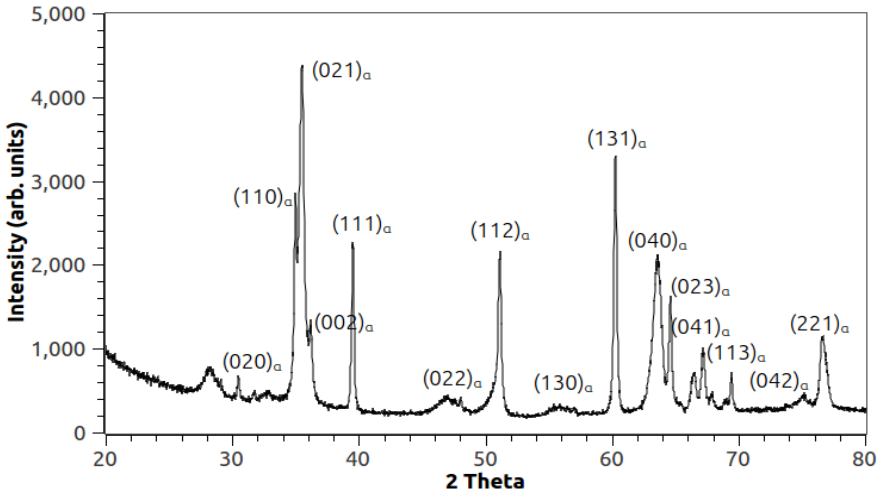

Fig. 4.66.: XRD pattern of U-30Zr alloy step-cooled from $\gamma \xrightarrow[650C]{(\alpha+\gamma)}$ 2 days and quenched

4.5.3 Samples Annealed at 600^{o}C

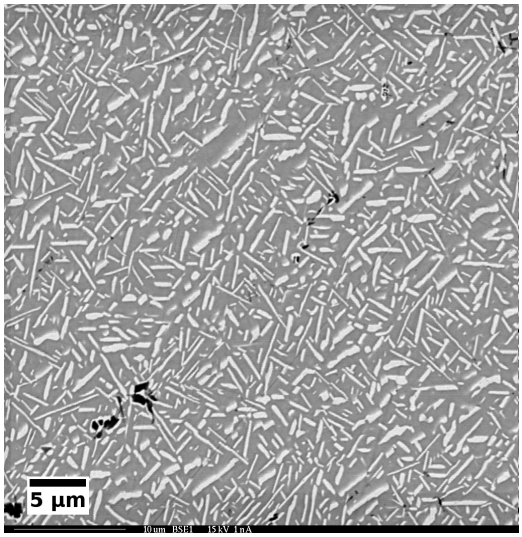

(a) Annealed for 1 day

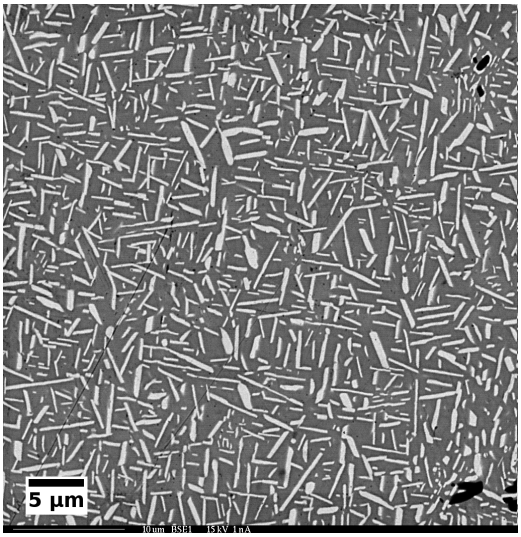

(b) Annealed for 3 days

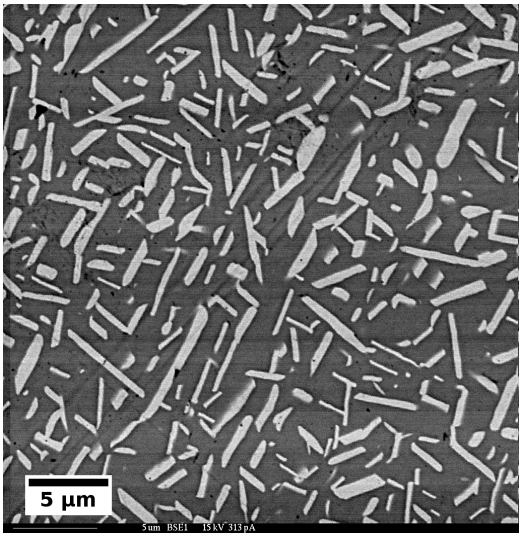

(c) Annealed for 7 days

Fig. 4.67.: BSE images of as-cast U-30Zr alloys annealed for different times at 600^oC

Back scattered images of as-cast and annealed samples are shown in Figures 4.67a, 4.67b, and 4.67c. Similar to U-20Zr alloy, the microstructure consists of δ phase with needle like precipitates of α-U. Here, the precipitates are less in number, sizes are much smaller and are sharper as compared to those in annealed U-20Zr alloys (Figures 4.55a, 4.55b, 4.55c, and 4.55d). Results of compositional analysis are shown in Table 4.8 and are consistent with the compositions of δ and α-U phases.

Table 4.8: WDS analysis of annealed U-30Zr alloy samples

Alloy	Precipitate		Matrix	
	U (wt%)	Zr (wt%)	U (wt%)	Zr (wt%)
U-30Zr_AC1d†	94.78	5.22	63.70	36.30
U-30Zr_AC3d	99.25	0.75	56.61	43.39
U-30Zr_AC7d	99.45	0.55	56.67	43.33
U-30Zr_GQ1d‡	-	-	-	-
U-30Zr_GQ3d	99.71	0.29	53.44	46.56

†ACxd: As cast alloy annealed for x=1, 3, 7 days

‡GQxd: γ-quenched alloy annealed for x=1, 3 days

Back scattered images of quenched and annealed alloys are shown in Figures 4.68a and 4.68b. Similar to the results of other alloys, the phase boundaries after 1 day annealing were diffuse and became quite sharp after 3 days of annealing. WDS reaults are shown in Table 4.8 and are consistent with δ phase matrix and α-U precipitates.

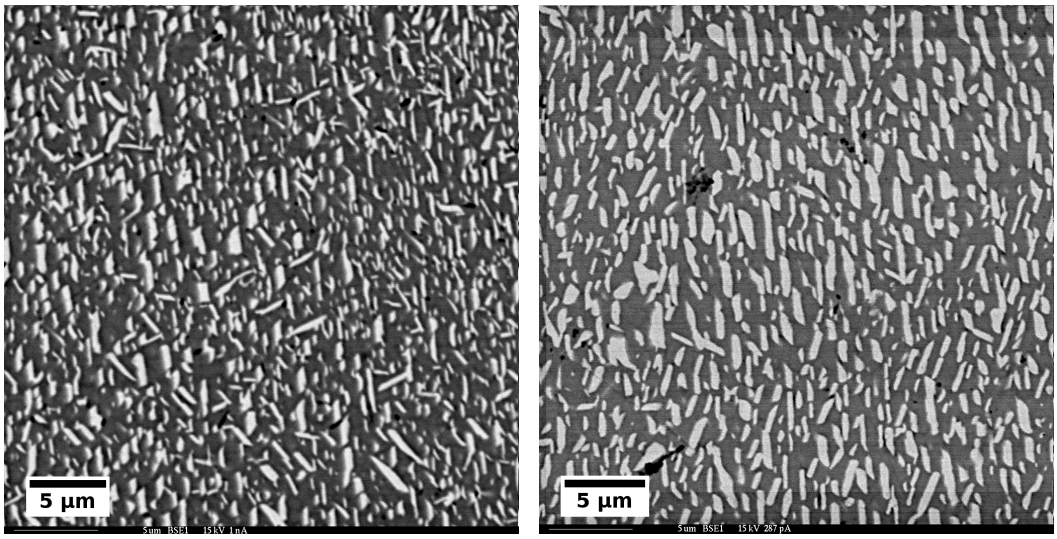

(a) Annealed for 1 day (b) Annealed for 3 days

Fig. 4.68.: BSE images of U-30Zr alloys quenched from γ phase and annealed for different times at 600^oC

4.6 Metallurgy of U-50wt%Zr

4.6.1 As-cast and γ-Quenched Samples

Microstructures of U-50Zr alloy, being of single phase (δ), did not show any contrast in back scattered mode of imaging. Moreover, they did not respond to etching (Refer Section 3.2.1) and did not reveal grain boundaries. Basak et al [106], in their study on U-50Zr alloys, used HF as the etchant which was not used in this study. X-ray diffraction patterns for as-cast and γ-quenched alloys are shown in Figures 4.69 and 4.70. It is seen that quenched alloy as fewer peaks and are associated with both retained γ phase and athermal ω phase. The as-cast alloy on the other hand has δ phase peaks as expected from the phase diagram [119]. An apparent difference in the two patterns in terms of peak heights is also seen. However, if the

peak intensities in both cases are normalized to the highest intensity line, a very small difference is seen between the patterns.

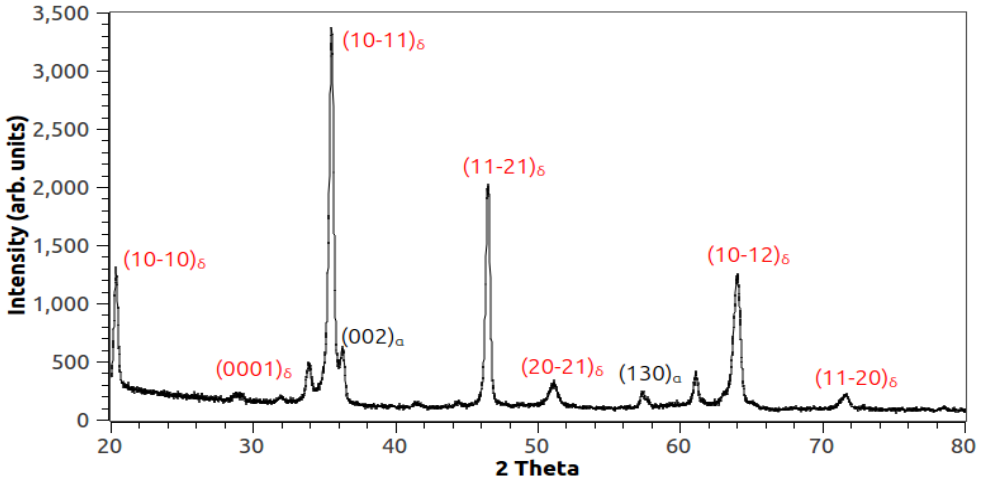

Fig. 4.69.: XRD pattern of as-cast U-50Zr alloy

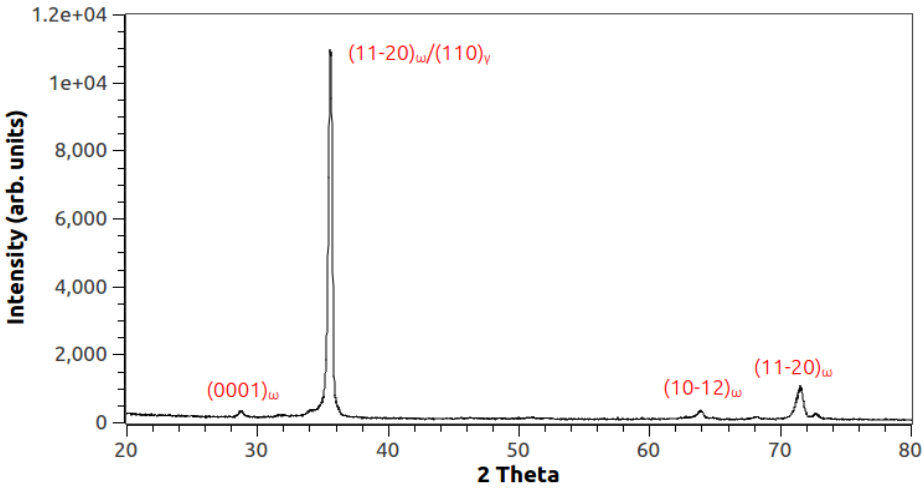

Fig. 4.70.: XRD pattern of γ-quenched U-50Zr alloy

.

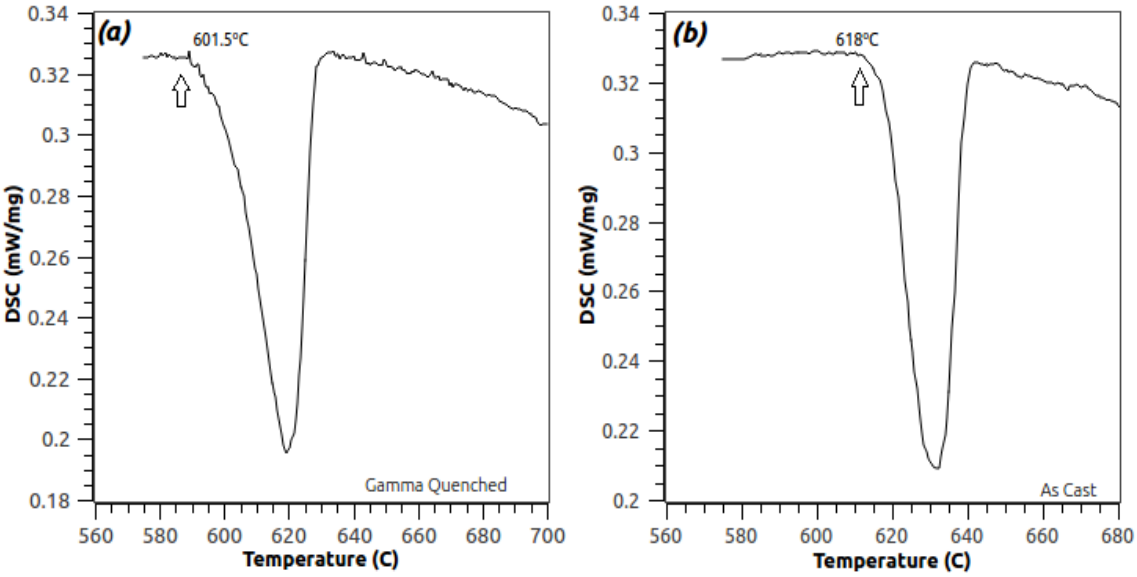

Fig. 4.71.: DSC curves of U-50Zr alloy showing a single transformation

DSC curves of as-cast and quenched alloys consist of only single transformation as seen in Figure 4.71. In case of quenched alloy the peak during heating, it corresponds to $\omega \rightarrow \gamma$ transformation because of the formation of athermal-ω in the quenched alloy, while for as-cast alloy, it is $\delta \rightarrow \gamma$ transformation. It is also seen that the transformation temperature is lowered from 618^{o}C in as-cast alloy to 601.5^{o}C for the quenched alloy.

4.6.2 Samples Annealed at 600^{o}C

XRD patterns of as-cast alloys annealed for 7 and 30 days are shown in Figures 4.72 and 4.73. Due to the presence of oxygen, it is seen that the peaks for δ phase have diminished and those of α-U have appeared by the end of 30 day anneal. On the contrary, 7 day annealed sample still had peaks for δ phase along with very few α-U peaks of low intensity indicating that very few precipitates of α-U have formed.

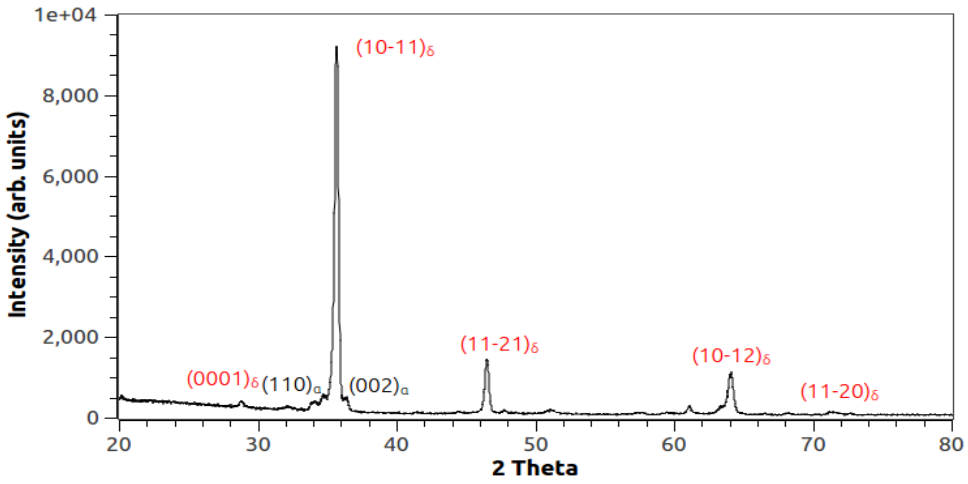

Fig. 4.72.: XRD pattern of as-cast U-50Zr alloy annealed for 7 days

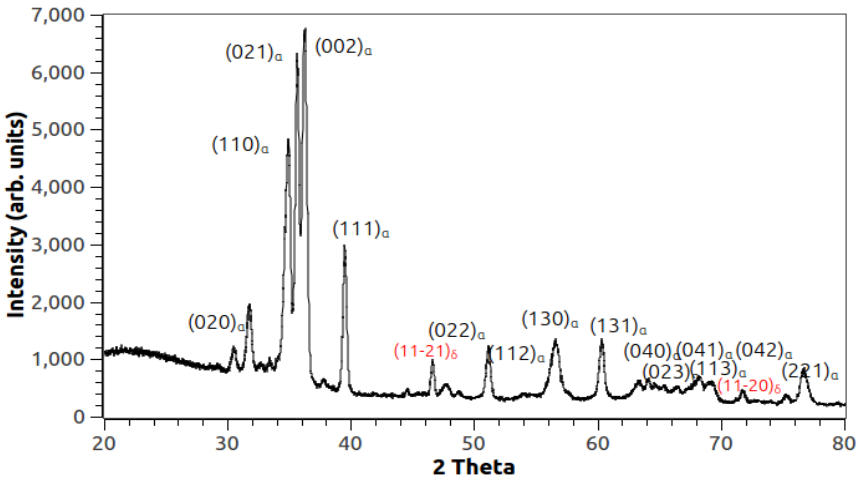

Fig. 4.73.: XRD pattern of as-cast U-50Zr alloy annealed for 30 days

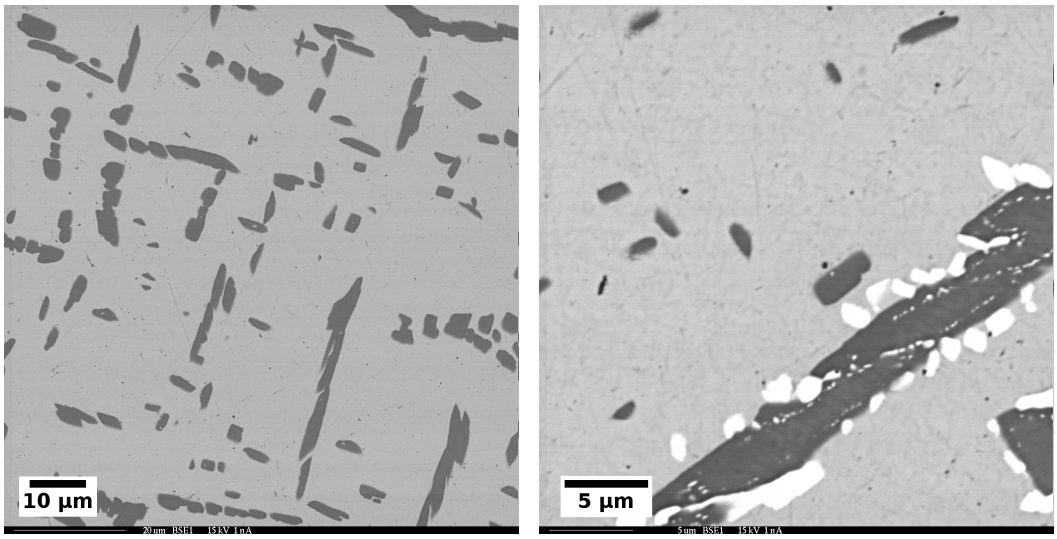

(a) As-cast alloy (b) Alloy quenched from γ phase

Fig. 4.74.: BSE images of U-50Zr alloys annealed for 30 days at 600^{o}C

BSE images of as-cast and quenched alloys annealed for 30 days are shown in Figures 4.74a and 4.74b. Zr precipitates (dark) along with α-U precipitates (white) are seen indicating the presence of oxygen during annealing. It is well known that δ phase is unstable in the presence of oxygen and nitrogen and decomposes into α-U and α-Zr [109, 115–117] and Figures 4.74a and 4.74b provide a direct evidence of it.

5. DISCUSSION

The meaning of the results presented in Chapter 4 will be discussed in the following Sections. There is a wealth of detail to consider, much of which is confirmatory to previous literature on the U-Zr binary system. On the other hand, the data also point to a potential error in understanding with regard to the δ phase transformation and how it may be more precise to consider the observed Zr-rich phases to be a sluggishly-metastable ω phase, under some conditions. To clarify these comments, the discussion will focus on the implications of the compiled data from the quenched and as-cast alloys (Section 5.1), the γ-annealed step-cooled alloys (Section 5.2), and the 600^{o}C ($\alpha + \delta$) annealed alloys (Section 5.3).

5.1 Quenched and As-cast Alloys

The microstructure in all quenched alloys must be the product of a diffusionless transformation since the cooling rate from the annealing temperature likely exceeds[1] 800^{o}C.s^{-1}. As pointed out in Section 2.2.4, the collapse of $\{111\}_\gamma$ planes and partial ordering of Zr atoms to form the δ phase is, in part,[2] a diffusion-controlled process that cannot occur in a quenching scenario. The athermal-ω transformation is a common feature in Zr alloys [94, 104, 127] and the cumulative data in Chapter 4 strongly suggests that it exists in the test U-Zr samples when quenched from the γ phase. Table 5.1 summarizes the alloy compositions and the conditions under which athermal-ω phase was observed.

[1] In this study, the alloys were homogenized at 850^{o}C and rapidly quenched into ice water. Though the quench rate not measured, the assumed rate of 800^{o}C/s is a reasonable first approximation.

[2] While collapse of $\{111\}_\gamma$ planes is a shear dominated, diffusionless transformation, ordering of Zr atoms is a thermally activated process and is diffusion-controlled.

Table 5.1: Ambient temperature phases in the alloys determined using XRD, TEM, EPMA, and DSC

Alloy Composition	Quenched	As-cast
U-2wt%Zr	$\alpha^{'} + \omega$	$\alpha + \delta$
U-5wt%Zr	$\alpha^{'} + \omega$	$\alpha + \delta$
U-10wt%Zr	$\alpha^{'} + \omega$	$\alpha + \delta$
U-20wt%Zr	$\alpha^{'} + \omega + \gamma$	$\alpha + \delta$
U-30wt%Zr	$\alpha^{'} + \omega + \gamma$	$\alpha + \delta$
U-50wt%Zr	$\omega + \gamma$	$\alpha + \delta$

Contrary to the scenario for quenched alloys, microstructures of as-cast alloys are a product of diffusional transformation since the cooling rate during the casting process was 40^{o}C/min, allowing more time for diffusion. Hence, the Zr-rich phase formed by the collapse of $\{111\}_{\gamma}$ planes has more time for partial ordering resulting in δ phase formation. Now, the following most important questions relevant to the present investigation merit elaboration.

1. *What is the formation mechanism of δ phase in U-rich U-Zr alloys*?

2. *What is the rationale behind the differentiaton between ω and δ in the literature and in the present study*?

The first question is addressed by considering the scenario where a U-Zr alloy (say, U-10Zr) is being cooled slowly at 40^{o}C/min from γ phase. During cooling, the alloy passes through various phase fields (i.e, $(\gamma_1 + \gamma_2)$, $(\beta + \gamma)$, and $(\alpha + \gamma)$). Also, $(\beta + \gamma)$ to $(\alpha + \gamma)$ is a eutectoid transformation and once the β is formed, very little diffusion is required for the α phase to form since α and β will have similar low Zr compositions. The eutectoid signature in terms of morphology (lamellar microstructure) is preserved while cooling and in the temperature range of 615 to

610^{o}C, the $\{111\}_\gamma$ planes in $(\alpha+\gamma)$ collapse (i.e., at the so called ω start temperature [94]) and the partial ordering takes place because of slow cooling and δ phase is formed. So, the δ phase, having the hexagonal structure forms via ω transformation mechanism. The δ formed from the γ (i.e, from the γ portion of the $(\alpha+\gamma)$ mixture) will inherit it's composition which is $\sim$40wt% or $\sim$63.50at% (inspection from the binary U-Zr phase diagram [119]).

The explanation presented above concurs with Lagerberg's experimental data on U-2Zr alloy [128]. He investigated phase transformations in U-2Zr, and constructed a TTT diagram. A DSC study was also conducted where in a transformation during heating the sample was observed at 610^{o}C ($\delta \rightleftharpoons \gamma$). However, the explanation given to this transformation (i.e, instead of $\delta \rightleftharpoons \gamma$) and also an apparent bend seen in TTT curve at 610^{o}C was that "a transition in growth mechanism from a diffusion to a shear process since the reaction rate is markedly increased below this temperature". But, as mentioned above and also in Sections 2.2.4 and 4.2.1, $\gamma \rightarrow \delta$ is a shear transformation. Moreover, the absence of literature on low temperature synthesis of δ phase (i.e, from α-U and α-Zr) bolsters the above explanation. Without confirmatory experimental evidence, it appears that the only way δ phase forms is via ω transformation mechanism along with partial ordering of Zr atoms.

Previous investigations on slow cooled (as-cast) U-rich U-Zr alloys have attributed the Zr-rich lamellae to supersaturated α-U since XRD only contained peaks α-U even though this phase was within it's detection limits [128–135]. It is also pointed out that even using Synchrotron radiation (National Synchrotron Light Source at Brookhaven National Laboratory), which has higher flux and energy of X-Rays, the presence of δ phase could not be ascertained [136]. However, TEM analysis on the U-2Zr, U-5Zr, and U-10Zr as-cast alloy samples (sectioned from the present batch of alloys cast) performed at Lawrence Livermore National Laboratory revealed that the lamellae are infact composed of δ phase [137, 138].

Within the context of the above proposed mechanism for δ phase formation, the absence of it's peaks in XRD data of as-cast U-rich U-Zr alloys can be explained if the collapse of the $\{111\}_\gamma$ planes and partial ordering is incomplete when slowly cooled from γ phase. Partial ordering at small spatial scales will not produce sharp X-ray peaks and this form of δ is analogous to *rumpled-ω/diffuse-ω* [94] (Refer to Section 2.2.4).

To address the next question on differentiating ω and δ, the work by Silcock [108], Boyko [107], and Akabori et al [109, 110] in determining the crystal structure of δ phase is mentioned here. Silcock observed the apparent similarity of δ with ω phase formation in Ti-V alloys [98] and found disagreement when indexing the observed pattern assuming (0,0,0) position for U atom, and Zr atom in ($\frac{2}{3}$, $\frac{1}{3}$, $\frac{1}{2}$) and ($\frac{1}{3}$, $\frac{2}{3}$, $\frac{1}{2}$) positions[3]. She then proposed special positions for Zr atoms in ω structure to obtain δ crystal structure (i.e, partially ordered ω). Accordingly, the Al position was assigned to Zr (i.e, (000)), and the B position was randomly assigned to U and Zr (i.e, at ($\frac{2}{3}$, $\frac{1}{3}$, $\frac{1}{2}$) and ($\frac{1}{3}$, $\frac{2}{3}$, $\frac{1}{2}$)).

Boyko [107] also used the same atomic positions used as Silcock [108] and found better agreement for δ phase structure when it is partially ordered. Akabori et al [110], using X-ray diffraction on a powdered δ phase sample, indexed the pattern by using two atomic configurations. In the first, they used Silcock's proposed atom positions [108] and in the second, they used completely random distributuion for U and Zr atoms at U/Zr=$\frac{1}{2}$. Little difference was observed between both configurations used. Akabori et al [109], using high resolution neutron diffraction, determined the same structure for δ phase. However, they also remarked that the partioning of U between Al and B positions has little effect in diffraction pattern as the atomic

[3]These positions were first proposed for Ti and U for the U_2Ti compound by Knapton [139]. He positioned Ti at (0,0,0), and U at ($\frac{2}{3}$, $\frac{1}{3}$, $\frac{1}{2}$) and ($\frac{1}{3}$, $\frac{2}{3}$, $\frac{1}{2}$) positions, thus producing the U_2Ti compound. Silcock interchanged the positions such that U occupied Ti position and Zr occupied U position thus producing UZr_2 compound [108]. However these positions did not produce the observed pattern.

scattering factor between U and Zr is not very different. So, this inherent abmiguity puts the 'partial ordering of Zr atoms'somewhat into question.

It is also pointed out that, for the ω phase occurring in Ti and Zr alloys, no preferential occupancy of Al and B positions by constituent atoms has been reported [94]. It still is not clear if the partial ordering of Zr atoms is necessary to obtain the XRD pattern for δ phase. Recall that the diffraction patterns observed for γ-quenched and as-cast alloys of U-20Zr, U-30Zr, and U-50Zr in this study (Sections 4.4, 4.5, and 4.6) had the athermal-ω and as-cast δ lines at the same 2θ positions potentially suggesting that the supposed ordering of Zr atoms (ordering in as-cast alloys is the result of diffusional transformation) in as-cast alloys has not manifested as a perceivable difference between the respective patterns (i.e, between ω and δ). In other words, the diffraction patters for athermal-ω and the δ phase are identical and cannot be used to discern the difference between the two phases.

Literature on the formation of ω phase in U-Zr alloys is rather sparse, with only two investigations providing experimental data [48, 129]. Hatt [48] reported the occurrence of ω phase in a quenched U-50at%Zr (U-27.7wt%Zr) alloy. However, no other details on morphology and X-ray diffraction pattern were presented. Hills et al [129], in their study on U-Zr alloys using Jominy test[4], reported the formation of ω phase in the following alloys:

1. Slow cooled end of U-14.1wt%Zr alloy
2. Slow cooled end of U-20.3wt%Zr alloy
3. Quenched and slow cooled ends of U-27.7wt%Zr alloy

However, no X-ray diffraction patterns were shown from their investigation. Had a difference in the XRD patterns in slow cooled and quenched ends been observed in

[4]The Jominy test consists of annealing a specimen which is usually cylindrical in shape at high temperature and immersing only the tip of specimen in a quenching medium. This way, different cooling rates, from rapid quench in the tip, to slow cooling at the other end are obtained along the length of the specimen.

their investigation, it seems that it would have been pointed out, but it appears that it was not the case. Formation of ω in the quenched tip of U-27.7Zr is consistent with athermal-ω formation (as noted in Sections 4.4, 4.5, and 4.6) and the results from present investigation are in perfect accord with their data. However, in the slow cooled ends, phase transformations must be diffusion controlled which should facilitate the ordering process and δ phase should be formed. Since the presence of ω phase was claimed in their study in two extreme scenarios (i.e, for quenched and slow cooled regions), it appears that there are extremely subtle differences in diffraction patterns for ω and δ in U-Zr alloys which could not be resolved by conventional XRD technique.

In the present study, the only difference observed in the XRD patterns of quenched and as-cast alloys was that the 2θ peaks at 20.4^o, 28.9^o, 46.6^o, and 71.8^o were somewhat broad for γ-quenched alloys compared to as-cast alloys (Refer to the Figures 4.49, 4.51, 4.62, 4.63, 4.69, and 4.70 for as-cast and quenched U-20Zr, U-30Zr, and U-50Zr alloys respectively). Broad XRD peaks are a characteristic feature of athermal-ω phase and indicates incomplete collapse of $\{111\}_\gamma$ planes [94]. Upon slow cooling or annealing in $(\alpha + \delta)$ phase field, peaks at the above 2θ positions become relatively sharp after a complete collapse of $\{111\}_\gamma$ planes. This infact has been observed in the present study (In step-cooled U-10Zr alloy. Refer Figure 4.39) and by Basak in U-7Zr and U-35Zr alloys, after step-annealing them (from $\gamma \rightarrow (\beta+\gamma) \rightarrow (\alpha+\gamma) \rightarrow (\alpha+\delta)$) for several thousands of hours [131].

Based on above comments and the cumulative data from the present study, it is suggested that it might be more appropriate to designate the observed Zr-rich phases in quenched and as-cast alloys as athermal-ω (ω_{ath}) and diffusional-ω (ω_d), respectively. Such a classification[5] (i.e, as ω_{ath} and ω_d) describes the data in the present study more elegantly compared to the case where they are considerd as

[5]In this Chapter, the usage of δ in the as-cast alloys will be maintained following the nomenclature in the established U-Zr phase diagram. However the suggestion is made towards considering the presence of ω_d instead of δ in as-cast alloys whenever evidence points to it.

ω and δ. Results for γ-quenched, as-cast, step-cooled and annealed, and $(\alpha + \delta)$ annealed alloys from the present study are further discussed considering the above ideas. Using complementary data, it will be shown that ω_{ath} phase forms profusely in all alloys when quenched from γ phase and ω_d phase forms in all as-cast alloys.

When quenched from γ phase, U-50Zr undergoes the athermal-ω transformation as evidenced from the peaks of ω along with retianed γ in XRD pattern (Figure 4.70). The as-cast alloy on the other hand contains peaks for α-U besides those for $\delta(\omega_d)$ phase (Figure 4.69). Since the as-cast alloy was slowly cooled from γ phase at 40^oC/min, there was enough time for diffusion and is referred to as $\delta(\omega_d)$. The DSC curve for the quenched alloy (Figure 4.71) shows a single transformation at 601.5^oC and from XRD pattern, it is seen that the room temperature phases are ω and γ, so, the transformation occuring at 601.5^oC during heating corresponds to $\omega \rightarrow \gamma$ transformation. In the case of as-cast alloy, the $\delta(\omega_d) \rightarrow \gamma$ transformation occurs at 618^oC. It is seen that the transformation temperature was lowered from 618^oC to 601.5^oC when the alloy was quenched from γ phase.

For γ-quenched U-30Zr and U-20Zr alloys, XRD patterns (Figures 4.63 and 4.51) indicate the presence of both $\alpha^{'}$ and ω. In the XRD data of quenched U-30Zr alloy, the $(002)_\alpha$ line has completely overlapped with $(021)_\alpha$ line while the $(110)_\alpha$ line is seen just as a faint shoulder peak to $(021)_\alpha$ line. The XRD pattern for quenched U-20Zr alloy is similar to U-30Zr except that the overlapping is less pronounced. This could also indicate the first sign of γ phase retention, though it is not conclusive. Optical micrograph of the γ-quenched U-20Zr alloy (Figure 4.50) showed only γ grain boundaries indicating that the transformation path was $\gamma \rightarrow \alpha^{'}$ without β as intermediate state. For the $\gamma \rightarrow \beta \rightarrow \alpha^{'}$ transformation, the microstructure would be irregular [50, 69]. Formation of ω phase must be within the prior γ grains, which could not be resolved using optical microscope.

The DSC curves for U-30Zr and U-20Zr alloy samples quenched from γ phase (part (a) of Figures 4.64 and 4.52) show two transformations, first one at 600^oC

and 596^{o}C and second transformation at 699^{o}C and 698^{o}C respectively. From XRD patterns, the room temperature phases present were $\alpha^{'}$ and ω, and from the DSC data of γ-quenched U-50Zr, the transformation occuring at $\sim 600^o$C is $\omega \rightarrow \gamma$. So, by extension, the transformation occuring at $\sim 600^o$C in both alloys can be regarded as $\omega \rightarrow \gamma$. The transformation at $\sim 700^o$C is the final transformation to γ phase in both cases since no transformation occured beyond this point. Since there was no $\alpha \rightarrow \beta$ transformation, this can be regarded as a direct $\alpha^{'} \rightarrow \gamma$ transformation.

For the as-cast alloys, the microstructures for U-30Zr and U-20Zr consisted of $\delta(\omega_d)$ phase matrix with α lamellae (Figures 4.61a, 4.61b and 4.47, 4.48a respectively). Though WDS analysis on as-cast samples couldn't be performed owing to very small features that were unresolvable in the microprobe, the presence of $\delta(\omega_d)$ phase was ascertained from XRD and DSC data. Peaks for $\delta(\omega_d)$ phase in XRD are clearly evident in both alloys (Figures 4.62 and 4.49) while DSC curves (Part (b) of Figures 4.64 and 4.52) of as-cast U-30Zr and U-20Zr alloys show a clear transformation peak at 621.5^{o}C and 618^{o}C respectively, in accord with the $\delta(\omega_d) \rightarrow \gamma$ transformation temperature shown (at 617^{o}C) in the equilibrium phase diagram [119].

Both γ-quenched and as-cast alloys of U-10Zr and U-5Zr exhibited identical features in their data. XRD data for both alloys quenched from γ phase consisted of peaks of only α-U (Figures 4.35 and 4.19). For U-10Zr, there was a visible overlapping of $(021)_\alpha$ and $(002)_\alpha$ lines while there was neither overlapping nor splitting of α-U peaks in the case of U-5Zr XRD data. No peaks for ω phase were found in XRD data in either of the quenched alloys. Optical micrographs in both cases (Figures 4.33b and 4.17b) clearly showed remnant γ grain boundaries indicating a direct $\gamma \rightarrow \alpha^{'}$ transformation without β as intermediate state. Back scattered images of quenched alloys showed bright (Zr rich) islands, likely evidence of the presence of ω phase (Figures 4.33a and 4.17a).

It is using bright field TEM images (Figures 4.34a and 4.18a) that a clear two phase lath morphology of alternating $\alpha^{'}$ and ω obtained. It is known that athermal ω

has ellipsoidal morphology with particles aligned along <111> direction of the parent b.c.c phase [125]. However, plate like morphology of ω phase has been observed in shock loaded Zr and it's alloys [96,126]. Moreover, the formation mechanisms of both $\alpha^{'}$ and ω from the parent b.c.c γ phase (Refer to Sections 2.2.1 and 2.2.4) explain the alternating bands. Additional indication for the presence of ω phase was obtained from DSC curves of γ-quenched U-10Zr and U-5Zr alloys.

The DSC curves for γ-quenched U-10Zr and U-5Zr, shown in Figures 4.36 and 4.20 had two transformations while heating. One at 601^{o}C and the other at $\sim 700^{o}$C. The first transformation occured at almost same temperature i.e, at $\sim 600^{o}C$ which corresponds to $\omega \rightarrow \gamma$ transformation in U-50Zr, U-30Zr, and U-20Zr. All these alloys had this transformation occuring at $\sim 600^{o}$C and it appears to be compositional invariant. The fact that $\omega \rightarrow \gamma$ heating transformation occurs at $\sim 600^{o}$C for all quenched alloys while the $\delta(\omega_d) \rightarrow \gamma$ transformation at $\sim 617^{o}$C for as-cast alloys, is a direct consequence of cooling rate from γ phase. Metastable phases formed in γ-quenched alloys (i.e, ω and $\alpha^{'}$) transform at different temperatures compared to the transformation temperatures of equilibrium phases. Transformation of $\delta(\omega_d) \rightarrow \gamma$ at $\sim 617^{o}$C for as-cast alloys is in excellent agreement with the U-Zr binary phase diagram [119].

For the as-cast U-10Zr and U-5Zr alloys, BSE images show lamellar microstructure (Figures 4.30a and 4.15a) with lamellae rich in Zr and the matrix rich in α-U. WDS analysis could not be performed as the lamellae were too small for the electron microprobe. Optical imaging in the case of U-5Zr showed a fleck type microstructure (Figure 4.15b) while for U-10Zr lamellae were clearly seen (Figures 4.30b and 4.31). DSC curves for the as-cast alloys (Part b) of Figures 4.36 and 4.20) showed a clear transformation at $\sim 617^{o}$C which is the $\delta(\omega_d) \rightarrow \gamma$ transformation according to the phase diagram [119] thus indicating that the Zr-rich phase is $\delta(\omega_d)$. Moreover, TEM analysis on these alloys has confirmed that it is $\delta(\omega_d)$ phase [137, 138].

XRD patterns for both the as-cast alloys on the other hand showed peaks for only α-U (Figures 4.32 and 4.16) though the area fraction of the Zr-rich lamellae was within the detection limits of XRD technique. The inability of XRD to detect this phase is well documented in literature and as mentioned previously, the $\delta(\omega_d)$ phase has been attributed to supersaturated α-U by several investigators [128–135]. However, considering the ideas mentioned on the formation mechanism of δ phase, the lack of XRD peaks can be explained by considering the Zr-rich phase as ω_d instead of δ.

For U-2Zr alloy, the γ-quenched microstructure was different from other quenched alloys in that the optical micrograph consisted of martensitic plates (Figure 4.3b). No structure within the plates (internal twinning or slip planes) could be resolved. The microstructure is similar to the one reported in literature [134] and has acicular morphology for the martensitic alpha ($\alpha_a^{'}$). Back scattered image had bright and dark areas, an indication of Zr-segregation (Figure 4.3a). The DSC curve for γ-quenched U-2Zr alloy was different than for other quenched alloys (Figure 4.5). A clear, yet small transformation peak is seen at 587^oC, lower to the ones observed for other alloys (i.e, at $\sim 600^o$C). By extending the trend observed in other alloys, it is proposed that ω phase is formed in quenched U-2Zr alloy and that the transformation observed at 587^oC corresponds to $\omega \rightarrow \gamma$. This proposal is in constrat to the one suggested by Basak et al [134] in which a transformation observed at 589^oC in a quenched U-2Zr alloy in their study, was identified as $\alpha_a^{'} \rightarrow \alpha$ [134]. The XRD pattern for γ-quenched U-2Zr alloy (Figure 4.4) had peaks for only α-U similar to the XRD data of quenched U-5Zr and U-10Zr alloys.

The as-cast U-2Zr alloy had lamellar microstructure in back scattered mode (Figure 4.1a) and a fleck type microstructure in optical micrograph (Figure 4.1b). XRD pattern for as-cast U-2Zr alloy (Figure 4.2) had peaks for α-U similar to the data of as-cast U-5Zr and U-10Zr alloys. The DSC curve for as-cast alloy (Figure 4.5) indicates 5 transformations with most of them overlapping with each other, indicat-

ing sluggish transformation kinetics. Presence of $\delta(\omega_d)$ phase in as-cast U-2Zr alloy was confirmed by TEM analysis [138] at Lawrence Livermore National Laboratory which suggests that the transformation at 608^oC in DSC data from present study corresponds to $\delta(\omega_d) \rightarrow \gamma$.

The transformation temperatures from DSC heating curves which correspond to $\delta(\omega_d) \rightarrow \gamma$ and $\omega \rightarrow \gamma$ for as-cast and quenched alloys respectively, are shown in Table 5.2. A clear lowering of transformation temperature (i.e, from $\sim 617^oC$ to $\sim 600^oC$ and 608^oC to 587^oC) is seen when the alloys are quenched. Moreover, the difference in the transformation temperatures (i.e, ΔT) between the two transformations is seen to be more or less constant within the experimental error of the DSC technique. The near invariance of ΔT in the alloys once again strongly suggests the presence of ω in γ-quenched U-2Zr alloy. The transformation at 587^oC in this γ quenched alloy, by extension, is $\omega \rightarrow \gamma$ as opposed to $\alpha_a^{'} \rightarrow \alpha$, suggested by Basak et al [134][6].

Table 5.2: $\delta(\omega_d) \rightarrow \gamma$ and $\omega \rightarrow \gamma$ transformation temperatures from DSC curves during heating for as-cast and the alloys quenched from γ phase

Alloy Composition	As-cast (^oC)	γ-quenched (^oC)	ΔT (^oC)
U-2wt%Zr	608	587	21
U-5wt%Zr	616	601	15
U-10wt%Zr	617.5	601	16.5
U-20wt%Zr	618	596	22
U-30wt%Zr	621.5	600	21.5
U-50wt%Zr	618	601.5	16.5

From X-ray diffraction data from quenched alloys, there is a clear indication of α-U like characteristics in U-rich alloys, and a progression towards γ and ω like

[6]Understandably, it is rather difficult to interpret the transformation at 589^oC to $\omega \rightarrow \gamma$ when they studied the alloy 'stand-alone'. However, in the present investigation, a whole suite of alloys were analyzed making it easier to extend the trend to U-2Zr alloy.

characteristics with increasing Zr content in the alloys. It is seen as overlapping of certain α-U peaks and retention of γ and ω in U-50Zr. Figure 5.1 shows such a sequence as a function of Zr content in the alloy. For U-50Zr alloy, only $(101\bar{1})$ peak for ω phase is seen while for U-30Zr, $(110)_\alpha$ is almost absent while $(002)_\alpha$ is seen as a faint shoulder peak on $(021)_\alpha$. For U-20Zr, the overlapping of $(021)_\alpha$ and $(002)_\alpha$ is less pronounced while $(110)_\alpha$ is still seen. For U-10Zr, $(110)_\alpha$, and $(021)_\alpha$ are distinct, with $(002)_\alpha$ just starting to merge into $(021)_\alpha$. U-5Zr and U-2Zr have distinct peaks without any overlap.

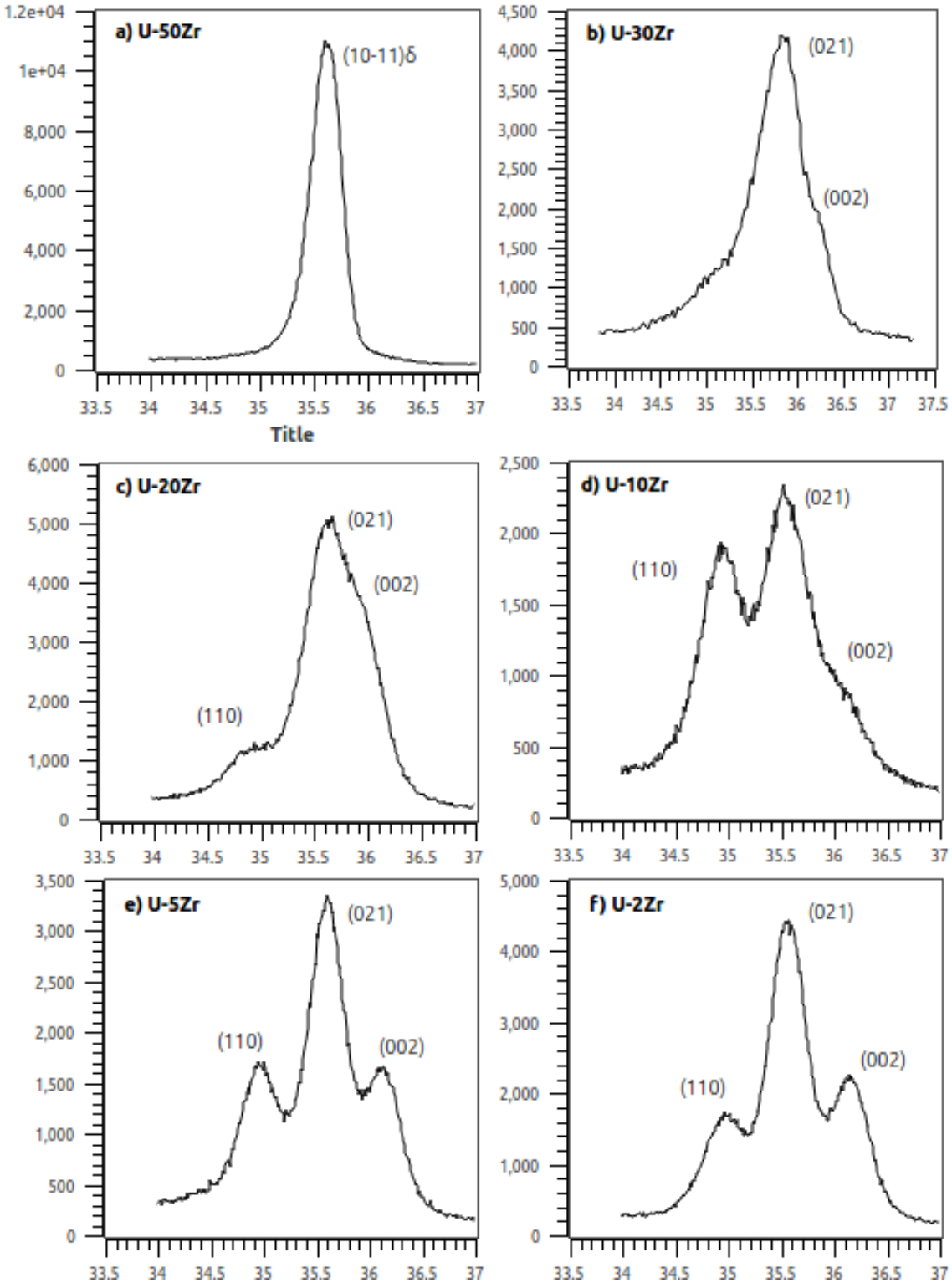

Fig. 5.1.: XRD patterns of γ-quenched alloys (partial 2θ range)

5.1.1 Phase Transformation Sequence in γ-Quenched Alloys

Based on the results and analyses on the γ-quenched alloys, an attempt is made to address an interesting question: *What is/are the likely transformation paths for high temperature γ phase when rapidly quenched*? This, to some extent, can be gleaned from the available data and also reasoned by logic and the starting point for this is the knowledge about retained phases. Table 5.1 shows the ambient temperature phases present in both quenched and as-cast alloy samples. In all quenched alloys, the phases present are $\alpha^{'}$, ω, and possibly, some retained γ. The presence of $\alpha^{''}$ in the alloys was ruled out as there was no splitting of the α-U lines in any of the measured patterns (Refer Section 2.2.1).

The γ-quenched U-50Zr alloy undergoes only one transformation when quenched i.e from $\gamma \rightarrow \omega$. The reverse transformation from $\omega \rightarrow \gamma$ occurs at 601.5^{o}C. For γ-quenched U-30Zr, U-20Zr, U-10Zr, and U-5Zr alloys, only two transformations are seen in the heating curves in the DSC data and it is suggested here that their transformation sequence must be similar. Basis for this suggestion is the strikingly close proximity of the two transformation temperatures in these alloys, as previously described. This is clearly seen from Table 5.3. For all the alloys, the first transformation occurs at $\sim 600^o$C and the second at $\sim 700^o$C.

The following two schemes for martensitic transformation when quenching γ phase are hence possible for U-5Zr, U-10Zr, U-20Zr, and U-30Zr alloys[7]. In the first scheme, γ partially shears to $\alpha^{'}$, and the remnant γ then transforms to ω via collapse of $\{111\}_\gamma$ planes, represented[8] as $\gamma \stackrel{s}{\Rightarrow} (\alpha^{'}, \omega)$. Partial transformation of γ leads to the retention of both $\alpha^{'}$ and ω at room temperature. It is quite possible that even these transformations are incomplete and some γ could be stabilized at room

[7]These are based on the schemes proposed by Hills et al [129]. However, they never observed ω phase in quenched alloys containing Zr up to ∼20wt%. Presence of athermal-ω was identified only in quenched tip of U-27.7wt%Zr alloy.

[8]Shear transformation is represented as $\stackrel{s}{\rightarrow}$ and partial shear transformations from $\gamma \stackrel{s}{\rightarrow} \alpha^{'}$ and $\gamma \stackrel{s}{\rightarrow} \omega$ are indicated as $\gamma \stackrel{s}{\Rightarrow} (\alpha^{'}, \omega)$.

Table 5.3: Transformation temperatures from DSC curves during heating for the alloys quenched from γ phase

Alloy Composition	First transformation (^{o})C ($\omega \rightarrow \gamma$)	Second transformation (^{o})C ($\alpha^{'} \rightarrow \gamma$)
U-2wt%Zr	587	688
U-5wt%Zr	601	700
U-10wt%Zr	601	701
U-20wt%Zr	596	698
U-30wt%Zr	600	699
U-50wt%Zr	601.5	-

temperature. However detecting it is difficult as the X-ray diffraction peaks of the b.c.c γ phase overlap with those of α-uranium.

In the second scheme, γ transforms to ω which then partially shears to $\alpha^{'}$, resulting in the rentention of both ω and $\alpha^{'}$. However $\omega \xrightarrow{s} \alpha^{'}$ was deemed problematic by Hills et al [129] citing Hatt and Robert's work [105] who have shown that $\gamma \xrightarrow{s} \omega$ shear transformation in U-Zr alloys is accomplished by atom movements on same planes and directions as the $\gamma \xrightarrow{s} \alpha^{'}$ shear transformation, the only difference being the sense of atom movements. It then follows that $\omega \xrightarrow{s} \alpha^{'}$ following $\gamma \xrightarrow{s} \omega$ must be just the completion of $\gamma \xrightarrow{s} \alpha^{'}$. However, the possibility of a geometrically different transformation for $\omega \xrightarrow{s} \alpha^{'}$ was not ruled out and in such a scenario, the possibility of occurrence of $\gamma \rightarrow \omega \xrightarrow{s} \alpha^{'}$ still exists.

In order to specifically detect the sequence of transformation, a quenching dilatometry experiment needs to be performed. The two possible transformation schemes for quenched alloys considered are shown in Table 5.4. As the microstructure of γ-quenched U-2Zr alloy is markedly different than others and since the DSC curve has more than two transformations taking place, a similar argument has not been

extended. It must however be noted that Basak et al [134], in their quenching dilatometry[9] study on U-2Zr alloy have found two thermal arrests, one at 597^{o}C and another at 553^{o}C. A double transformation mechanism has been proposed where γ first shears to $\alpha^{''}$, which then shears to $\alpha_a^{'}$. So, for U-2Zr alloy, the transformation sequence proposed by them was [134]: $\gamma \xrightarrow{s} \alpha^{''} \xrightarrow{s} \alpha^{'}$.

Table 5.4: Possible transformation schemes upon quenching from γ phase

Alloy Composition	Scheme I	Scheme II
U-5wt%Zr	$\gamma \overset{s}{\Rightarrow} (\alpha^{'}, \omega)$	$\gamma \xrightarrow{s} \omega \xrightarrow{s} \alpha^{'}$
U-10wt%Zr	$\gamma \overset{s}{\Rightarrow} (\alpha^{'}, \omega)$	$\gamma \xrightarrow{s} \omega \xrightarrow{s} \alpha^{'}$
U-20wt%Zr	$\gamma \overset{s}{\Rightarrow} (\alpha^{'}, \omega)$	$\gamma \xrightarrow{s} \omega \xrightarrow{s} \alpha^{'}$
U-30wt%Zr	$\gamma \overset{s}{\Rightarrow} (\alpha^{'}, \omega)$	$\gamma \xrightarrow{s} \omega \xrightarrow{s} \alpha^{'}$
U-50wt%Zr	$\gamma \xrightarrow{s} \omega$	-

However, based on Hatt's model [48] for formation of α like metastable phases (Refer to Section 2.2), $\alpha^{''}$ is the monoclinic distortion of $\alpha^{'}$ and forms if $\hat{\gamma}$ angle fails to reach 90^o. For the $\alpha^{''} \xrightarrow{s} \alpha^{'}$ transition, there should in principle be a smooth change in $\hat{\gamma}$ angle as $\alpha^{''} \xrightarrow{s} \alpha^{'}$ is just the completion of $\gamma \xrightarrow{s} \alpha^{'}$ shear transformation ($\alpha^{''}$ represents under-shear with respect to $\alpha^{'}$). An abrupt change in the dilatometer signal (i.e, second thermal arrest) seen indicates atomic rearrangement of some form and hence a change in crystal structure. Following the assumption that $\omega \xrightarrow{s} \alpha^{'}$ must be just the completion of $\gamma \xrightarrow{s} \alpha^{'}$ [129], Basak et al ruled out ω as intermediate phase and from calculations of relative change in length obtained from dilatometer signal, the possbility of γ^o was ruled out. On the other hand, a transformation at 589^{o}C in their DSC heating curve strongly suggests that it is $\omega \rightarrow \gamma$ as has been observed in the findings of present study. If such is the case, the transformation schemes suggested for other quenched alloys (Table 5.4) can be extended to γ-quenched U-2Zr as well.

[9]The cooling rate used in their investigation was 175^{o}C.s^{-1}.

Hatt [48], in his work, studied quenched U-10at%Zr (∼U-4wt%Zr) alloy and found that the microstructure consisted two families of bands intersecting each other, a possible signature of double transformation. He conjectured that γ^o existed in a small temperature range as an unpublished work by G. B. Brook and E. H. Welch[10] indicated only a single thermal arrest in their analyis on martensitic transformations in U-10at%Zr alloys. So, according to Hatt [48], the scheme could be $\gamma \xrightarrow{s} \gamma^o \xrightarrow{s} \alpha^{'}$ as was observed in U-Mo alloys [61] and U-Nb alloys [53, 54, 58, 140]. The schemes $\gamma \xrightarrow{s} \gamma^o \xrightarrow{s} \alpha^{''}$ and $\gamma \xrightarrow{s} \gamma^o \xrightarrow{s} \alpha^{'}$ are well established transformation schemes observed in U-Nb alloys with $\alpha^{'}$ forming at lower Nb contents and $\alpha^{''}$ forming at higher Nb contents. In the former case, there is not enough Nb content to produce monoclinic distortion [53, 54, 58, 140]. In recent investigation on U-5at%Nb alloy [140], quenching dilatometry indicated two thermal arrests and the room temperature microstructure consisted of both $\alpha_a^{'}$ and $\alpha_b^{'}$. It was believed that the double signal from the dilatometer was associated with the acicular and banded martensites (i.e, $\alpha_a^{'}$ and $\alpha_b^{'}$) forming at different temperatures.

With the gammatizing temperature (850^{o}C) and the quenching mechanism (i.e, quench rate) used in this study, neither γ^o nor $\alpha^{''}$ could be observed as room temperature phases. With the presence of ω phase and $\alpha^{'}$ phase in all the γ-quenched alloys, it is possible that these phases form at different temperatures[11] during quenching and either of the suggested transformation sequences could be operational (Refer Table 5.4). However, considering the formation of various metastable phases in uranium alloys, and with the additional complexity of the formation of metastable ω phase, which is unique to U-Zr alloys, further work using TEM and quenching dilatometry is necessary to confirm the actual sequence for each alloy.

[10]Their work was cited in [48]

[11]These temperatures most likely depend on the alloy composition and quench rate

5.2 Step-Cooled Alloys

Alloys were step cooled from γ phase with two thermal profiles as noted in Chapter 4. In the first case, alloy samples were homogenized in γ phase for 6 hours and step-cooled to 650^{o}C in $(\alpha + \gamma)$ phase field, held for 2 days and then quenched. This heat treatment was used to retain the $(\alpha + \gamma)$ microstructure at room temperature and study the morphology as a function of Zr content in the alloys. In the second case, U-2Zr, U-5Zr, and U-10Zr alloys were homogenized at 850^{o}C for 6 hours, step-cooled to 650^{o}C (i.e, in the $(\alpha + \gamma)$ phase field), held for 2 days, step cooled to 600^{o}C (i.e, in the $(\alpha + \delta)$ phase field), and held for 3 days, and then furnace cooled. This profile was used for U-rich U-Zr alloys to see if δ can be detected in XRD data in as-cast alloys. It is again mentioned here that as-cast alloys of U-2Zr, U-5Zr, and U-10Zr never showed δ phase peaks in XRD data even though this phase was shown to be present using TEM [137, 138]. The presence of ω_d instead of δ explains lack of the corresponding peaks (Refer Section 5.1) and would appear once the $\{111\}_\gamma$ plane collapse mechanism is complete upon holding at 600^{o}C.

5.2.1 Alloys Quenched from $(\alpha + \gamma)$ Phase Field

Alloy samples of U-2Zr, U-5Zr, U-10Zr, U-20Zr, and U-30Zr quenched from $(\alpha+\gamma)$ phase field, BSE images showed a two phase microstructure (Figures 4.6b, 4.21b, 4.37b, 4.53b, and 4.65b). The chemical composition of the matrix and the precipitates performed where feasible were consistent with they being α and γ phase respectively (The matrix phase for U-30Zr was γ and the precipitates were α-U). Since peaks for γ phase overlap with those with α-U, the presence of γ phase could not be stated conclusively (Figures 4.8, 4.23, 4.40, 4.54, and 4.66) from XRD data. While coincidence of peaks of α and γ-U cannot be an evidence for the presence of γ phase, it does not eliminate the possibility of it's presence either.

5.2.2 Alloys Step-Cooled to $(\alpha + \delta)$ and Annealed

As was observed in U-2Zr, U-5Zr, and U-10Zr as-cast alloys, XRD could not detect the presence of δ phase though DSC and TEM confirmed it's presence. While it is possible that for U-2Zr, the volume fraction of δ phase is below the detection limits of XRD, the same is not true for as-cast U-5Zr and U-10Zr alloys. Since the lamellar features were in the sub micron range (Figures: 4.30a and 4.15a), the alloys were held at 600^{o}C, in $(\alpha + \delta)$ phase field for 3 days while cooling from γ phase for the features to coarsen. Before holding at this temperature, the alloys were annealed at 650^{o}C in $(\alpha + \gamma)$ for 2 days and then step cooled to 600^{o}C, held for 3 days and then slowly cooled to room temperature. The microstructures are shown in Figures 4.6a, 4.21a, and 4.37a along with their WDS analyses in Tables 4.1, 4.3, and 4.5 indicating the Zr-rich phase to have the proper composition corresponding to the δ phase.

Interestingly, the XRD pattern for U-10Zr had broad peaks at same 2θ positions as athermal-ω for δ phase (Figure 4.39), indicating a lack of long range order. It appears that the collapse mechanism for δ phase formation is not yet complete and time needed might be more albeit the annealing was done at 600^{o}C for 3 days. XRD pattern for U-5Zr was similar in that the δ phase peak broadening was even more pronounced (Figure 4.22). Peaks for δ phase were non-existent in U-2Zr. As there were visible δ phase peaks in XRD patterns for as-cast U-20Zr and U-30Zr alloys, they were not subjected to this thermal profile. These expermients indicate that more time is needed for the formation of δ phase in U-rich U-Zr alloys upto 10wt% Zr studied here. Lack of complete collapse of $\{111\}_\gamma$ planes after 3 days of annealing is again an indication of ω_d instead of δ. Further, this implies that all δ phases observed in the as-cast alloys (furnace cooling over a few hours) are actually ω_d. The as-cast and quenched alloys with all Zr compositions were hence subjected to further annealing at 600^{o}C for up to 30 days.

5.3 Annealed Alloys

Both as-cast and quenched alloys were annealed at 600^{o}C (i.e, in the ($\alpha+\delta$) phase field) for 1, 3, 7, and 30 days for them to reach equilibrium comditions. While a two phase microstructure with the constituents having α-U and δ composition is seen in all alloys (except U-50Zr, as it consists of only δ phase) four most striking features were observed:

- X-ray diffraction patterns never showed peaks for δ phase in U-2Zr, U-5Zr, and U-10Zr as-cast and quenched alloys which were annealed for 7 and 30 days.

- The clear and sharp $\delta(\omega_d)$ phase peaks which were already present in as-cast U-20Zr alloy, and the ω phase peaks present in γ-quenched U-20Zr alloy (Figures 4.49 and 4.51) were no longer present on annealing.

- Broad peaks for δ phase were observed in step-cooled U-10Zr alloy sample annealed for 3 days at 600^{o}C (Figure 4.39) and not in any of the other annealed U-10Zr alloy samples[12].

- Reitveld analysis on annealed samples of U-5Zr and U-10Zr alloys has revealed the presence of γ phase instead of δ (Figures shown and doscussed below).

The above startling observations will be discussed in the light of the suggestion made in Section 5.1 regarding the presence of ω_d instead of δ in as-cast U-Zr alloys.

From the microstructures of annealed samples of U-2Zr, U-5Zr, and U-10Zr, and also from the WDS analysis of the individual phases present, it is apparent that the matrix has the composition consistent with α-U while the Zr-rich phase has the composition corresponding to δ phase. Moreover, the volume fractions of Zr-rich phase present are in the detectable range of XRD technique (This is true for U-5Zr and U-10Zr alloys which have apparent δ phase volume fractions of $\sim$12% and $\sim$25%,

[12]'Step-cooled' annealing is the thermal profile where the sample was cooled from γ phase and annealed at 600^{o}C. On the other hand, other samples were annealed by ascending to 600^{o}C from room temperature.

respectively). The amount of Zr in the Zr-rich lamellae of as-cast alloys was obtained from EDS analysis on a TEM and was ∼66at% (∼44wt%) [137, 138].

So, it is clear that this phase has inherited the amount of Zr from the γ in $(\alpha+\gamma)$ phase field. The only effect of annealing should then be to coarsen these lamellae keeping the composition intact and this is what was observed from WDS analysis in annealed samples. In addition, no precipitates or no increase in the number of α-Zr precipitates as a function of annealing time was observed in any of the alloys (U-2Zr to U-30Zr) indicating that the absence of δ phase peaks is not at all impurity driven. On the other hand, the absence of δ peaks can only be explained if the metastable ω_d is present in as-cast alloys. If this is indeed the case, then the following proposed transformation sequence must occur. During casting, due to slow cooling, metastable diffusional-ω (i.e, ω_d from the γ portion of $(\alpha+\gamma)$) forms due to the incomplete $\{111\}_\gamma$ plane collapse mechanism. If δ were the stable phase, it should be clearly revealed in XRD after annealing and the fact that it has not, adds to the credibility of ω_d. Moreover, the δ phase peaks present in as-cast U-20Zr alloy and the ω phase peaks present in γ-quenched U-20Zr alloy disappeared after annealing for 7 and 30 days. Reitveld analysis[13] of the 7 day and 30 day annealed samples at 600^oC of U-5Zr and U-10Zr alloys indicated the presence of γ phase in these alloys. It is seen clearly that the amount of γ phase present in the samples is increasing as a function of annealing time. This trend is shown in Table 5.5.

[13]The analysis was kindly performed by Dr. Thomas Hartmann at UNLV. He commented that presence of γ is possible yet somehow questionable as (002) peak b.c.c-Zr (b.c.c-Zr is shown as β-Zr in the figures) was not observed as the shoulder peak of $(112)_\alpha$. Yet other peaks of b.c.c-Zr were seen to contribute significantly to individual line intensities.

Table 5.5: Amount of γ phase present in as-cast U-5Zr and U-10Zr alloys as a function of annealing time

Alloy Composition	Annealing time at 600^{o}C	Phase fraction (%)
U-5Zr	7 days	9.54
U-5Zr	30 days	16.74
U-10Zr	7 days	4.30
U-10Zr	30 days	5.96

Figures 5.2, 5.3, 5.4, and 5.5 show the results of Reitveld analysis of annealed alloys of U-5Zr and U-10Zr, respectively. It must be pointed out that no internal standard was used and the XRD data were collected from a bulk sample. The presence of γ phase indicates two possibilities:

- That δ is unstable at 600^{o}C and the $(\alpha + \gamma)$ phase field extends below 600^{o}C
- That metastable ω_d is present in as-cast alloys instead of δ and transforms to γ upon annealing

These two possibilities will be discussed by considering the data from step-cooled and annealed U-10Zr alloy sample.

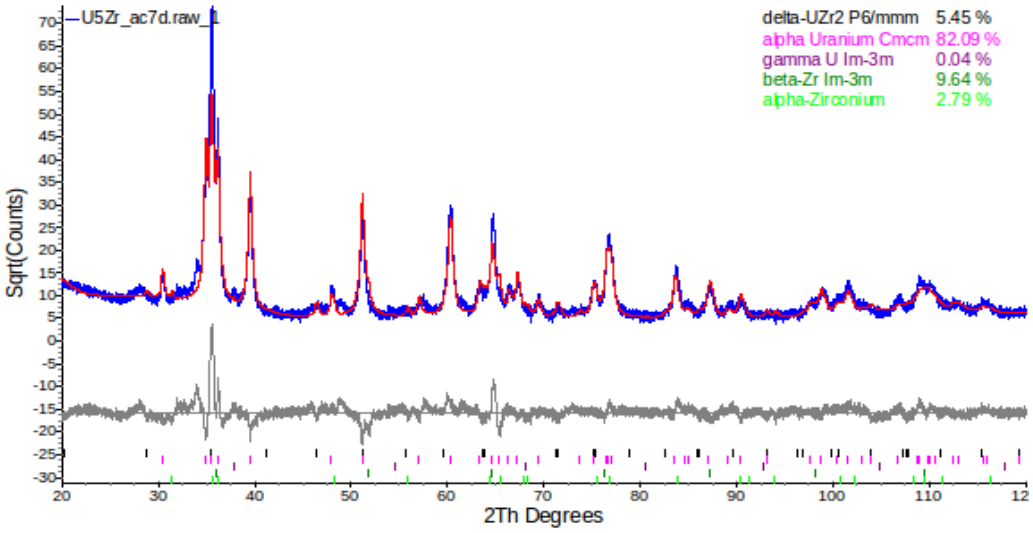

Fig. 5.2.: XRD pattern of as-cast U-5Zr alloy annealed for 7 days

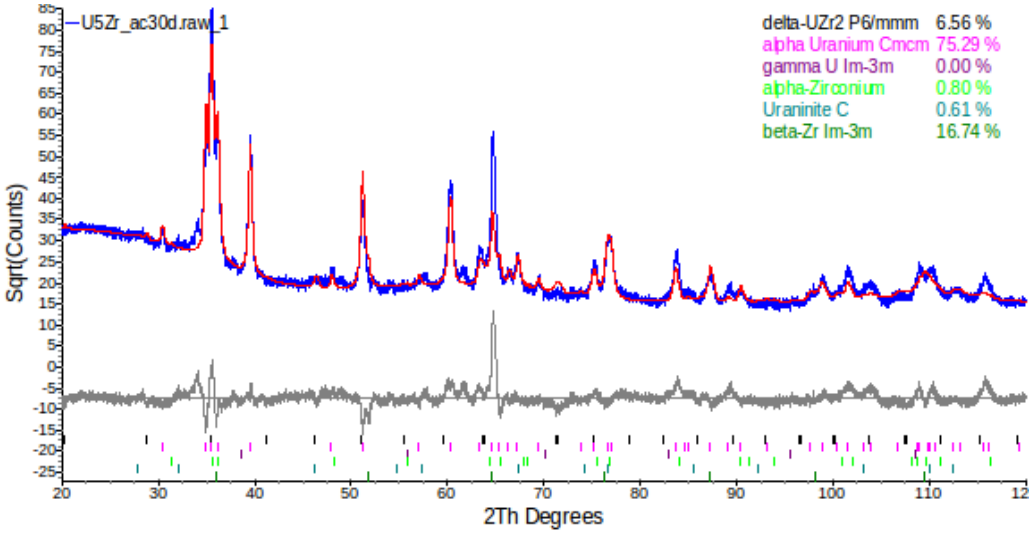

Fig. 5.3.: XRD pattern of as-cast U-5Zr alloy annealed for 30 days

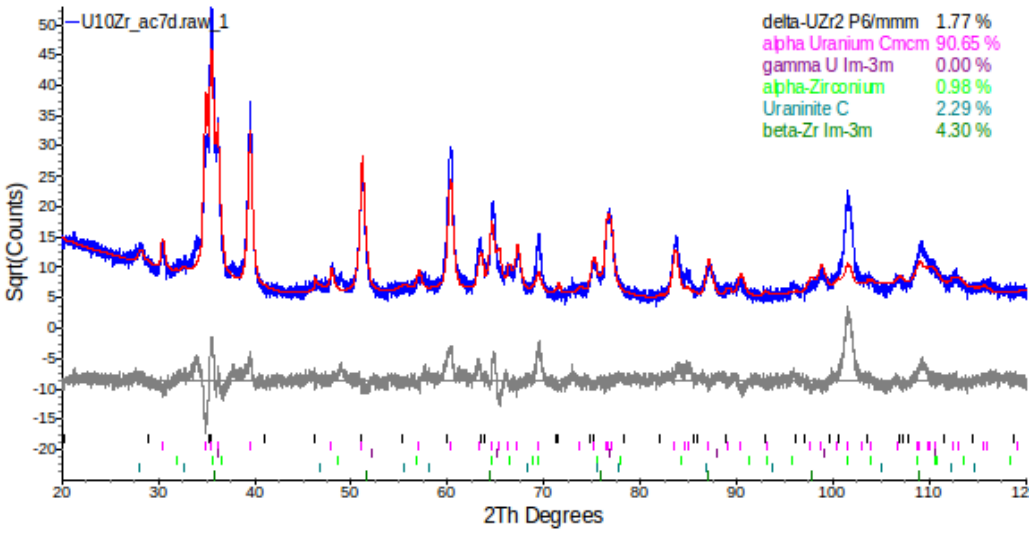

Fig. 5.4.: XRD pattern of as-cast U-10Zr alloy annealed for 7 days

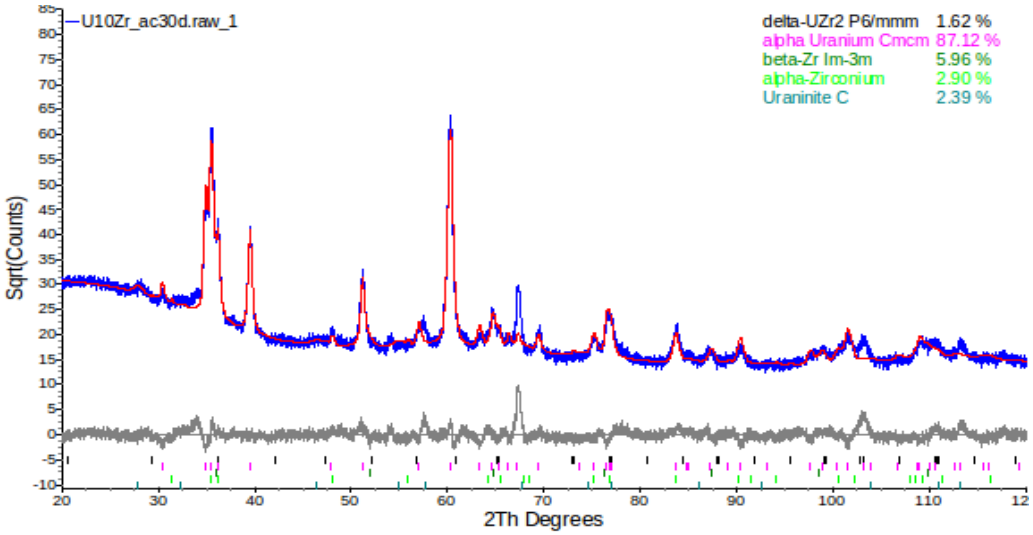

Fig. 5.5.: XRD pattern of as-cast U-10Zr alloy annealed for 30 days

It was previously mentioned that δ phase peaks were observed for a step-cooled and annealed (Step-cooled from γ phase and held in $(\alpha + \delta)$ phase field for 3 days. This thermal profile is referred to as TP-I). U-10Zr alloy sample and no peaks were

found in the samples annealed for 7 and 30 days (Figures 4.39, 4.42, and 4.43, respectively). In this case, the temperature was increased from room temperature to 600^{o}C. This thermal profile is referred to as TP-II. There is a cursory evidence of this phase only forming when cooled from γ phase. To verify this, U-10Zr alloy buttons were annealed in the glovebox at UNLV where the oxygen and water levels in the glove box never exceeded 4 ppm during the annealing process. The alloy buttons were subjected to two thermal profiles, (i.e, TP-I and TP-II) and in the case of TP-II, the annealing period was for 3 days. As expected, there were no peaks for δ phase in the button subjected to TP-II while there were peaks in button subjected to TP-I.

Kaity et al [135] observed that U-6wt%Zr exhibited a feature which is of interest in the present discussion. They found that DSC curves for as-cast and quenched U-6Zr had a transformation at 570^{o}C. Their as-cast sample was made via injection casting which has much faster solidification rate than for the as-cast sample in the present investigation. The samples were annealed at 550^{o}C and it was found that the peak area reduced as a function of annealing time. The peak totally vanished upon annealing for 24 hours and they attributed this transformation to $\alpha_a^{'} \rightarrow \alpha$.

The presence of the metastable ω phase in their alloy is immediately apparent in the light of this present study and the preponderance of data from the multiple compositions and thermal profiles. If this indeed is the case, then the vanishing of the DSC peak correlates excellently with it transforming to γ as the $\delta \rightarrow \gamma$ transformation at $\sim$617^{o}C was not seen after annealing by Kaity et al [135]. Moreover, vanishing of the δ/ω phase peaks noted above in U-20Zr agrees very well with this explanation. It is pointed out here that the idea of mentioning the data of Kaity et al [135] is not to prove their interpretation of their data wrong but, on the contrary, is used to make the case for the presence of ω phase stronger. Based on the comments presented above, it is hence suggested that it might be more appropriate to consider

the hexagonal δ phase as the metastable ω (athermal-ω in γ-quenched alloys and diffusional-ω in as-cast alloys) phase which transforms to γ phase on annealing.

6. SUMMARY AND CONCLUSIONS

Based on the results from the present study the findings can be summarized as follows:

1. When quenched from γ phase, athermal-ω, martensitic $\alpha^{'}$, along with some remnant γ are observed in U-2Zr, U-5Zr, U-10Zr, U-20Zr, and U-30Zr alloys. Based on information gleaned from XRD, TEM, and transformation temperatures from DSC heating curves, γ transforms to the above phases by two paths. In the first scheme, γ partially shears to $\alpha^{'}$, and the remnant γ then transforms to ω. In the second scheme, γ transforms to ω which then partially shears to $\alpha^{'}$. In the case of U-50Zr, γ transforms to ω via athermal-ω transformation.

2. Alloys annealed in $(\alpha + \gamma)$ and quenched in water retained γ phase. The microstructure consisted of α-U matrix with γ precipitates for alloys upto 20wt%Zr while the matrix was γ and the precipitates were α for U-30Zr.

3. Absence of δ phase peaks in U-rich as-cast alloys can be explained if diffuional-ω is present instead of δ.

4. Step-cooled U-5Zr and U-10Zr alloys from $(\alpha + \gamma)$ to $(\alpha + \delta)$ phase showed broad peaks for δ phase indicating incomplete collapse of $\{111\}_{\gamma}$ planes.

5. BSE images of as-cast alloys of U-2, 5, 10, 20, and 30Zr when annealed for 1, 3, 7, and 30 days clearly revealed a two phase microstructure. WDS analyses for chemical composition in individual phases revealed that the matrix consisted of α-U while the precipitates were δ phase. However, XRD data still did not show any δ phase peaks in U-2, 5, and 10 Zr and the peaks which were seen in as cast U-20Zr vanished after 7 days of annealing.

6. Interpretation of the data from step-cooled samples and annealed samples in the present study is consistent if diffusional-ω in as-cast alloys is present.

To restate the most important and potentially debatable observation from the work reported here, strong evidence was reported for the existence of the metastable diffusional-ω phase in as-cast alloys and athermal-ω in quenched alloys. Regardless of the formation mechanism of ω (i.e, diffusional and shear) it is suggested that the long-held conventional understanding in literature regarding the stable nature of the UZr_2 δ phase is incorrect and must must be reconsidered as the data from present study agree well if a metastable ω is present.

The transformation of simple b.c.c solid solutions containing Zr to a hexagonal structure (i.e, ω) is rarely stable [108]. So, experiments which conclusively show the presence of ω instead of δ are suggested. By carrying out careful annealing experiments at various temperatures for various lengths of time, and by using state-of-the-art characterization tools such as TEM, quenching dilatometry, and neutron diffraction, the ambiguity can be completely resolved.

REFERENCES

[1] G. L Hofman and L. C Walters. Metallic Fast Reactor Fuels. In B. R. T. Frost, editor, *Materials Science and Technology, Vol. 10A, Nuclear Materials*. VCH Publishers, 1994.

[2] A. N Holden. *Physical Metallurgy of Uranium*. Addison-Wesley Pub. Co., 1958.

[3] Bernhard Blumenthal. The Transformation Temperatures of High-Purity Uranium. *Journal of Nuclear Materials*, 2(1):23–30, 1960.

[4] B. A Loomis and S. B Gerber. Length and Electrical Resistivity Changes of Neutron Irradiated Uranium. *Philosophical Magazine*, 18(153):539–553, 1968.

[5] B. A. Loomis, T. H. Blewitt, A. C. Klank, and S. B. Gerber. Elongation of Uranium Single Crystals during Neutron Irradiation. *Applied Physical Letters*, 5:135–137, 1964.

[6] Walters L. C., Seidel B. R., and Kittel J. H. Performance of Metallic Fuels and Blankets in Liquid-Metal Fast Breeder Reactors. *Nuclear Technology*, 65:179–231, 1984.

[7] G. L. Hofman, L. C. Walters, and T. H. Bauer. Metallic Fast Reactor Fuels. *Progress in Nuclear Energy*, 31:83–110, 1997.

[8] M. C. Billone and Y. Y. Liu. Status of Fuel Element Modeling Codes for Metallic Fuels. In *Proceedings of the International Conference Reliable Fuels for Liquid Metal Reactors*, Tuscon, Arizona, 1986. American Nuclear Society.

[9] Kobayashi. T, Kinoshita. M, Hattori. S, Ogawa. T, Tsuboi. Y, Ishida. M, Ogawa. S, and Saito. H. Development of the Sesame Metallic Fuel Performance Code. *Nuclear Technology*, 89:183–193, 1990.

[10] Ogata. T and Yokoo. T. Development and Validation of ALFUS: An Irradiation Behavior Analysis Code for Metallic Fast Reactor Fuels. *Nuclear Technology*, 128:113–123, 1999.

[11] Hwang. W, Nam. C, Byun. T. S., and Kim. Y. C. MACSIS: A Metallic Fuel Performance Analysis Code for Simulating In-Reactor Behavior Under Steady-State Conditions. *Nuclear Technology*, 123:130–141, 1998.

[12] Chan Bock Lee, Dae Ho Kim, and Youn Ho Jung. Fission Gas Release and Swelling Model of Metallic Fast Reactor Fuel. *Journal of Nuclear Materials*, 288:29–42, 2001.

[13] Aydn Karahan and Jacopo Buongiorno. A New Code for Predicting the Thermo-Mechanical and Irradiation Behavior of Metallic Fuels in Sodium Fast Reactors. *Journal of Nuclear Materials*, 396:283–293, 2010.

[14] Gerard L. Hofman, Pahl R. G., Lahm C. E., and Porter D. L. Swelling Behavior of U-Pu-Zr Fuel. *Metallurgical Transactions A*, 21:517–528, 1990.

[15] J. Rest. An Analytical Study of Gas-Bubble Nucleation Mechanisms in Uranium-Alloy Nuclear Fuel at High Temperature. *Journal of Nuclear Materials*, 402:179–185, 2010.

[16] J. Rest. Kinetics of Fission-Gas-Bubble-Nucleated Void Swelling of the Alpha-Uranium Phase of Irradiated U-Zr and U-Pu-Zr Fuel. *Journal of Nuclear Materials*, 207:192–204, 1993.

[17] G. L. Hofman, S. L. Hayes, and M. C. Petri. Temperature Gradient Driven Constituent Redistribution in U-Zr Alloys. *Journal of Nuclear Materials*, 227:277–286, 1996.

[18] Catherine Sabathier, Laetitia Vincent, Philippe Garcia, Frederico Garrido, Galle Carlot, Lionel Thome, P. Martin, and Carole Valot. In situ TEM Study of Temperature-Induced Fission Product Precipitation in UO_2. *Nuclear Instruments and Methods in Physics Research Section B: Beam Interactions with Materials and Atoms*, 266:3027–3032, 2008.

[19] J.H. Evans. Effect of Temperature on Bubble Precipitation in Uranium Dioxide Implanted with Krypton and Xenon Ions. *Journal of Nuclear Materials*, 188:222–225, 1992.

[20] A. Michel, C. Sabathier, G. Carlot, O. Katasov, S. Bouffard, P. Garcia, and C. Valot. An *in situ* TEM Study of the Evolution of Xe Bubble Populations in UO_2. *Nuclear Instruments and Methods in Physics Research Section B: Beam Interactions with Materials and Atoms*, 272:218–221, 2012.

[21] Hj. Matzke. Inert Gas Diffusion and Radiation Damage in Ionic Crystals and Sinters Following Ion Bombardment. *Canadian Journal of Physics*, 46:621–634, 1968.

[22] Hj. Matzke, P. G. Lucuta, and T. Wiss. Swift Heavy Ion and Fission Damage Effects in UO_2. *Nuclear Instruments and Methods in Physics Research Section B: Beam Interactions with Materials and Atoms*, 166-167:920–926, 2000.

[23] Hj. Matzke, , C. Ronchi, and C. Baker. Precipitation of Xe and Cs into Bubbles, Kinetics of Bubble Migration and Alternative Release Processes. *Eur. Appl. Res. Rept. Nucl. Sci. Technol.*, 5:1105–1158, 1984.

[24] Hj. Matzke and L.M. Wang. High-Resolution Transmission Electron Microscopy of Ion Irradiated Uranium Oxide. *Journal of Nuclear Materials*, 231:155–158, 1996.

[25] J. Gan, D.D. Keiser, B.D. Miller, M.A. Kirk, J. Rest, T.R. Allen, and D.M. Wachs. Kr Ion Irradiation Study of the Depleted-Uranium Alloys. *Journal of Nuclear Materials*, 407:48–54, 2010.

[26] J. Gan, D.D. Keiser Jr., B.D. Miller, D.M. Wachs, T.R. Allen, M. Kirk, and J. Rest. Microstructure of RERTR DU-Alloys Irradiated with Krypton Ions up to 100 dpa. *Journal of Nuclear Materials*, 411:174–180, 2011.

[27] R.C. Birtcher and P. Baldo. Use of Ion Beams to Simulate Reaction of Reactor Fuels with their Cladding. *Nuclear Instruments and Methods in Physics Research Section B: Beam Interactions with Materials and Atoms*, 242:487–489, 2006.

[28] C. W. Jacob and B. E. Warren. The Crystalline Structure of Uranium. *Journal of American Chemical Society*, 59:2588–2591, 1937.

[29] J. Thewlis and H. Steeple. The β-Uranium Structure. *Acta Crystallographica*, 7:323–328, 1954.

[30] J. Thewlis. Structure of Uranium. *Nature*, 168:198–199, 1951.

[31] J. Thewlis. An X-Ray Powder Study of β-Uranium. *Acta Crystallographica*, 5:790–794, 1952.

[32] C. W. Tucker Jr. The Crystal Structure of β Phase Uranium. *Acta Crystallographica*, 4:425–431, 1951.

[33] C. W. Tucker Jr. A Supplementary Note on the Crystal Structure of β-Uranium. *Acta Crystallographica*, 5:395–399, 1952.

[34] C. W. Tucker Jr. and P. Senio. An Improved Determination of the Crystal Structure of β-Uranium. *Acta Crystallographica*, 6:753–760, 1953.

[35] C. W. Tucker Jr. The Status of β-Uranium Structure. *Acta Crystallographica*, 7:752–756, 1954.

[36] C. W. Tucker Jr., P. Senio, J. Thewlis, and H. Steeple. Joint Note on the β-Uranium Structure. *Acta Crystallographica*, 9:472–474, 1956.

[37] H. Steeple and T. Ashworth. The Minimum Residual Refinement of β-Uranium from Polycrystalline Data. *Acta Crystallographica*, 21:995–998, 1966.

[38] J. Donohue and H. Einsphar. The Structure of β-Uranium. *Acta Crystallographica*, B27:1740–1743, 1971.

[39] J. C. McLennan and R. W. McKay. *Trans. Roy. Soc. Can.*, 24, 1930.

[40] A. S. Wilson and R. E. Rundle. The Structure of Uranium Metal. *Acta Crystallographica*, 2:126–127, 1949.

[41] A. Goldberg and T. B. Massalski. Phase Transformations in the Actinides. In *Nuclear Metallurgy*, volume 17 of *Proceedings of the Fourth International Conference on Plutonium and Other Actinides*, pages 875–973, Santa Fe, 1970.

[42] Harry L. Yakel. A Review of X-ray Diffraction Studies on Uranium Alloys. In John J. Burke, David A. Colling, Alvin E. Gorum, and Jacob Greenspan, editors, *Physical Metallurgy of Uranium Alloys*, Proceedings of the Third Army Materials Technology Conference, pages 259–308, Colorado, 1974.

[43] D. Blake and R. F. Hehemann. Transformations in Uranium Base Alloys. In John J. Burke, David A. Colling, Alvin E. Gorum, and Jacob Greenspan, editors, *Physical Metallurgy of Uranium Alloys*, Proceedings of the Third Army Materials Technology Conference, pages 189–218, Colorado, 1974.

[44] Mme J. Lehmann and R. F. Hills. Proposed Nomenclature for Phases in Uranium Alloys. *Journal of Nuclear Materials*, 2:261–268, 1960.

[45] R. D. Field, D. J. Thoma, P. S. Dunn, D. W. Brown, and C. M. Cady. Martensitic Structures and Deformation Twinning in the U-Nb Shape-Memory Alloys. *Philosophical Magazine*, 81:1691–1724, 2001.

[46] Harry L. Yakel. Crystal Structures of Transition Phases Formed in U-16.60at%Nb-5.64at%Zr Alloys. *Journal of Nuclear Materials*, 33:286–295, 1969.

[47] P. Duwez. The Effect of Cooling Rate on the Allotropic Transformation Temperatures in Pure Uranium. *Journal of Applied Physics*, 24:152–156, 1953.

[48] B. A. Hatt. The Orientation Relationship Between the Gamma and Alpha Structures in Uranium-Zirconium Alloys. *Journal of Nuclear Materials*, 19:133–141, 1966.

[49] W. G. Burgers. On the Process of Transition of the Cubic-Body-Centered Modification into the Hexagonal-Close-Packed Modification of Zirconium. *Physica*, 1:561–586, 1934.

[50] K. Tangri and G. I. Williams. Metastable Phases in the Uranium-Molybdenum System and Their origin. *Journal of Nuclear Materials*, 4:226–233, 1961.

[51] K. Tangri. *Journées Métallurgiques d'Automne*, 90, 1960.

[52] K. Tangri and D. K. Chaudhuri. Metastable Phases in the Uranium Alloys with High Solute Solubility in the BCC Gamma Phase. Part I- The System U-Nb. *Journal of Nuclear Materials*, 15:278–287, 1965.

[53] R. A. Vandermeer. Phase Transformations in a Uranium + 14at% Niobium Alloy. *Acta Metallurgica*, 28:383–393, 1980.

[54] Vandermeer, R. A. and Ogle, J. C. and Northcutt, W. G. A Phenomenological Study of the Shape Memory Effect in Polycrystalline Uranium-Niobium Alloys. *Metallurgical Transactions A*, 12(5):733–741, 1981.

[55] M. Anagnostidis, M. Colombié, and H. Monti. Phases Metastables dans les Alliages Uranium-Niobium. *Journal of Nuclear Materials*, 11:67–76, 1964.

[56] C. D'Amato, F. S. Saraceno, and T. B. Wilson. Phase Transformations and Equilibrium Structures in Uranium-Rich Niobium alloys. *Journal of Nuclear Materials*, 12(3):291–304, 1964.

[57] G. I. Terekhov, R. Kh. Tagirova, and O. S. Ivanov. Transformation of γ-Solid Solutions in U-Nb and U-Zr Alloys. *Physical Chemistry of Alloys and Refractory Compounds of Thorium and Uranium*, pages 39–44, 1972.

[58] D. A. Carpenter and R. A. Vandermeer. An X–Ray Diffraction Study of a Martensitic Transformation in Uranium Alloys. *Journal de Physique*, 43(12):C4–395, 1982.

[59] R. D. Field, , D. W. Brown, and D. J. Thoma. Texture Development and Deformation Mechanisms During Uniaxial Straining of U-Nb Shape-Memory Alloys. *Philosophical Magazine*, 85:2593–2609, 2005.

[60] D. Stewart and G. I. Williams. The Structure and Occurrence of the Metastable Monoclinic Phase, $\alpha_b^{'}$, in Uranium-Molybdenum Alloys. *Journal of Nuclear Materials*, 20:262–268, 1966.

[61] B. W. Howlett. A Study of the Shear Transformations from the Gamma-Phase in Uranium-Molybdenum Alloys Containing 6.0-12.5at% Molybdenum. *Journal of Nuclear Materials*, 35:278–292, 1970.

[62] R. F. Hills, B. R. Butcher, and J. A. Heywood. A Study of the Effect of Cooling Rate on the Decomposition of the γ Phase in Uranium-Low Molybdenum Alloys. *Journal of the less-common metals*, 3:155–169, 1961.

[63] R. F. Hills, B. W. Howlett, and B. R. Butcher. Further Studies on the Decomposition of the γ Phase in Uranium-Low Molybdenum alloys. *Journal of the less-common metals*, 5:369–373, 1963.

[64] Mme J. Lehmann. Phases Monocliniques dans les Alliages Uranium-Molybdene. *Journal of Nuclear Materials*, 4(2):218–225, 1961.

[65] J. G. Speer and D. V. Edmonds. An Investigation of the $\gamma \rightarrow \alpha$ Transformation in Uranium Alloys. *Acta Metallurgica*, 36:1015–1033, 1988.

[66] M Anagnostidis, R. Baschwitz, and M. Colombie. Phases Métastables dans les Alliages Uranium-Titane. *Memoires et Etudes Scientifiques de la Revue de Metallurgie*, LXIII:163 – 168, 1966.

[67] K. Tangri, D. K. Chaudhuri, and C. N. Rao. Metastable Phases in Uranium Alloys with High Solute Solubility in the BCC Gamma Phase. Part II- The System U-Ru. *Journal of Nuclear Materials*, 15:288–297, 1965.

[68] R. F. Hills, B. W. Howlett, and B R. Butcher. The Effect of Cooling Rate and Composition on the Transformation of the Gamma Phase in Uranium-Ruthenium Alloys (With an Appendix on Ruthenium as a Grain Refining Element. *Journal of Nuclear Materials*, 16:109–128, 1965.

[69] R. J. Jackson and W. L. Larsen. Transformation and Structures in the Uranium-Rhenium System I. Metastable $\alpha^{'}$, $\alpha^{''}$, and γ^{o} Structures. *Journal of Nuclear Materials*, 21:263–276, 1967.

[70] C. M. Wayman. *Introduction to the Crystallography of Martensitic Transformations*. The Macmillan Company, 1964.

[71] J. S. Bowles and J. K. Mackenzie. Crystallography of Martensitic Transformations I. *Acta Metallurgica*, 2:129–137, 1954.

[72] J. W. Christian. Analyses of Lattice and Shape Deformations and of Atomic Shuffles in Martensitic Transformation. *Materials Science and Engineering*, A127:215–227, 1990.

[73] J. W. Christian. *The Theory of Transformations in Metals and Alloys*. Pergamon, 2002.

[74] Ming-Xing Zhang and Patrick M. Kelly. Crystallographic Features of Phase Transformations in Solids. *Progress in Materials Science*, 54:1101–1170, 2009.

[75] M. A. Jaswon and J. A. Wheeler. Atomic Displacements in the Austenite-Martensite Transformation. *Acta Crystallographica*, 1:216–224, 1948.

[76] C. M. Wayman. Crystallographic Theories of Martensitic Transformations. *Journal of Less-Common Metals*, 28:97–105, 1972.

[77] J. W. Christian. The $\gamma \rightarrow \alpha$ Transformation in Uranium Alloys. M/R 1811, A.E.R.E.

[78] G. H. May. IRD 66-71, International Research and Development Co. Research Report.

[79] J. G. Speer and D. V. Edmonds. Martensite Lattice Correspondence and Twinning in Uranium Alloys. volume 21, pages 705–709. Materials Research Society Symposium Proceedings, 1984.

[80] F. Giraud-Héraud, J. Guillaumin, and R. Sifferlen. Mechanismes de Transformation des Alliages U-Mo 1.5% par Refroidissement Rapide a Partit de la Phase γ. *Journal of Nuclear Materials*, 25:16–23, 1968.

[81] A. G. Crocker and N. D. H. Ross. The Crystallography of Martensitic Transformations in Uranium and It's Alloys. In *The Mechanism of Phase Transformations in Crystalline Solids*, volume 33, pages 176–180, University of Manchester, 1969. Institute of Metals.

[82] N. D. H. Ross and A. G. Crocker. Type II Twinning in Martensite Crystallographic Theories. *Scripta Metallurgica*, 3:37–42, 1969.

[83] A. G. Crocker. Crystallographic of Deformation Twinning in Alpha-Uranium. *Journal of Nuclear Materials*, 16:306–326, 1965.

[84] A. G. Crocker and B. A. Bilby. On the Theory of Martensitic Crystallography. *Acta Metallurgica*, 9:992–995, 1961.

[85] B. A. Bilby and A. G. Crocker. The Theory of the Crystallography of Deformation Twinning. *Proceedings of the Royal Society A*, 288:240–255, 1965.

[86] B. R. Butcher and A. H. Rowe. The Crystallography of the $\beta \rightarrow \alpha$ Phase Transformation in Uranium-1.4 Atomic per cent. Chromium Alloy. In *The Mechanism of Phase Transformations in Metals*, volume 18, pages 229–242, Royal Institution, London, 1956. Institute of Metals.

[87] W. M. Lomer. The $\beta \rightarrow \alpha$ Transformation in Uranium-1.4 Atomic per cent. Chromium Alloy. In *The Mechanism of Phase Transformations in Metals*, volume 18, pages 243–252, Royal Institution, London, 1956. Institute of Metals.

[88] D. Dayan and M. Talianker. Application of the Double-Shear Theory of Martensite Crystallography to the $\beta \rightarrow \alpha^{'}$ Transformation in an U(Ga) Alloy. *Metallurgical Transactions A*, 21A:2131–2136, 1990.

[89] D. Dayan and M. Talianker. The Kinetics of the Isothermal Martensitic $\beta \rightarrow \alpha$ Transformation in U(Ga) Alloys. *Metallurgical Transactions A*, 20A:1163–1168, 1989.

[90] D. G. Pettifor. Theory of Crystal Structures of Transition Metals. *Journal of Physics C: Solid State Physics*, 3:367–377, 1970.

[91] John A. Moriarty. Ultrahigh-Pressure Structural Phase Transitions in Cr, Mo, and W. *Physical Review B*, 45:2004–2014, 1992.

[92] Hui Xia, Arthur L. Ruoff, and Yogesh K. Vohra. Temperature Dependence of the ω-bcc Phase Transition in Zirconium Metal. *Physical Review B*, 44:10374–10376, 1991.

[93] Y. K Vohra. Electronic Basis for Omega Phase Stability in Group {IV} Transition Metals and Alloys. *Acta Metallurgica*, 27(10):1671–1675, 1979.

[94] S. K. Sikka, Y. K. Vohra, and R. Chidambaram. Omega Phase in Materials. *Progress in Materials Science*, 27:245–310, 1982.

[95] Yu. A. Bagaryatskiy and G. I. Nosova. The $\beta \rightarrow \omega$ Transformation in Titanium Alloys During Quenching: A Singular Kind of Martensitic Transformation. *Physics of Metals and Metallography*, 13:92–101, 1962.

[96] Banerjee. S, Tewari. R, and Dey. G. K. Omega Phase Transformation-Morphologies and Mechanisms. *International Journal of Materials Research/Zeitschrift fur Metallkunde*, 2006:963–977, 2006.

[97] C.B. Basak, S. Neogy, D. Srivastava, G.K. Dey, and S. Banerjee. Disordered bcc γ-Phase to δ-Phase Transformation in Zr-Rich U-Zr Alloy. *Philosophical Magazine*, 91:3290–3306, 2011.

[98] (Miss) J. M. Silcock, M. H. Davies, and H. K. Hardy. The Structure of the ω Precipitate in Titanium-16% Vanadium Alloy. In *The Mechanism of Phase Transformations in Metals*, volume 18, pages 93–104, Royal Institution, London, 1956. Institute of Metals.

[99] Yu. A. Bagaryatskyi, G. I. Rosava, and T. W. Saganova. *Doklady Akademii Nauk SSSR*, 105:1225, 1955.

[100] P. D. Frost, W. M. Parris, L. L. Hirsch, J. R. Doig, and C. M. Schwartz. Isothermal Transformation of Titanium-Chromium Alloys. *Transactions of ASM*, 46:231–256, 1954.

[101] J. M. Silcock. An X-Ray Examintion of the ω-Phase in TiV, TiMo and TiCr Alloys. *Acta Metallurgica*, 6:481–493, 1958.

[102] D. De Fontaine and Otto Buck. A Monte Carlo Simulation of the Omega Phase Transformation. *Philosophical Magazine*, 27:967–983, 1973.

[103] D. De Fontaine. Mechanical Instabilities in the B.C.C Lattice and the Beta to Omega Phase Transformation. *Acta Metallurgica*, 18:275–279, 1970.

[104] B. A. Hatt and J. A. Roberts. The ω-Phase in Zirconium Base Alloys. *Acta Metallurgica*, 8:575–584, 1960.

[105] B. A. Hatt and J. A. Roberts. R. 114/9, Fulmer Research Institute Progress Report.

[106] Chandra Bhanu Basak, N. Prabhu, and Madangopal Krishnan. On the Formation Mechanism of UZr_2 Phase. *Intermetallics*, 18:1707–1712, 2010.

[107] E. R. Boyko. The Structure of δ Phase in the Uranium-Zirconium System. *Acta Crystallographica*, 10:712–713, 1957.

[108] J. M. Silcock. Intermediate Phase in the Uranium-Zirconium System. *Journal of Metals*, 9:521, 1957.

[109] Mitsuo Akabori, Toru Ogawa, Akinori Itoh, and Yukio Morii. The Lattice Stability and Structure of δ-UZr_2 at Elevated Temperatures. *J. Phys: Condens. Matter*, 7:8249–8257, 1995.

[110] M. Akabori, A. Itoh, T. Ogawa, F. Kobayashi, and Y. Suzuki. Stability and Structure of the δ Phase of the U-Zr Alloys. *Journal of Nuclear Materials*, 188:249–254, 1992.

[111] Alex Landa, Per Soderlind, Patrice E. A. Turchi, L. Vitos, and A. Ruban. Density-Functional Study of Zr-Based Actinide Alloys. *Journal of Nuclear Materials*, 385:68–71, 2009.

[112] Alex Landa, Per Soderlind, and Patrice E. A. Turchi. Density-Functional Study of the U-Zr System. *Journal of Alloys and Compounds*, 478(12):103–110, 2009.

[113] D. Summers-Smith. The Constitution of Uranium-Zirconium Alloys. *Journal of Institute of Metals*, 83:277–282, 1955.

[114] H. A. Saller and F. A. Rough. Compilation of U.S and U.K Uranium and Thorium Constitutional Diagrams. BMI-1000, Battelle Memorial Institute.

[115] Frank A. Rough, Alfred E. Austin, Arthur A. Bauer, and J. Robert Doig. The Stability and Existence Range of the Zirconium-Uranium Epsilon Phase. BMI-1092, Battelle Memorial Institute.

[116] J. F. Duffey and C. A. Bruch. Delta Phase Field of the U-Zr Equilibrium Diagram. *Transactions of The Metallurgical Society of AIME*, 212:17–19, 1958.

[117] A. N. Holden and W. E. Seymour. Intermediate Phase in the Uranium-Zirconium System. *Journal of Metals*, 206:1312–1316, 1956.

[118] S. T. Zegler. The Uranium-Rich End of the Uranium-Zirconium System. ANL-6055, Argonne National Laboratory.

[119] R. I. Sheldon and D. E. Peterson. The U-Zr (Uranium-Zirconium) System. *Bulletin of Alloy Phase Diagrams*, 10:165–171, 1989.

[120] Frank. A. Rough. An Evaluation of Data on Zirconium-Uranium Alloys. BMI-1030, Battelle Memorial Institute.

[121] Grant William Helmreich. Characterization of Alpha-phase Sintering of Uranium and Uranium-Zirconium Alloys for Advanced Nuclear Fuel Applications. Master's thesis, Texas A&M University, 2010.

[122] A.M. Kelly, R.D. Field, and D.J. Thoma. Metallographic Preparation Techniques for U-6wt%Nb. *Journal of Nuclear Materials*, 429:118–127, 2012.

[123] Heatbath® Corporation/Park Metallurgical. `http://heatbath.com/heat-treating-products-2/neutral-salts/`.

[124] A. J. Perkins, P. E. Yaffe, and R. F. Hehemann. The Isothermal Omega Transformation in Zirconium-Niobium Alloys. *Metallography*, 4:303–323, 1971.

[125] R. Tewari, D. Srivastava, G. K. Dey, J. K. Chakravarty, and S. Banerjee. Microstructural Evolution in Zirconium Based Alloys. *Journal of Nuclear Materials*, 383(12):153–171, 2008.

[126] G. K. Dey, R. Tewari, S. Banerjee, G. Jyoti, S. C. Gupta, K. D. Joshi, and S. K. Sikka. Formation of a Shock Deformation Induced ω Phase in Zr 20 Nb Alloy. *Acta Materialia*, 52(18):5243–5254, 2004.

[127] B. S. Hickman. The Formation of Omega Phase in Titanium and Zirconium Alloys: A Review. *Journal of Materials Science*, 4:554–563, 1969.

[128] G. Lagerberg. Phase Transformations in a Uranium-Zirconium Alloy Containing 2 weight per cent Zirconium. *Journal of Nuclear Materials*, 9:261–276, 1963.

[129] R. F. Hills, R. Butcher, B. W. Howlett, and D. Stewart. The Effect of Cooling Rate on the Decomposition of the γ Phase in Uranium-Zirconium Alloys. *Journal of Nuclear Materials*, 16:25–38, 1965.

[130] A. Virot. Characteristiques de l'alliage Uranium-Zirconium a 6% en poids de Zirconium. *Journal of Nuclear Materials*, 5:109–119, 1962.

[131] Chandra Bhanu Basak. Microstructural Evolution of U-Rich U-Zr Alloys Under Near-Equilibrium Condition. *Journal of Nuclear Materials*, 416:280–287, 2011.

[132] Chandra Bhanu Basak, R. Keswani, G. J. Prasad, H. S. Kamath, and N. Prabhu. Phase Transformations in U-2wt%Zr Alloy. *Journal of Alloys and Compounds*, 471:544–552, 2009.

[133] Chandrabhanu Basak, G. J. Prasad, H. S. Kamath, and N. Prabhu. An Evaluation of the Properties of As-cast U-Rich U-Zr Alloys. *Journal of Alloys and Compounds*, 480:857–862, 2009.

[134] Chandrabhanu Basak, R. Keswani, G. J. Prasad, H. S. Kamath, N. Prabhu, and S. Banerjee. Investigation on the Martensitic Transformation and the Associated Intermediate Phase in U-2wt%Zr Alloy. *Journal of Nuclear Materials*, 393:146–152, 2009.

[135] Santu Kaity, Joydipta Banerjee, M. R. Nair, K. Ravi, Smruti Dash, T. R. G. Kutty, Arun Kumar, and R. P. Singh. Microstructural and Thermophysical Properties of U-6wt%Zr Alloy for Fast Reactor Applications. *Journal of Nuclear Materials*, 427:1–11, 2012.

[136] M. C. Petri, L. Leibowitz, M. H. Mueller, J. W. Richardson, and D. D. Keiser. Jr. Phase Identification in a U-Zr/Ni-Cr Diffusion Couple Using Synchrotron Radiation. *Journal of Materials Research*, 11:332–340, 1996.

[137] J. T. McKeown, S. Irukuvarghula, S. Ahn, M. A. Wall, L. L. Hsiung, S. McDeavitt, and P. E. A. Turchi. Coexistence of the α and δ Phases in an As-cast Uranium-Rich UZr Alloy. *Journal of Nuclear Materials*, 436:100–104, 2013.

[138] J. T. McKeown, S. Irukuvarghula, S. Ahn, M. A. Wall, L. L. Hsiung, S. McDeavitt, and P. E. A. Turchi. Microstructural Assessment of As-cast Uranium-Rich U-Zr Alloys. In preparation.

[139] A. G. Knapton. The Crystal Structure of TiU_2. *Acta Crystallographica*, 7:457–458, 1954.

[140] R. D. Field and D. J. Thoma. Crystallographic and Kinetic Origins of Acicular and Banded Microstructures in UNb Alloys. *Journal of Nuclear Materials*, 436(13):105–117, 2013.